Photoconductivity and gas sensing properties of ZnO nanowire devices

Dissertation
zur Erlangung des akademischen Grades
doctor rerum naturalium (Dr. rer. nat)

vorgelegt dem Rat der Physikalisch-Astronomischen Fakultät
der Friedrich-Schiller-Universität Jena

von Dottore Magistrale in Fisica Davide Cammi
geboren am 24.04.1985 in Fiorenzuola d'Arda (PC), Italien

Gutachter:

1. Prof. Dr. Carsten Ronning, FSU Jena

2. Prof. Dr. Tobias Voss, TU Braunschweig

3. Prof. Dr. Giancarlo Cicero, Politecnico di Torino (Turin, Italien)

Tag der Disputation: 23.02.2016

Contents

Chapter 1

Introduction

1.1 Motivation

The field of nanotechnology has received in the last two decades an increasingly importance in all research areas of natural sciences [1–4]. The term refers to a large variety of techniques and applications concerning objects, which typically have at least one dimension not larger than few hundreds of nanometers. Well known examples of such nanostructures are quantum wells, quantum dots, nanowires and nanotubes [5].

From the perspective of the basic research, the possibility of dealing with objects of reduced dimensionality offers the opportunity to investigate physical processes at the nanoscale level. Under these conditions several physical properties start to deviate from those, which are typically observed in bulk materials. For instance, Band gap, density of states as well as electric, optical and mechanical properties can be strongly modulated by the size of the nanostructures, due to the quantum confinement of charge carriers [6–11]. Compared to bulk structures, nanostructures are also characterized by a significantly larger surface to volume ratio, which leads to a dramatic impact of the surface on fundamental physical processes such as charge transport and interaction between matter and light [12].

Furthermore, the deep comprehension of the nature laws at the nanoscale level opens up tremendous possibilities in terms of applications. The potentialities of nanostructures, which are mainly based on their high surface to volume ratio, are nowadays intensively exploited in electronics, photonics and bio-sciences [13]. These include in particular their extreme sensitivity to surface related processes, such as molecular detection and catalytic activity [14, 15], enhanced interaction with electromagnetic radiation [12] and the possibility to control their electrical, magnetic and properties through the quantum confinement of charge carriers [16]. Furthermore, the process of device miniaturization allows cosiderable reduction of the power consumption, enhanced operation speed, as well as improved data processing and transmission [17]. Among nanostructures, semiconductor nanowires (NWs) are the most promising building components for nano-electronics and nano-photonics devices [18, 19]. They typically show an approximatively cylindrical geometry, with diameter around 100 nm and length up to tens of micrometers [5, 20]. Due to these unique geometrical properties, they can be easily integrated into electronics devices as active semiconducting channel [21, 22] or can act as photonics waveguides and resonant cavities for nanowire based lasers [19, 23, 24]. Moreover, nanowire morphology offers optimal features for energy harvesting [25, 26], gas and bio-sensing applications [27, 28], allowing high conversion efficiency and low detection limit.

Semiconductor nanowires are available in a large variety of material compositions, such as silicon, III-V and II-VI compounds. Among them, metal oxide nanowires represent a large class of versatile nanostructures, which have been widely investigated as active component in opto-electronic devices, field-effect transistors and gas sensors [29, 30]. In particular, ZnO has attracted increasingly interest due to the combinations of unique properties. These include for instance the large exciton energy of 60 meV, which ensures intense excitonic emission at room temperature, the intrinsic n-type conductivity, as well as the high resistence to harsh environment and the biocompatibility [31]. Furthermore, ZnO nanowires can be easily grown via vapor transport technique enabled by vapor-liquid-solid method (VLS), unlike nanowires based on many other compound semiconductors, which are typically synthetized through more complex chemical vapor deposition procedures [20]. Recent studies reported about extremely high photo-gain in ZnO nanowires assembled as UV photodetectors [32], as well as promising performances in chemical and bio sensing [33–36].

However, the large-scale applicability of ZnO nanowire devices is currently hindered by the limited control over their electrical properties. In particular, the strong influence of the surrounding environment on the device conductivity may be deleterious for photodetection applications, in which the measurement reproducibility should not be affected by the surrounding environment. Furthermore, the long persistence of the photoconductivity (PPC) after light excitation, whose origin is still under debate [37–39], affects deleteriosuly the recovery speed of ZnO nanowire based photodetectors. The development of an adequate model, which can precisely describe this effect, would be highly beneficial for an effective controll over the PPC. An additional issue concerns the eventual presence of localized defect levels in the band gap of the nanowire, which may drastically alter the charge transport and the photoconductivity properties of the entire device. Defect states are typically located at interfaces, such as the surface or contact regions, and they can easily form during the processing steps, which are required to produce the nanowire devices. Additionally, the specific modification of the device properties requires the optimization of various treatment procedures, whose impact on ZnO nanowire devices is still largely unexplored. This is for instance the case of ion beam implantation or plasma treatments on contacted ZnO nanowires or treatments in plasma atmospheres.

Furthermore, despite the large number of publications about chemical and bio sensing with ZnO nanowires, the specific detection mechanism is still unclear and the gas sensitivity at room temperature, as well as the gas selectivity (i.e. the ability to distinguish different molecular species), are quite poor. These facts reflect more in general that the impact of the surface on the charge transport properties of ZnO nanowires is not fully understood and reveal the need of further studies and investigations.

The beneficials from a deeper knowledge about the mentioned issues include in particular the possibility to selectively modify ZnO nanowire devices according to the specific wish and to enlarge their functionalities in view of improved applications.

1.2 Outline of the thesis

In this thesis, the photoconductivity and gas sensing properties of ZnO nanowires assembled into electronic devices are investigated.

The properties of ZnO as a material system in general and in the nanowire morphology in particular are introduced in chapter 2, along with the doping of semiconductor nanowires as well as the theory about the metal-semiconductor junction and the nanowire based field-effect transistor (FET). In the same chapter, the state of the art about the persistent photoconductivity and the gas sensing with ZnO is also presented. The experimental methods are described in chapter 3. These include the growth of the nanowires and the device preparation, as well as the subsequent procedures for the modification of the device properties and the exploited characterization techniques.

Chapter 4 is dedicated to the influence of defect levels on the sub-bandgap photoconductivtiy in ZnO nanowire field-effect transistors. In this configuration the population of defect levels, and therefore the device photoresponse below the band gap of ZnO, can be controlled by means of the gate voltage. The contribution of interfacial levels to the photoconductivity is investigated through a combined electrical and photoluminescence characterization.

Chapter 5 concerns the influence of the surrounding atmosphere on the above band gap photoconductivity properties of contacted ZnO nanowires. The photoresponse and the photoconductivity decay after UV excitation have been investigated in particular in vacuum, inert atmosphere and air. The dependence of the photoconduction process on the surrounding environment is discussed in terms of modulation of the surface band bending. A quantitative analysis of the persistent photoconductivity by means of the so-called Elovich equation for adsorption processes is then proposed.

Chapter 6 deals with the aluminum doping of contacted ZnO nanowires by means of ion beam implantation. At first, the optimal conditions for the post-implantation thermal activation of the aluminum ions as shallow donors are discussed. The impact of the implantation process on the optical and electrical properties of the devices is then investigated, giving particular emphasis on the change induced in the photoconduction process. The investigation is enriched and completed through the comparison with argon implanted devices.

Finally, in chapter 7 the hydrogen sensing properties of ZnO nanowire devices at room temperature are investigated. The response of the devices toward hydrogen molecules was measured under different gas concentration and a model for the sensing mechanism is proposed. Plasma treatments in argon and oxygen atmospheres as well as thermal annealing in oxygen are then explored as possible methods to enhance the gas sensitivity of the devices.

Detailed motivations of the performed experiments are presented at the beginning of the respective chapters, which are concluded with a summary of the most significant results. A conclusive summary of the thesis work and a corresponding outlook are given in chapter 8.

Chapter 2

Background and state of the art

2.1 Zinc oxide

2.1.1 Properties and applications

Zinc oxide (ZnO) is a one of the most important II-VI compound semiconductors and has been investigated since the first quarter of the last century [40]. The continuously growing interest arises from the possibility to grow high quality ZnO single crystals and nanostructures at relatively low production costs [41–45].

ZnO is a wide band gap semiconductor with a direct band gap of $E_g \sim 3.37$ eV at room temperature [46]. It crystallizes in the hexagonal wurzite structure, with every oxygen atom tetraedrically bound to four zinc atoms (Figure 2.1). This structure lacks an inversion plane perpendicular to the c-axis. Therefore, surfaces perpendicular to the c-axis show either Zn-polarity or O-polarity. Furthermore, the low symmetry of the wurzite crystal structure combined with the large electromechanical coupling gives rise to strong piezoelectric and pyroelectric properties [31]. Although the tetrahedral coordination reveals a partial covalent nature of the chemical bond, the high electronegativity difference between oxygen and zinc confers the crystal a strong ionic character [47]. As a consequence, the valence band is mainly determined by the overlap of completely filled 2p orbitals of O^{2-}, while the condution band is formed by empty orbitals of Zn^{2+}.

Despite the wide band gap, ZnO is typically characterized by spontaneous n-type conductivity at room temperature. According to density-functional-theory (DFT) calculations [48–51] and experimental evidences [52–54], hydrogen atoms incorporated during growth, either at interstitial (H_i) or substitutional positions (H_O), are considered the main donor

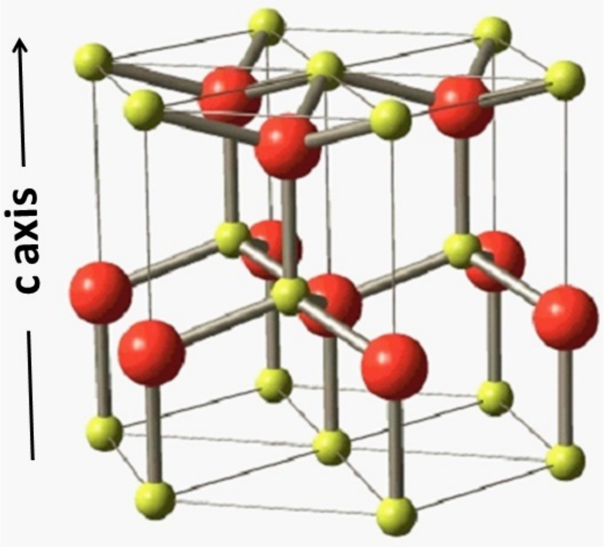

FIGURE 2.1: *Schematic rapresentation of the wurzite unit cell of ZnO, with every oxygen atom (in yellow) tetraedrically bound to four zinc atoms (in red). Adapted from [63].*

impurities in ZnO. The contribution from intrinsic defects to the spontaneous n-type conductivity is essentially negligible. Interstitial zinc atoms (Zn_i) or zinc antisites (Zn_O) are shallow donors, but they are present in ZnO only at low concentrations due to the high formation energy under n-type conditions [31]. Oxygen vacancies (V_O) give instead origin to deep donor levels [55, 56] and thus cannot provide electrons to the conduction band. Reported values for the donor concentration in nominally undoped ZnO bulk crystals and thin film range from 10^{16} cm^{-3} to 10^{19} cm^{-3} at room temperature, largely depending on the adopted growth technique [57–61]. The corresponding electron mobility, typically determined by means of Hall measurements, critically depends on the crystal quality. As such, it is strongly influenced by the growth tecnique, and in case of thin film structures also by the chosen growth substrate, whose eventual lattice mismatch with ZnO can induce strain and formation of grain boundaries [31]. The highest reported values of the electron mobility in ZnO bulk and thin film structures at room temperature are 205 [41] and 440 $cm^2 \cdot V^{-1} s^{-1}$ [62], respectively.

The research and application areas of ZnO are particularly wide and includes several fields of technology, such as photonics, electronics, spintronics, energy harvesting and sensing [45, 64]. Due to the wide band gap and the high excitonic binding energy of 60 meV, ZnO has been considered attractive for the development of opto-electronic devices and light emitting diodes in the near UV range, emerging as possible alternative material to GaN [65, 66]. The possibility to introduce a large amount of n-type dopants (see also

Section 2.1.4), combined with the high transparency in the infra-red and visible ranges of the spectrum, is particularly desirable in electronics for the production of transparent thin-film transistors [67–69] and in photovoltaics for the development of new transparent electrical contacts [70, 71]. On the other hand, band-gap engineering of ZnO over a broad energy range by alloying with Mg and Cd have been successfully demonstrated [72]. Doping of ZnO with magnetic impurities, like manganese, cobalt, or nickel, can be exploited for the production of spintronic devices, in which the electron spin is used for writing and reading informations [73]. The strong piezoelectricity allows the use of ZnO for piezoelectric energy harvesting and conversion, particularly for the production of electromechanically coupled sensors and actuators [25]. Furthermore, due to the high chemical stability, biocompatibility and the sensitivity of the surface to the environment conditions, ZnO have been successfully considered for gas and bio sensing application [30].

2.1.2 Growth

Growth of ZnO structures can be carried out by a large variety of methods. Bulk crystals are typically grown by hydrothermal techniques [42], vapor-phase transport [41] and and pressurized melt growth [74]. The growth of ZnO thin films can be accomplished by means of chemical vapor deposition (CVD) [59, 60], molecular-beam epitaxy (MBE) [57, 58], laser ablation [75] and sputtering [76]. High crystal quality ZnO films can be grown homoepitaxial on the native bulk crystal [57, 60], or on substrates with relatively small lattice mismatch, such as Al_2O_3 [77, 78]. Alternative substrates with higher lattice mismatch are for instance Si [79], SiC [78] and GaAs [80].

ZnO nanowires are often grown via the so-called metal catalyst assisted Vapor-Liquid-Solid mechanism (VLS), firstly described by Ellis and Wagner in 1964 concerning the growth of silicon whiskers [81]. In the VLS methods, a thin layer of a catalyst material (typically gold) is deposited on a substrate and heated up above its melting temperature. The source material is provided in vapor phase and gets incorporated into the liquid catalyst droplet, forming an alloy. When the alloy becomes saturated, the source material starts to segregate and in most of the cases re-crystallize at the interface between the catalyst and the substrate. As the incorporation proceeds, the segregation continues in vertical direction and the structure receives the typical shape of a nanowire, with diameter comparable with the size of the catalyst droplet. Typical growth rate are in the order of some several hundreds of nm/min up to few μm/min [82]. Beside the vertical growth promoted by the VLS mechanism, also growth in the lateral direction at significantly lower rate (nm/min) can be observed. This is caused by the direct deposition of the source material on the side walls of the nanowire and is therefore called Vapor-Solid (VS) growth. Since its activation requires typically high temperatures, the VLS mechanism enables typically growth techiques which require high temperatures, such as physical and chemical deposition, MBE and laser ablation. Additionally, also self-catalyzed growth techniques [83] as well as solution growth methods at relatively low temperatures [84] can be exploited fro the growth of ZnO nanowires, altough the crystal quality obtained in the latter case may be quite poor.

2.1.3 Properties of nanowires

The reduction of the structure dimensionality to the nanometric scale leads to a dramatic modifications of several properties of ZnO, which are strongly affected by the high surface to volume ratio of nanostructures [32, 85, 86]. In general, the impact of the surface on several properties of ZnO nanowires is revealed by their dependence on the nanowire diameter, as well as on the atmosphere surrounding the nanowire. Furthermore, they can be drastically modified by means of several surface treatments or surface functionalization employing various material components (polymers, organic molecules, nanoparticles, etc.).

The appearance of surface related effects in ZnO nanowires have been widely investigated by several theoretical and experimental studies. Photoluminescence measurements revealed for instance a strong dependence of the exciton related emission on the nanowire diameter [85]. In particular, the intensity of the surface exciton emission tends to increase as the diameter of the nanowire decreases. Moreover, a blue shift of the free exciton emission has been theoretically predicted [87] and experimentally observed [88, 89] in ultrathin nanowires with nanowire smaller than 10 nm. The effect has been attributed to the widening of the band gap, which is induced by the quantum confinement of the charge carriers in nanostructures with size comparable with the Bohr radius ($\approx$ 2 nm in ZnO) [90]. Enhancement of the surface exciton emission has been also observed by coating the nanowire with organic and inorganic compounds [91], which induce passivation of surface states. On the other hand, nanowires coated with metals exhibite reduced intensity of the surface excitonic emission [92], due to the formation of metal-induced gap states in the surface region [93], which leads to a higher electron trapping rate.

Size dependent transport properties in ZnO nanowires have been observed in dark conditions as well as under light excitation [86, 94–96]. Electron mobility values at room temperature for nanowires thinner than 200 nm range from 5 $cm^2 \cdot V^{-1} s^{-1}$ to 75 $cm^2 \cdot V^{-1} s^{-1}$, which are much lower than that typically observed in bulk and thin film structures. This effect has been attributed to the enhanced surface scattering and charge trapping at surface defects, experienced by charge carriers as a result of the diameter shrinking. Comparable results have been observed under photoexcitation conditions by means of scanning photocurrent microscopy measurements, which revealed a significant decrease of the minority carrier diffusion length for decreasing nanowire diameter [97]. However, the electron mobility in ZnO nanowire based field effect transistors [95] is typically higher than that measured in corresponding transistors based on thin films (0.01-10 $cm^2{\cdot}V^{-1}s^{-1}$) [98, 99]. The electron mobility depends additionally on the environment sorrounding the nanowire, being lower in oxygen rich atmopshere than in inert environments or at reduced pressure [100]. Such dependence can be suppressed by coating the surface with a variety of molecular compounds [95, 96, 100–103]. Due to the passivation of surface states, the electron mobility in coated nanowires can reach much higher values than in bare nanowires, up to 1000 $cm^2{\cdot}V^{-1}s^{-1}$ [95].

The dependence of the electron mobility on the surrounding atmosphere reflects a more general influence of the surrounding environment on the transport properties of ZnO nanowires. Indeed, due to the high surface to volume ratio, the interaction of the surface with gas and bio-molecules involves a large fraction of the nanowire body. Such effect can be beneficially exploited in several applications, such as for instance chemical and bio-sensing [14], allowing particularly high sensitivity for the detection of molecular species in gas and in liquid phase [30, 104]. Significant examples are the successful detection of the protein streptavidin down to a concentration of 2.5 nM [105] or the detection limit of 10 ppb in case of NO_2 sensing, which is the lowest value achieved in gas sensing applications with nanowire based sensors [106]. Size dependent gas sensitivity has been reported in case of oxygen [94] and hydrogen sensing [35] with ZnO nanowires, revealing in both cases a three time enhancement of the response by shrinking the diameter from 200 to 100 nm. Further enhancement of the sensitivity can be achieved by surface functionalization with noble metal nanoparticles or organic molecules. Noble metal nanoparticles promote the catalytic dissociation of gas molecules into the atomic components, which interact more strongly with the ZnO surface [34, 107]. Organic molecules are typically used for the covalent binding with specific bio-molecules, which allows the development of highly selective sensors for label free bio-sensing [36]. Furthermore, in contrast to traditional polycristalline film gas sensors, which suffer from material instabilities due to grain coalescence [108] and must be heated up to optimal operation temperatures (100 - 400 °C) by external heating elements [109], sensors based on ZnO nanowires ensure long-term stability and considerable reduction in terms of power consumption (up to few tens of μW) and device complexity. In particular, the former potentiality is guaranteed by the higher crystal quality of the nanowires and the substantal absence of grain boundaries, while the latter is based on the possibility to exploit self heating effects, favored by the confinement of the structure and the weak thermal coupling of the nanowire with the substrate and the electrodes, which leads to a reduction of the heat loss [110, 111].

The nanowire geometry leads also to a dramatic increase of the UV photoconductivity gain up to 10^8 [32], which represents a five orders of magnitude enhancement in comparison to ZnO thin film photodetectors [71]. Such extremely high gain has been attributed to the enhanced separation efficiency of photogenerated charge carriers, promoted by the reduced dimensionality of nanowires, and could in principle allow reaching single-photon detectivity in homogeneous single nanowires [112, 113]. In particular, increase of the UV photoconductivity gain have been observed in ZnO nanowires as a function of the nanowire diameter shrinking [114]. Enhancement of the UV photoresponse, up to three orders of magnitude [115, 116], has been also achieved by functionalizing the nanowire surface with polymers and organic molecules [115, 117, 118] and noble metal nanoparticles [119]. Furthermore, decoration of the nanowire surface with noble metal nanoparticles [120] and semiconductor quantum dots [121, 122] can considerably enlarge the photosensitivity of ZnO based photodetectors toward the visible and infrared spectral ranges.

2.1.4 Doping of semiconductor nanowires

Doping of semiconductors is a fundamental process for the modification of the electric, magnetic and optical properties of materials. The controlled introduction of desired impurities in semiconductor nanowires can be achieved via three different methods: doping during growth or subsequent doping either by ion beam implantation or diffusion techniques. Diffusion of dopants after growth offers the lowest controllability and requires typically suitable precursors and high temperature procedures. The latter issue is particularly disadvantageous for nanowires, because their high surface/volume ratio leads to higher thermal instability and eventual degradation at the required temperatures [123]. Doping during growth has been successfully achieved in case of relatively large Si nanowires [124], but inhomogeneous dopant distribution occurs in thinner nanowires and more generally in nanowires based on other materials [125]. Additionally, morphological and structural changes have been observed in compound semicondutor nanowires doped during growth [126] and the solubility of several elements in the cristalline matrix is limited.

Ion beam implantation, which is based on the injection of ions of the desired impurities at high energy, permits instead to overcome this limitations. In particular, it ensures the availability of every element beyond the solubility limit and a precise control of the dopant distribution, which can be tuned by specifically selecting the ion energy and fluence [123]. The key issue of the implantation process consists in the loss of ion energy, induced by their interaction with the electrons and the nuclei in the matter. The energy loss, or stopping power, critically depends on the charge and the mass of ions, as well as on the composition of the target material [123]. However, the main disadvantage of ion implantation is the generation of defects in the crystal during the implantation process. Therefore, post-implantation annealing treatments are typically required, in order to recover the original crystal structure.

The modification of the electrical conductivity in ZnO via doping procedures ensures higher potentialities for this material system in several application fields. Increase of the n-type conductivity through the controlled introduction of shallow donor impurities leads for instance to superior performances of ZnO as transparent conductive oxide and for sensing applications. On the other hand, the possibility to introduce shallow acceptors and to achieve consequently p-type doping can open up various possibilities in terms of optoelectronic applications, in particular concerning the realization of ZnO based light emitting diodes and lasers.

Potential shallow donors in ZnO are B, Al, Ga and In as Zn substitutional, as well as Cl and F as O sustitutional [127]. Especially doping with Al and Ga has been attempted by many groups. The highest reported values for the electron density in Al and Ga doped ZnO nanowires are respectively around 10^{20} cm^{-3} and 10^{19} cm^{-3} [128–130], which are slightly lower than that observed in corresponding ZnO thin films (up to 10^{21} cm^{-3}) [131, 132]. However, decrease in the mobility for increasing dopant concentration has been observed in Al:ZnO nanowires [128], while there is no evidence of such effect in Ga:ZnO nanowires [129]. This can be attributed to the fact that the substitution of Zn with Ga does not introduce large distorsion in the lattice, because the bond length of Ga-O is nearly the same of Zn-O [133, 134].

While n-type doping of ZnO can be achieved straightforward, p-type doping suffers from lack of stability and reproducibility. These difficulties are caused by a variety of factors, including compensation effects, low solubitily of the dopants and high ionization energy of acceptor states [127]. Among compensation sources, the main contributions are represented by the intrinsic n-type background and the presence of intrinsic defects, such as V_O and Zn_i. Efforts to drastically reduce the intrinsic n-type background have not been successfull yet, since the complete elimination of hydrogen impurities during any growth procedure is practically impossible. Additionally, the formation of the mentioned intrinsic defects is quite likely during p-type doping, because their fomation energy is relatively low when the Fermi level approaches the valence band [135]. As such, most of the efforts to p-type dope ZnO with group-V elements has not lead to the desired results. It has been claimed that such limitations can be overcome by simultaneous introduction of n- and p-type dopants [136]. This method, which is known as "co-doping", should enhance the solubiltity of n-type dopants and partially limit the formation of compensating intrinsic defects, by keeping the Fermi level relatively far away from the valence band and increasing consequently their formation energy. However, no reliable and reproducible experimental results have been reported yet.

2.2 Surface properties of semiconductors

2.2.1 Pinning of the Fermi level

The surface of a crystal corresponds to a sudden break of the lattice symmetry and determines the formation of a large number of dangling bonds. These generate typically surface states, which are located in the band gap and can act either as charge acceptors or donors. In a n-type semiconductor, such as ZnO, surface defects which act as charge acceptors can localize electrons from the conduction band, lowering their energy and leaving unbalanced positive ions in the inner part of the crystal. As a result, the Fermi level gets pinned at these surface states and the valence and conduction bands bend upward, inducing the formation of a depletion region in the proximity of the surface (Figure 2.2).

The width of such depletion region depends in general on the height of the surface barrier ϕ and the electron density N trough the following expression [137]:

$$z_{dep} = \sqrt{\frac{2\epsilon\epsilon_0\phi}{e^2N}}, \tag{2.1}$$

where ϵ_0 and ϵ are respectively the vacuum and the semiconductor dielectric permittivities, e is the electron charge and ϕ is related to the density of occupated surface states N_s:

$$\phi = \frac{e^2N_s^2}{2\epsilon\epsilon_0N}. \tag{2.2}$$

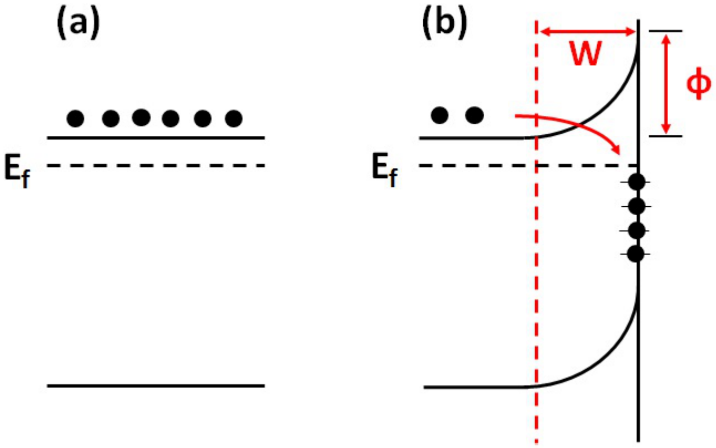

Figure 2.2: *Schematic representation of the Fermi level pinning at the surface in n-type semiconductors, induced by acceptor surface states. The conduction and valence bands, which are flat and equidinstant fron the Fermi level E_f in the bulk (a), are instead bent in the proximity of the surface (b). The Fermi level is pinned at sthe surface due to the presence of midgap surface states, which trap electrons from the conduction band. Accumulation of electrons at the surface results in the formation of a built-in electric potential ϕ and a corresponding depletion region* W.

2.2.2 Surface band bending in ZnO nanowires

Despite the simplicity of equation 2.1, the determination of z_{dep} can be particulary complex in case of ZnO nanowires, because the height of the surface barrier ϕ depends on several factors, such as nanowire diameter [138], surface roughness [139], molecular adsorption [139] and surface functionalization [119, 140, 141]. Moreover, eventual processing steps typically required for the production of ZnO nanowire based devices can lead to a further modification of the surface properties, leaving the values of ϕ and correspondingly z_{dep} largely unpredictable.

Experimental techniques are therefore required, in order to specifically investigate the surface band bending properties in ZnO nanowires. Among these, ultraviolet photoelectron spectroscopy [142], Kelvin probe force microscopy [143] and photoluminescence spectroscopy [144] are the most exploited contactless and nondestructive methods. Studies available in literature report values of ϕ ranging from few tenths of eV [145, 146] up to 1.5 eV [147], which correspond to depletion widths up to several tens of nm. However, the latter critically depend on the electron density, which varies up one order of magnitude in the reported works. In particular, a reduction of the depletion width up to 30 % has been observed after thermal desoprtion treatment, indicating a strong dependence of the surface band bending on the presence of adsorbed species [147]. This reveals that the surface band bending properties in ZnO nanowires do not depend exclusively on the density of intrinsic surface states, but also on the formation of defect levels induced by adsorption processes. Among such levels, those related to the adsorption of oxygen molecules are the most dominant in ZnO, reaching density up to 10^{12} - 10^{13} cm^{-2} [148, 149]. They are located at various positions of the band gap, ranging from 0.5 eV above the valence band [150] up to 0.7 eV below the conduction band [151] and act as electron acceptors. Therefore, the density of trapped electrons at the surface can be modulated by the oxygen concentration in the atmosphere surrounding the nanowire, resulting in the enlargement or reduction of the corresponding surface depletion region. This process can drastically affect the transport properties of ZnO nanowires, because the depletion region can represent a large percentage of the nanowire diameter. A strong dependence of several physical processes (interaction with gas and bio-molecules, catalytic activity, photo-response, etc.) involving ZnO nanowires on the atmosphere conditions is thus to expect.

2.3 Metal - Semiconductor interface

Typically, the properties of contacted semiconductor nanowires do not depend exclusively on the nanowire itself, but can be largely influenced by the specific features of the interface to metallic electrodes. A preliminary knowledge of the properties of a metal - semicondutor junction is therefore required, in order to predict and deeply understand electric and transport properties of the overall device and to eventually introduce specific modifications (functionalization, doping, etc.) in view of possible applications. This is particularly important in case of nanowire based devices, because due to the reduce size of the structure, the contacts can dramatically impact the electric properties of the overall device. Since a detailed theoretical description of the properties of a metal - semiconductor junction can be found in several well known text books [137, 152, 153], only few general concepts will be recalled, which are fundamental for the comprehension of the electrical properties of ZnO nanowire based electric devices.

In general, when a metal and a n-type semiconductor are placed in contact, a net flow of electrons between the two materials takes place, until the respective Fermi levels line up. If the Fermi level of the semiconductor is lower than the work function of the metal, the electrons flow from the former into the latter. As a consequence, the valence and the conduction bands of the semiconductor bend upwards in the proximity of the interface and a depletion region appears, as shown in Figure 2.3. The height of the barrier at the

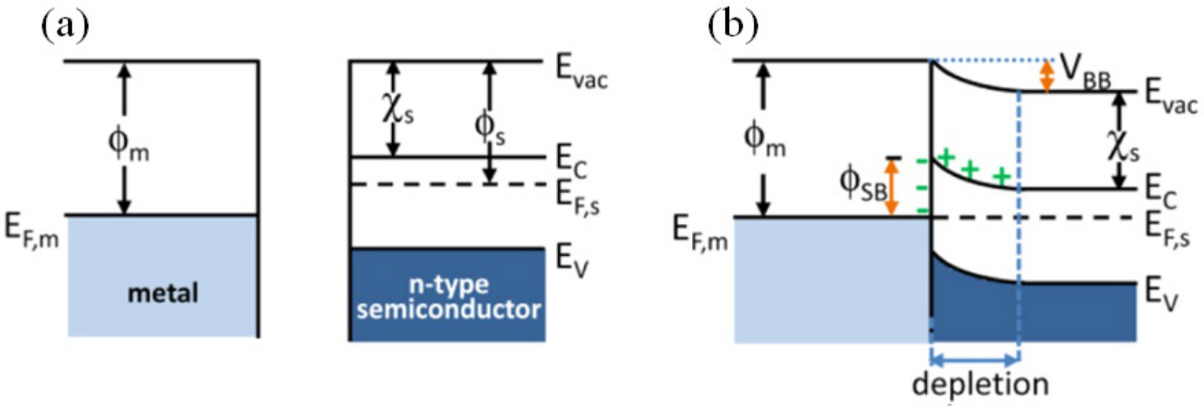

FIGURE 2.3: *Schematic representation of the band diagram of a metal and a n-type semiconductor before (a) and after contact (b), in case of $\phi_m > \phi_s$. The electrons flow from the semiconductor into the metal, until the Fermi levels line up. As a consequence, a depletion region forms in the semiconductor in the proximity of the interface. Such junction is called Schotty contact. Both Figures are adapted from [154].*

interface is given by the difference between the work function of the metal ϕ_m and the electron affinity of the semiconductor χ_s:

$$\Phi_{SB} = \phi_m - \chi_s. \tag{2.3}$$

The width of the depletion region depends on the dielectric permittivity ϵ, the charge carrier density of the semiconductor N and the built-in voltage ($V_{BB} = \phi_m$ - ϕ_s) through the following expression:

$$z_{SB} = \sqrt{\frac{2\epsilon V_{BB}}{e^2 N}}. \tag{2.4}$$

Current across the juction can be induced by applying an external voltage different ΔV. It mainly consists in the flow of majority carriers and can be distinguished in three contributions: diffusion from the semiconductor into the metal, thermoionic emission in the opposite direction and tunneling through the barrier. If the semiconductor is not heavily doped, the latter component can be neglected and the current is expressed by the following equation:

$$I = A^* T^2 e^{-\frac{\Phi_{SB}}{kT}}(e^{\frac{e\Delta V}{kT}} - 1), \tag{2.5}$$

where A^* is the Richardson constant, k is the Boltzmann constant, and T is the absolute temperature. A junction with such properties is called Schottky contact and is typically characterized by a high contact resistivity and a rectified profile of the current as a function of the voltage difference. From this perspective, it resembles the main characteristics of a pn junction, although in the latter case the current consists in the flow of minority carriers.

On the contrary, when the Fermi level of the semiconductor is higher than the work function of the metal, an accumulation of electrons in the proximity of the interface takes place, giving rise to a low resistive ohmic contact. Ohmic contacts can be formed also when the Fermi level of the semiconductor is lower than the work function of the metal, if the semiconductor is heavily doped. Under this condition, the width of the depletion region shrinks and the electrons can tunnel through the junction without any barrier.

A more accurate and realistic description of metal/semiconductor interfaces is complicated by the presence of surface states, which pin the Fermi level in the band gap of the semiconductor. As a result of the Fermi level pinning, a depletion region in the proximity of the semiconductor surface appears and the contact correspondingly tends to show Schottky properties, independently on the specific choice of the metal.

2.4 Nanowire field-effect transistors

The field-effect transistor is a three-terminal device in which a tranverse electric field generated by the gate electrode controls the current flowing in the semiconducting channel between the source and drain terminals [152]. In the so called metal oxide field-effect transistor (MOSFET), the gate is capacitevely coupled to the semiconductor through a dielectric layer, typically SiO_2 or another insulators with high dielectric constant, such as for instance HfO_2 or Al_2O_3.

The modulation of the semiconductor conductivity channel enabled by electric gating is based on the shift of the conduction band in respect to the Fermi level, as illustrated in Figure 2.4 (a). In particular, the separation between the conduction band and the Fermi level of the semiconductor increases when the gate voltage is negative, while it decreases under positive gating. Considering n-type semiconductors, the conductivity rises in the latter case, as more electrons are available in the conduction band, while the channel tends to become highly resistive in the former one. The opposite occurs in case of p-type semiconductors. For this reason, field effect transistors are widely used in electronics as electric switches and amplifiers.

Field effect transistors based on ZnO nanowires have been intesively investigated in the last decade [22, 86, 94–96]. Most of their properties, such as the field-effect mobility and

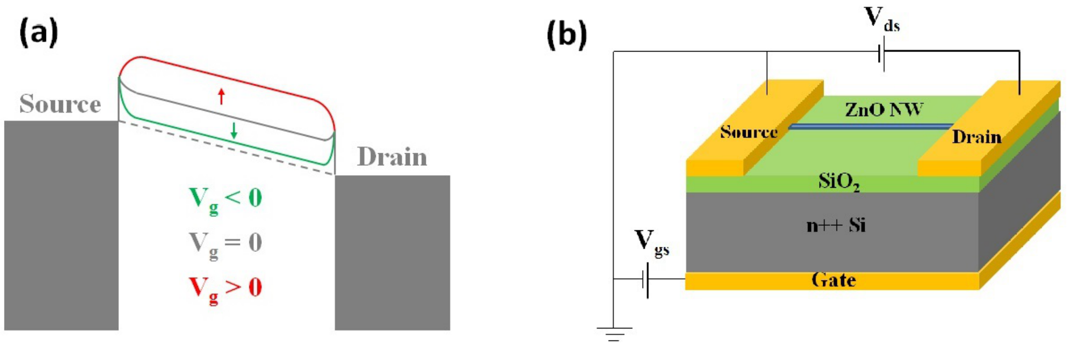

Figure 2.4: *Schematic illustration of electrostatic gating effect in a FET (a). The gate electric field induces a shift of the semiconductor conduction band respect to the Fermi level (dashed line), reducing the distance when the gate voltage is positive and increasing it when the gate voltage is negative. In a n-type semiconductor, electrons accumulates in the conduction band in the formar case, while they are depleted from the semiconductor a positive gate voltage accumulated electrons in conduction band, while a negative gate voltage depletes the channel. In (b) the back gate configuration is schematically illustrated for a nanowire based FET.*

ON/OFF current ratio critically depend on the fabricated gate structure. Among various gate structures explored, four majour types can be identified: back, top, side and vertical surrounding gate [22]. The back gate configuration is the most commonly adopted, due to its fabrication semplicity. As illustrated in Figure 2.4 (b), the nanowire channel lies typically on the dielectric layer and the underlying highly doped substarte is used as a back gate. Typical values of the field-effect mobility reported for this configuration range between 3 and 80 $cm^2{\cdot}V^{-1}s^{-1}$ and ON/OFF current ratio around 10^4 - 10^6 [22]. However, it is unconvenient for efficient device integration and does not offer precise control of individual channel segment. However, this limitations can be overcome by considering other configurations. In particular, the fabrication of vertically oriented NW FETs ensures a ultrahigh integration density [155]. Possible local gating is offered by the top gate configuration, in which a localized gate electric field requires less strength in order to effciently modulate the channel conduction [156]. As a result, ON/OFF ratio up to 10^7 can be achieved. Excellent gating performances can be also obtained with side gate structures, in which air acts as dielectric gap between the gate and the ZnO. This allows singnificant reduction of leakage currents and low dielectric thickness, resulting in extremely high field effect mobilities up to 1000 $cm^2{\cdot}V^{-1}s^{-1}$ [157].

Thanks to these novel geometries, NW FETs are expected to ensure better operation performances than planar devices [158], having potential application as buliding blocks in future integrated circuits, such as for instance microprocessors and non-volatile memories. Additionally, the observed dependence of the UV photoresponse and the molecular detection process on the gate voltage [33, 159] can be exploited for the development of photodetectors as well as chemical sensors based on ZnO NW FETs working in optimized conditions.

2.5 Persistence of the photoconductivity

The photoconductivity consists the increase of the electrical conductivity of a semiconductor or insulating material under electromagnetic radiation. The effect is based on the increase in the free charge carriers density, caused by the absorbtion of photons in the crystal. Generation of free charge carriers occurs in an ideal semiconductor crystal when the photo energy exceeds the band gap of the material. Electrons are promoted to the conduction band, while holes are left in the valence band. Both charge carriers contribute to the conduction process, although the hole mobility is typically lower than the electron one. Additionally, in a real crystal also electrons and holes localized at defect states can be promoted to the respective delocalized band and photoconductivity can be therefore observed also under sub-bandgap excitation.

After excitation, the photoconductivity persists until excited charge carriers recombine. The rate of the photocurrent decay is therefore determined by the charge carrier lifetime. In an ideal semiconducor, this is typically not longer than 1 ns. However, in a real semiconductor several processes, such as charge trapping at various defect levels or electron - hole separation, may prolong it by several orders of magnitude, giving origin to the persistence of the photoconductivity. The slow recovery of the conductivity in dark, which can proceed for several minutes or hours, has been observed in bulk crystals [160], thin films [161] and nanostructures [32] of several material systems, including silicon [162], metal oxides [150] and III-V [138, 163].

The effect was originally observed at the end of the fifties by Melnick [164], who conducted above band gap photoconductivity experiments on sintered ZnO. The study revealed a strong dependence of the photocurrent decay on the surrounding atmosphere, showing in particular a slower recovery of the dark current in inert environments or vacuum than under oxygen rich conditions. These results indicated a strong inhibition of the charge carrier recombination in the bulk of the sample, since this is substantially insensitive to the environment conditions. The reduced recombination probability was attributed to the separation of photogenerated electron-hole pairs during light excitation, induced by

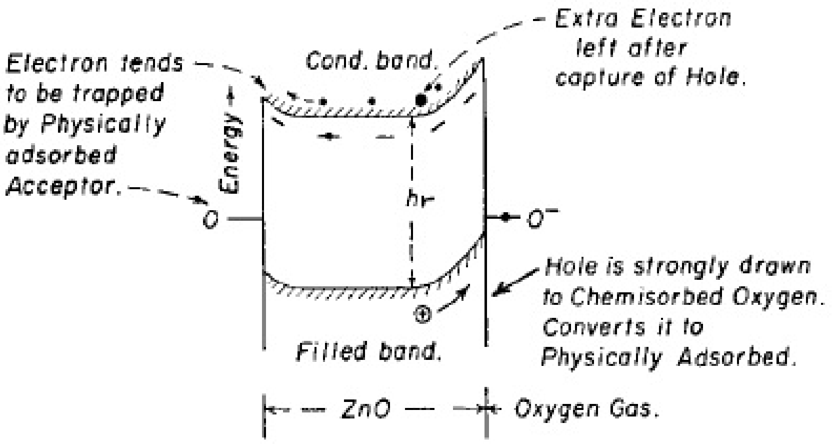

Figure 2.5: *Physical model of the hole-induced oxygen desorption from the ZnO surface during above band gap excitation. The process is caused by the migration of the photogenerated holes toward the surface, driven of the upward surface band bending. The interaction of the holes with the chemisorbed oxygen molecules convert them into weakly bound physisorbed species, which can easily desorb. As a result of this process unpaired photogenerated electrons are left in the conduction band. Representation taken from [164].*

the upward surface band bending and the corresponding migration of holes toward the surface (Figure 2.5). Since holes, which are accumulated at the surface, can promote the desoption of ionosorbed oxygen from the surface, it was then suggested that the decay of the photoconducitivity after light excitation is driven by the slow trapping at the surface of unpaired electrons from the conduction band, assisted by the simultaneous re-adsorption of oxygen molecules. Such interpretation of the persistent photoconductivity as a purely surface related effect assumed progressively popularity and has been adopted in later works concerning the photoconductivity properties of several ZnO structures [32, 37, 39, 161]. The impact of the surface on the charge carrier relaxation after light excitation is expected to play a fundamental role especially in nanostructured ZnO, due to the high surface to volume ratio and the confined dynamics of the charge carriers. However, no systematic studies about the influence of the surrounding environment on the PPC have been conducted so far in case of ZnO nanowires.

On the other hand, some recent experimental [165–167] and theoretical studies [55, 168] revealed that also bulk defects can contribute to the PPC. For instance, oxygen vacancies, zinc interstitial and grain boundaries, are supposed to act as hole traps [169–171], which can cause a reduction of the electron-hole recombination probability, determining consequently the appearence of the PPC. Furthermore, some authors consider the surface related model, based on the hole-induced oxygen desoprtion, not compatible with the observation of the PPC after below band gap excitation [167, 172], which does not lead to the generatation of electron-hole pairs. In particular, it has been suggested that the slow relaxation of photogenerated electrons is related to the occupation of metastable states resonant with the conduction band [168]. This process occurs typically after excitation of electrons from the ground state of oxygen vacancies, which is located in ZnO approximately 1 eV above the valence band maximunm, to excited states located in the conduction band [50]. As schematically illustrated in figure 2.6, this transition determines a large lattice relaxation in the proximity of the vacancy [55] and leads consequently to the formation of such metastable states. After light excitation, a quick relaxation of the electrons to the ground state of the vacancy is hindered by the presence of a thermal barrier ΔE, which is supposed to contribute to the PPC. Metastable excited states of oxygen vacancies resonant with the conduction band have been proposed as responsible defects for the PPC also in $SrTiO_3$ [173] and might be involved more in general also in other oxides. Hole trapping processes and resonance of metastable states with the conduction band have been identified as responsible factors for the PPC also in GaN [163].

Furthermore, defect levels responsible for the slow relaxation of charge carriers in semiconductor based devices can be located also in the proximity of contacts and interface regions. These have been identified for instance in ZnO NW FETs at the interface between ZnO and the gate dielectric [174] and in GaN thin films or AlGaN/GaN heterostructures at the interface with various growth substrates, such as sapphire and SiC [175].

Therefore, a large variety of factors can simultaneouly contribute to the PPC. As a consequence, a general unified and accepted model for the description of the phenomenon is still missing. Indeed, several approaches for the quantitative analysis of the photoconducivity decay are available in literature. The most commonly adopted are typically based on single or multiple exponential fitting functions, in the simple as well as in the stretched form. The latter, which is also known as Kohlrausch function, is typically expressed as:

$$I = Ae^{-(\frac{t}{\tau})^{\beta}}, \tag{2.6}$$

where A is the value of the photocurrent immediately after light excitation, τ is the relaxation time and β falls into a range between 0 and 1. The steched exponential is a flexible fitting function, which was originally used for the description of decay processes in presence of multiple energy transfer mechanisms [176]. As β tends to 1, the function appraoches a classical simple exponential and distinct relaxation processes become indistinguishable. However, despite its popularity, the use of such function for the description of the PPC is only rarely adeguatamente motivated, being mostly exploited only for its

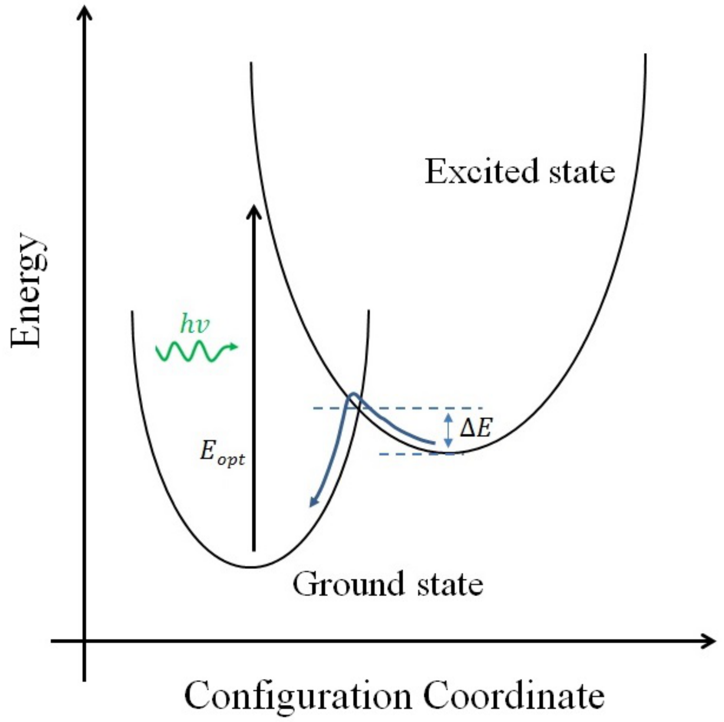

FIGURE 2.6: *Configuration diagram of an oxygen vacancy in ZnO, describing the optical transition of an electron from the ground state to an excited state resonant with the conduction band of ZnO. Due to the large crystal relaxation occurring immediately the transition, the excited state acts as a metastable conductive state and the recapture to the ground state is hindered by a thermal barrier. As a result, the persistent photoconductivity may appear.*

capability to fit experimental data. More realistic analysis procedures are therefore required, in order to obtain from the data evaluation fitting parameters with a reliable physical meaning. Moreover, a deeper comprehension of the underlying physical mechansims represents the prerequisite for a reliable control of the PPC, which is indesirable in view of photodetection applications, but can be instead beneficially exploited for the development of non-volatile memory or optical switches and integrators [177].

2.6 Chemical sensing with ZnO

The detection of gas molecules using sensors based on ZnO and more in general on semiconductor materials is based on the change of specific physical properties of the sensor, induced by the adsorption of the molecules on the semiconductor surface [178]. In particular, the detection can be performed by measuring the change in electrical conductivity [30], capacitance [179], work function [180], mass [181], optical properties [182] or reaction energy released by the gas/solid interaction [183]. Sensors based on the change in conductivity are particularly interesting, because of the high sensitivity, low-cost production and semplicity of device configuration [184].

It is generally assumed that the change in conductivity of ZnO upon molecular adsorption is caused by an electron transfer occuring between the gas molecules and the ZnO surface [185]. In particular, it is believed that for reducing gases such as C_2H_6O, H_2 and CO, whose adsorption on ZnO causes an increase of the conductivity [35, 186, 187], this chemical reaction is mediated by the ionosorbed oxygen always present at the surface of ZnO, either in the molecular (${O_2}^-$) or in the atomic form (O^- and O^{2-}) [185]. The latter one, which is the most abundant at room temperature [188] and on non stochiometric surface with lattice oxygen deficiency [189], is the most reactive ionic oxygen species and interacts easily with reducing gases according to the following reaction formula [185]:

$$X + mO^{-a} \rightarrow Y + ne^{-}, \tag{2.7}$$

where X is the reacting gas, a = 1,2, m = 1,2,... ; Y is the reaction product and n = 1,2,... is the number of free electrons. As a result of this reaction, electrons previously trapped at the oxygen chemisortion sites are released into the conduction band of ZnO and contribute to the increase of the nanowire conductivity. On the contrary, the adsorption of oxiding gases such as NO_2 and O_3 promotes the trapping of electrons at the surface and determines consequently a decrease of the nanowire conductivity [190].

The described model is the most commonly adopted in literature for the interpretation of the gas sensing process [185]. However, it must be noticed that it has mainly a speculative character, in particular due to the lack of experimental techniques able to probe the dynamics of the detection process. Additionally, most of the theoretical studies conducted so far do not describe the physical system with a sufficient level of accuracy, since neither the ionosorbed oxygen coverage nor the intrinsic n-type conductivity of ZnO are usually included as parameters of the simulation procedure. As such, they cannot provide conclusive support to the proposed mechanism. It is also under dabate whether the charge transfer between the gas molecules and the nanowire sensor is necessarely mediated by chemisorbed oxygen ions, as it was claimed that some molecular species, including H_2 and C_2H_6O might exchange electrons with ZnO by direct interaction with surface lattice atoms [186]. Furthermore, the interaction gas/ZnO can eventually lead to surface reconstruction effects and more in general to a local change of bond angles and lengths, which may induce further modification of the surface electronic properties [191]. These considerations reflect the fact that the interaction of gas molecules with a semicondutor surface is a complex process, which can result from the concomitant occurrence of several contributions, largely depending on factors like temperature, activation energy and stoichiometry of the surface [30]. From this perspective, the description of the sensing mechanism through the reaction shown in equation 2.7 should be just intended as a partial and semplified picture of a more complex process.

Chapter 3

Experimental

3.1 Nanowire growth

The ZnO nanowires employed in within the work were grown via VLS method in a horizontal tube furnace [192–196]. The source material, a ZnO fine powder, was typically placed in the middle part of the furnace and heated up at 1350 °C in order to induce its evaporation. Silicon substrates sputtered with 10 nm Au were positioned downstream in the colder region of the furnace, at temperature comprised between 1100 and 950°C. The nanowires were grown under argon flow of 50 sccm, at pressure of 100 mbar. Typical growth times were coprised between 30 and 60 min. Under such conditions, the growth procedure results in a dense and disordered ensemble of nanowires, with length up to 40 μm and diameter ranging between 100 and 300 nm. A typical example is shown in Figure 3.1. Further details about the process and the influence of growth parameters (temperature, pressure, growth time, etc.) can be found in previous works [192–196].

3.2 Photolithography

The production of nanowire based electric devices proceeded then with electrical contacts were defined via photolithography and metal deposition. The complete procedure required to assemble the ZnO nanowire field effect transistors is based on four main steps, which are schematically illustrated in Figure 3.2 (a). They consist in the mechanical imprinting of the nanowires, photolithography, metal deposition and electric bonding. The core of this process is the photolithography, which is a well-known technique exploited in semiconductor industry for the fabrication of electric contacts down to the micrometric scale [197]. In this work, the nanowires were at first transferred via mechanical imprinting

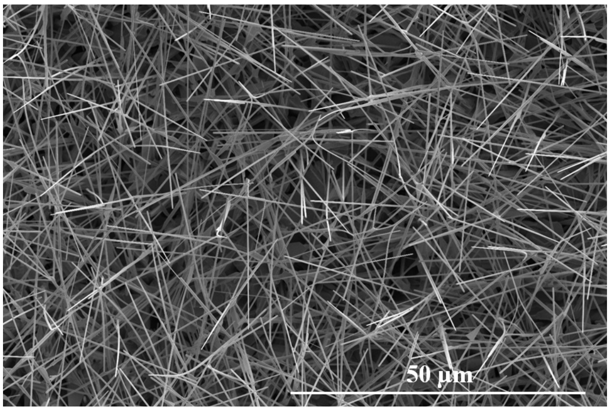

Figure 3.1: *Typical ensamble of ZnO nanowires grown on Au-coated Si substrates via vapor transport technique enabled by the VLS method. The nanowires are up to 40 micrometer long, with diameter ranging between 100 and 300 nm.*

from the growth substrate to heavily doped Si substrates with 850 nm SiO_2 on top. Low resistivity of the Si substrates ($1 \sim 10$ Ωcm) was required to employ them as a back gate electrodes in the subsequent FET measurements. The image reversal photo-resist TI35ES from MicroChemicals Gmbh [199] was then uniformily distributed via spin-coating and the photolithography was performed, in order to define on each substrate a pattern of fifteen position units for the electrodes. More in detail, the photolitography procedure with the employed photoresist consists in six steps. At first, the substrates were exposed to the UV light for 25 s through the photolithography mask. This step makes the exposed part of the photoresist soluble, while leaves the unexposed one unsoluble. A reversal bake at 125 °C for 120 s was then performed, in order to reverse such properties and to leave the previously exposed portion of the photo-resist inert. The following UV irradiation without mask for 90 s makes finally the initially unexposed region soluble. The latter was then removed by the developing process.

The subsequent deposition of Ti and Au was performed by electron – beam evaporation. This technique is based on the evaporation of the source materials induced by a high energetic electron beam. The procedure was performed in a sealed chamber at pressure of 10^{-7} mbar, in order to prevent oxidation of Ti. The thickness of the deposited metals was measured by a quarzoscillator. Although Ti is one order of magnitude less conductive than Au, its deposition is known to considerably enhance as an intermediate layer the poor adherence of Au on SiO_2 [200]. In the frame of this thesis, the stability of the contacts was investigated as a function of the Ti thickness. The study revealed that 10 nm Ti are sufficient to provide stable and durable contacts. Such thickness was therefore chosen as a standard thickness for the Ti layer. After Ti evaporation, 150 nm Au were

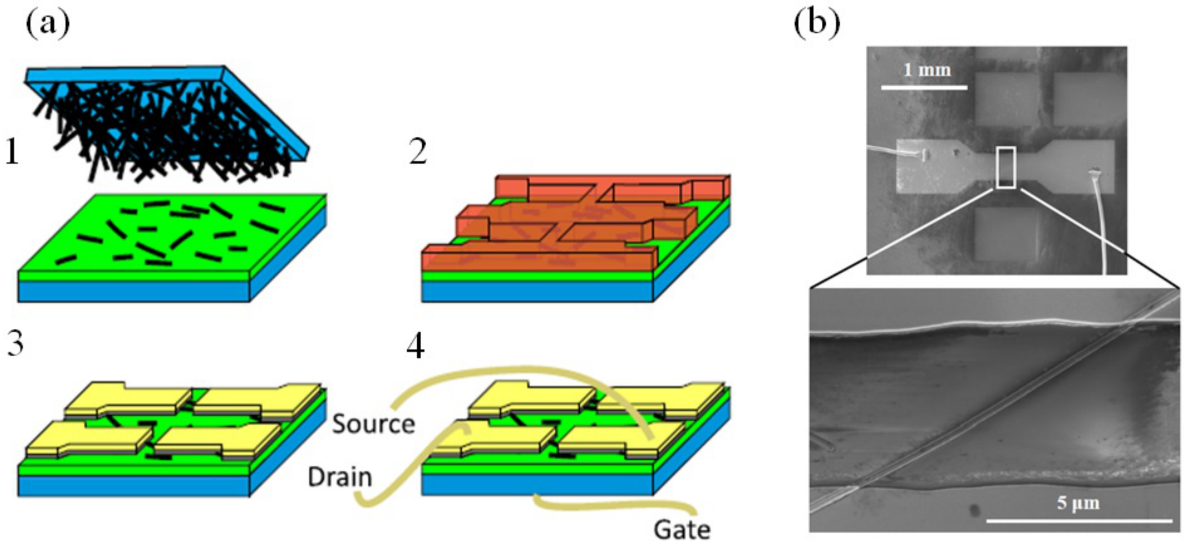

FIGURE 3.2: *Schematic representation of the sample preparation procedure (a), consisting in the mechanical imprinting of ZnO nanowire on a Si/SiO*$_2$ *substrate (1), photolithography (2), metal deposition (3) and electric bonding (4) (adapted from [198]). (b) Scanning electron microscopy (SEM) image of a typical single ZnO nanowire device investigated in this work. It consists of two Ti/Au electrodes separadey by a gap of 5 μm and bridged by a single nanowire. The electrodes are electrically bonded to a commercial chip, which can be mounted in a sealed chamber for measurements under different atmospheres.*

deposited and the undeveloped photoresist was removed by lift - off in aceton. Finally, the devices were bonded to a commercial chip carrier by a thermo-sonic wedge bonding procedure. Figure 3.2 (b) shows a top view of a typical sample, in which a single nanowire bridges the electrodes, separated by a gap of 5 μm.

3.3 Electrical characterization

3.3.1 Setup

For all electrical measurements performed in the frame of this thesis, a Keithley 237 [201] source measurement unit (SMU) was used as voltage generator and amperemeter with pA sensitivity. Computerized measurements were allowed by a LabView software written by Steffen Milz [196].

Depending on the specific purpose, the electrical measurements were carrier out either in a home made sealed chamber or in a EP6 probe station by Süss MicroTec [202], both connected with the SMU.

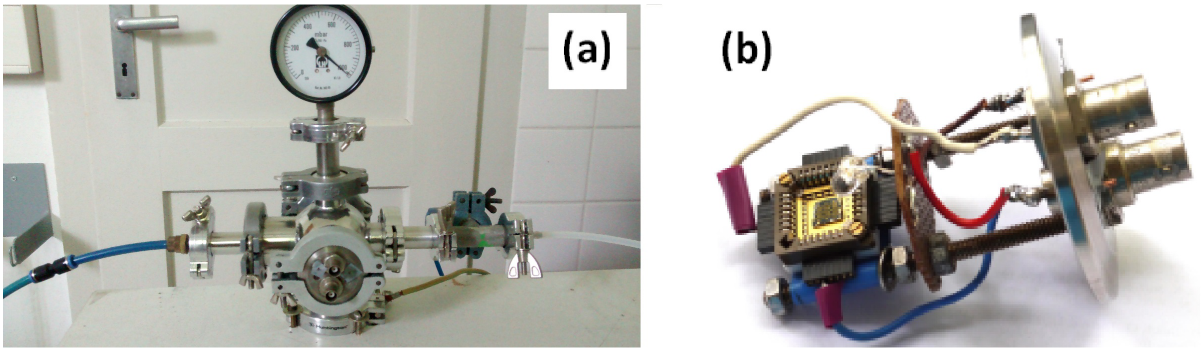

Figure 3.3: *Sealed chamber used for electrical measurements under different atmospheres (a). The commercial chip holding the samples were fixed on a home made carrier holder and externally connected to the SMU through a blind flange, equipped with BNC connectors (b).*

The sealed chamber environment (Figure 3.3 (a)) allowed to measure under various atmospheres and was therefore used for gas sensing measurements and the investigation of the photoconductivity properties in different environments. The commercial chip holding the samples was fixed on a home made carrier holder, equipped on every side with multipin feedthroughs (Figure 3.3 (b)). BNC connectors located on the external side of a blind flange allowed the electrical connection to the SMU. The chamber had a volume of approximately 3 l and could be evacuated up to 10^{-5} mbar. The flow of several gases was controlled by distinct and independent mass flow controller units from the company MKS [203].

The probe station was equipped with four manipulators holding conductive needles, which were used to contact the electrodes of the sample. Due to the flexibility of the contacting procedure, which do not require any electric bonding of the samples, the probe station was used for the measurements, which were carried out in air and are discussed in Chapter 4 and Chapter 6. The probe station was kept completely closed while measuring with a grounded metallic cage, in order to ensure electromagnetic shield.

3.3.2 Photoconductivity measurements

Photoconducivity measurement under below band gap excitation were conducted using a Xenon Lamp with 200 mm monochromator as a light source. The power density of the light excitation in the range 400 - 800 nm was around 40 $\mu W/cm^2$ in the blue, red and infra-red regions with a peak value of 80 $\mu W/cm^2$ in the green region.

A UV LED provided by the company Pure Led Technik was instead used as light source for the above band gap photoconductivity measurements. The LED had an emission angle

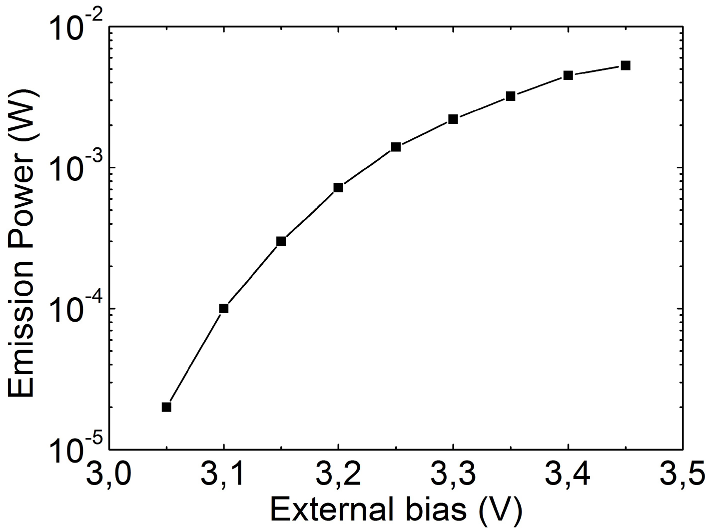

FIGURE 3.4: *Emission power of the UV LED, which was used as a light source for the above band gap photoconductivity measurements. The power could be adjusted from 20 μW up to 5 mW by varying the external bias.*

of approximately 15 °, central emission at 370 nm and FWHM of 10 nm. As shown in Figure 3.4, the emission power could be adjusted from 20 μW up to 5 mW by progressively varying the external bias from 3.05 V up to 3.45 V. The diode was placed 1 cm above the sample holder, in order to emit on a surface area of around 1 cm^2 in correspondence to the sample position. When not explicitly specified, the photoexcitation was carried out with the UV LED at an intensity of I = 1 mW/cm^2.

Prior every measurement the samples were kept in the dark for at least 24 hours, either in the sealed chamber or in the probe station, in order to reach a constant value of the current. For the measurements conducted in the sealed chamber under inert atmospheres, the gas (argon or nitrogen) was let into the chamber starting 2 hours prior beginning the measurement, at flow of 100 sccm and pressure of 1 atm.

3.3.3 Sensing measurements

Hydrogen sensing measurements were conducted using nitrogen flowing at 1000 sccm as a reference atmosphere. Molecular hydrogen was provided for safety reason from a formier gas (FG) supply, consisting of a mixture of hydrogen and nitrogen in molar concentration ratio of 5/95.

The gas sensitivity, denoted as S_{H_2}, was calculated as the relative change of the nanowire resistance upon hydrogen flow respect to the reference resistance R_0:

$$S_{H_2} = \frac{\Delta R}{R_0}. \tag{3.1}$$

The concentration of hydrogen in the reference atmosphere can be defined as:

$$[H_2] = \frac{n_{H_2}}{n_{tot,N_2}}, \tag{3.2}$$

where $n_{tot,N_2} = n_{ref,N_2} + n_{FG,N_2}$ is the total number of nitrogen moles in the measuring chamber, which includes the number of moles provided by the reference nitrogen flow (n_{ref,N_2}) and by the flow of formier gas (n_{FG,N_2}). Thus, equation 3.2 can be rewritten as:

$$[H_2] = \frac{1}{\frac{n_{ref,N_2}}{n_{H_2}} + \frac{n_{FG,N_2}}{n_{H_2}}}. \tag{3.3}$$

Considering that $n_{H_2} = 0.05 n_{FG}$, $\frac{n_{FG,N_2}}{n_{H_2}} = 0.95$ and since at constant pressure the molar ratio corresponds to the flow ratio, equation 3.3 can be finally expressed in terms of the reference flow Fl_{ref,N_2} and the flow of formier gas Fl_{FG}:

$$[H_2] = \frac{Fl_{FG}}{20 Fl_{ref,N_2} + 0.95 Fl_{FG}}. \tag{3.4}$$

As for the photoconductivity measurements, also prior sensing measurements the samples were kept in the dark for at least 24 hours, in order to reach a constant value of the dark current.

3.4 Photoluminescence

Photoluminescence spectroscopy represents a powerful tool for the investigation of energy levels in semicondutors, such as for instance impurities and intrinsic defect levels. Depending on the size of the incident spot, the photoluminescence can be classified either as macro or microphotoluminescence (μPL). In the latter case, the spot has typically a size of few μm^2. As such, μPL is a suitable tool for the optical characterization of single and/or contacted nanowires. Optical properties can be for instance investigated as a function of the position between the electrodes, revealing useful information about the distribution of defects along the nanowire.

In the frame of this thesis μPL measurements were performed on contacted ZnO nanowires, using a continuous wave HeCd laser and a nanosecond pulsed Nd:YAG laser as light sources. The laser beam was focused by a microscope objective to a spot ranging between approximately 1 μm^2 and 25 μm^2, largely depending on the chosen exciting wavelength. The emitted light was dispersed by a monochromator and detected by a CCD camera. The measurements presented in Chapter 4 were carried out at room temperature, while those presented in Chapter 6 were performed at low temperature (4 K). Further details concerning the PL setup can be found in [204].

3.5 Ion beam implantation

Implantations of argon and aluminium on contacted ZnO nanowires were carried out with an air insulated Cockroft-Walton accelerator from High Voltage Engineering Europa [205], which allows the implantation of almost every element with ion energies from 10 keV up to 400 keV and current densities up to tens of μA$\cdot cm^{-2}$. Positively charged ions are extracted from the ion source by a 30 keV DC voltage difference, focused by electrostatic lenses and mass separated by a 90° bending magnet. After mass separation, the ion beam can be further accelerated before entering the targed chamber, which is kept at the ground level. The implantation process was conducted at room temperature under high vacuum ($<5 \cdot 10^{-6}$ mbar), in order to ensure appropriate operation conditions.

The distribution of the implanted impurities and the generated defects was simulated prior the implantation by means of the software package SRIM [206, 207], which is a Monte Carlo code based on the simulation of binary collisions between the impinging ions and the target atoms. The dynamics of the impinging ions in the crystal is governed by a screened interaction potential, which determines their path until they completely stop. The software performs a statistical average between collisions and determine as a result a distribution of the implanted impurities and the induced defects. Additionally, post implantation annealing procedure was optimized in order to reduce the concentration of defects and to maximize the sample conductivity. The details concerning implantation and annealing parameters will be discussed in Chapter 6.

Chapter 4

Sub-bandgap photoconductivity in ZnO nanowires

This chapter deals with the below band gap photoconductivity properties of ZnO nanowire based field effect transistors. The initial investigation of the electrical properties of the samples in dark condition is followed by the analysis of the photoresponse properties in the range 400 - 800 nm. Particular attention is dedicated to the modulation of the photoresponse, induced by the applied gate voltage. The electrical measurements are accompagnied by a microphotoluminescence characterization, in order to gain deeper insight about the nature of the defect involved in the photoconduction process. The latter measurements were performed in collaboration with Rober Röder and part of the results have been published in [208].

4.1 Motivation

It is well known that the presence of defect levels in a field effect transistors can drastically affect several properties of such devices [209]. Defects can be located in the semiconductor channel as well as in the gate dielectric and in the sustrates, or at different interfaces. In particular, the impact on the transport properties can be particularly significant in nanowire based FETs, due to the high surface to volume ratio of the semiconductor channel.

In view of photodetection applications with ZnO nanowires, a detailed knowledge about the nature of defect levels in related electronic devices is fundamental. On the one hand, the presence of defect can be deleterious, leading for instance to device instabilities and degradation. Moreover, it can be deleterious in applications for which visible-blind ZnO photodetectors are required. On the other hand, it may be convenient whenever the extension of the photosensitivity range in sub-bandgap spectral range is desirable.

From this perspective, the FET configuration is particularly convenient, since it offers the opportunity to control the occupation of defect levels by means of electric gating. In this way, it is possible to selectively detemine wheter a defect level is available or not for the photoconduction process, allowing the development of flexible photodetectors, which can operate as a visible-blind or as sub-bandgap sensitive devices depending on the specific applied gate voltage.

4.2 Electrical properties of ZnO NW FETs in dark

4.2.1 Contact properties

As introduced in section 2.3, the dependence of the drain-source current on the corresponding voltage difference reveals fundamental informations about the contact properties of the device. Current – Voltage measurements (I-V) were performed in the range [-10 V;+10 V] on samples produced as described in 3.2, keeping the gate electrode grounded. The curves related to single nanowire devices are typically characterized by a strongly non linear profile, which indicates the formation of Schottky contacts. However, the Schottky properties of the two contacted nanowire sides are not necessarely comparable, since the mechanical imprinting of the nanowires on the substrate prior the photo-lithography is a random process. Consequently, the I-V characteristics of a single nanowire device can assume either a symmetrical or an asymmetrical profile, as evident in Figure 4.1 (a) and Figure 4.1 (b) for two different devices. However, when the electrodes are bridged by a higher number of nanowires, the I-V charateristics appear more linear, as a result of the average between several non linear I - V curves (Figure 4.1 (c)).

The appearence of the S-shaped profile in the I-V characteristics of single nanowire devices can be understood by modelling the contacted ZnO nanowire, which is basically a metal-semiconductor-metal structure, as two back-to-back Schottky diodes. This choice is motivated by the fact that the I-V characteristics of a diode are characterized exactly the same rectifying properties of a Schottky contact. Basically, when an external voltage difference is applied, the same current I must flow through both diodes. However, when one diode (nominated for semplicity diode 1) is forward biased, the other one (diode 2) is reversed biased. The latter tends consequently to limit the value of the current, which tends to saturate. The same situation occurs obviously in the opposite interval of the voltage difference. This explains qualitatively the observed behaviour. Quantitatively, the current which would flow through a single diode can be written as:

$$I_{1,2} = A^{*}T^{2}e^{-\frac{\phi_{1,2}}{kT}}(e^{\frac{eV}{kT}} - 1) \tag{4.1}$$

where $\phi_{1,2}$ are the respective potential barrier at the two interfaces. Imposing that $I = I_1 = I_2$, the total current can be expressed as [210]:

$$I = \frac{I_{01}I_{02}sinh(eV/2kT)}{I_{01}exp(eV/2kT) + I_{02}exp(-eV/2kT)}, \tag{4.2}$$

where $I_{01} = AT^{2}exp(\phi_1/kT)$, $I_{01} = AT^{2}exp(\phi_2/kT)$ and $\phi_{1,2}$ are the Schottky barrier heights. The other quantities are definited as previously. An example of fitting using equation 4.2 is presented in Figure 4.1 (a), in case of two comparable barriers heights. The discrepancy observed at low bias originates most probably from the non complete idealy of the diodes [210], which is not taken into account in equation 4.2. The obtained values of the two Schottky barrier ϕ_1 and ϕ_2, which are around 0.45 eV, are comparable to that reported in literature for similar ZnO nanowire devices [211].

However, the nature of the Au/Ti/ZnO junction is still matter of debate in literature. While some studies report about the formation of a Schotthy barrier [212], some others reveal ohmic properties [32, 213]. In general, a univocal determination of the nature of such junction is not possible, due to the similarity of the work function of Ti and the electron affinity of ZnO. In particular, the reported values of the ZnO electron affinity range from 3.7 up to 4.5 eV [214, 215]. As such, depending on the specific conditions, it can be higher or lower than the work function of Ti (4.33 eV [216]) and the corresponding junction might show respectively ohmic or Schottky characteristics. Additionally, depending on the Ti thickness, the presence of Au ($\phi = 5.1$ eV [216]) in the proximity of the Ti/ZnO interface can lead to a further mixing of the junction properties. Furthermore, even while dealing with the same nominal semiconductor, several factors such as growth conditions and sample preparation can lead to incomparable results in terms of junction properties. In particular, different growth techniques and growth conditions give typically rise to different concentration of unintentional dopants and determine therefore dissimilar contact characteristics. Also the roughness of the semiconductor surface critically depends on the processing steps required for the sample preparation and can drastically affect the features of the interface.

A final comment concerns the influence of the source-drain bias polarity on the density of occupied defect levels in the proximity of the contact regions. In general, the occupation

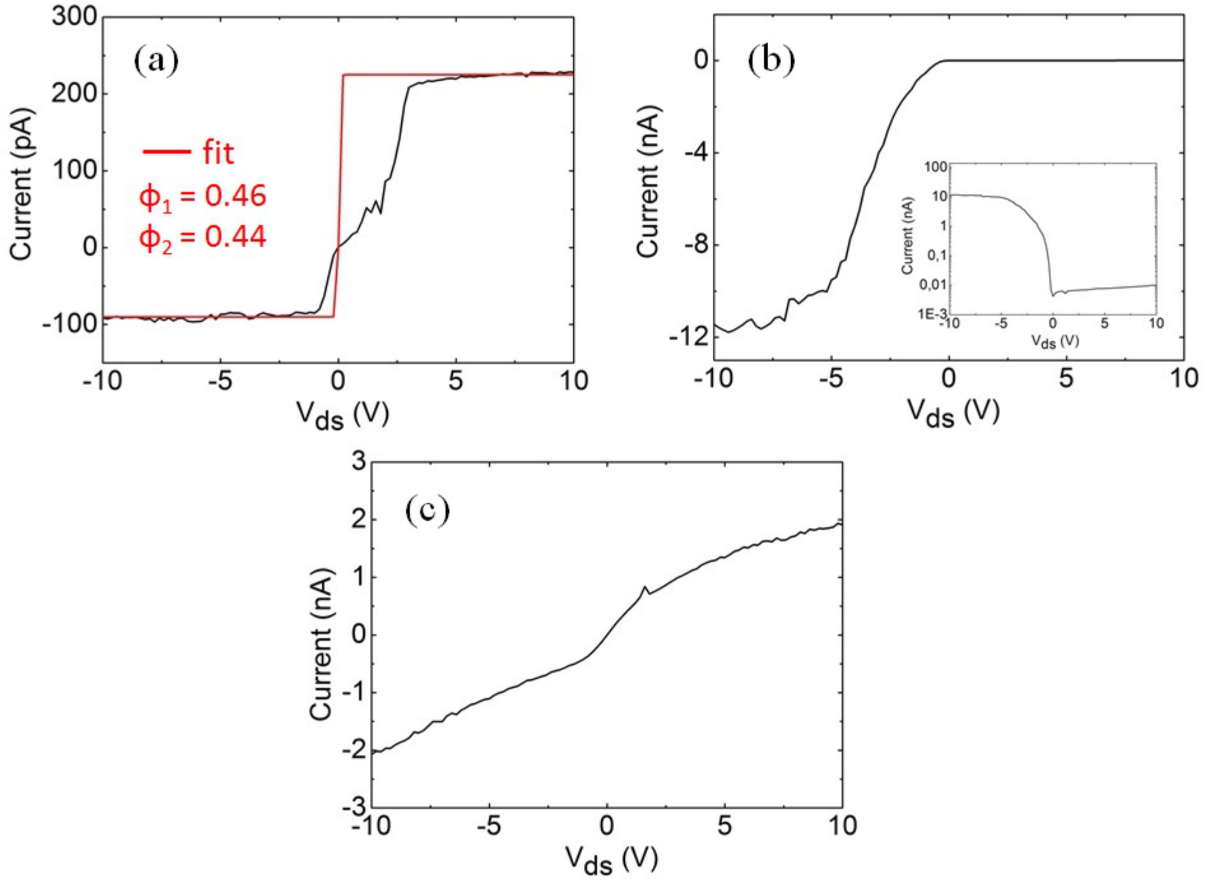

Figure 4.1: *Current - Voltage measurements (I - V) performed on ZnO nanowire devices (compare figure 3.2) with different contact properties. Single nanowire devices show typically nonlinear characteristics due to the formation of a Schottky contact between ZnO and the Ti/Au electrodes. The height of the Schottky barriers on the two contacted sides of the nanwire can be comparable (a), or considerably differs (b), resulting in a symmetric or asymmetric profile of the I- V characteristics, respectively. When the electrodes are bridged by more nanowires the curve is almost linear (c), being the average between several asymmetric contributions.*

probability of a defect level varies in the depletion region, since its position changes in respect to the Fermi level [217]. Since the application of an external bias modifies the original width of the contact depletion region and the profile of the corresponding band bending, the occupation probability of defect levels near the contact region will change correspondingly. In case of contacted nanowires with symmetric I-V characteristics, no matter whether linear or not, it is expected that an inversion of the bias polarity does not affect significantly the total density of occupied defect levels, since the drain and the source contacts are characterized by comparable properties, as previously discussed. However, this is not true when the I-V characteristics are highly asymmetric. In this case the properties of the source and drain contacts significantly differ and the density of

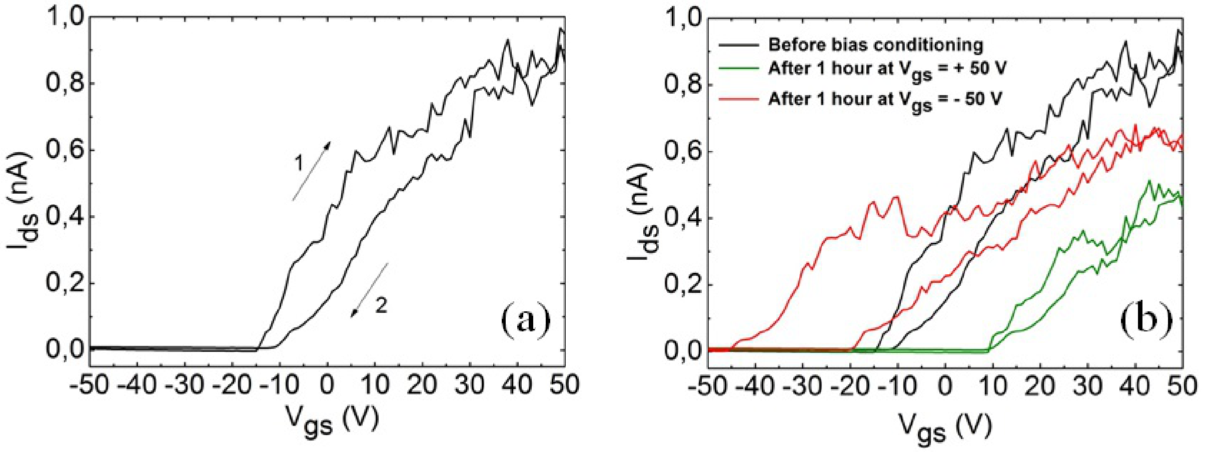

FIGURE 4.2: *Transfer characteristics (I_{ds}–V_{gs}) of a single ZnO NWFET, measured at V_{ds} = + 5 V in air and dark conditions (a). A large hysteresis is appreciable, which appears when the voltage is sweept at first from negative toward positive values (1) and then backwards (2). The effect of a bias conditioning on the transfer measurements is shown in (b). Conditioning at V_{gs} = - 50 V for 1 hour prior the measurement induces a negative shift in the gate voltage threshold, whiel the occposite occurs after a conditioning at V_{gs} = + 50 V. In the former case also a larger hysteresis can be appreciated.*

occupied level at a specific bias may be correspondingly uncomparable with that occurring under opposite bias polarity. This fact must be always taken into account, while dealing with the transport properties of such nanowire devices.

4.2.2 Transfer characteristics

Since the conductivity of n- and p-type semiconductors shows an opposite dependence on an external gate potential, transfer characteristic measurements (I_{ds} - V_{gs}) represent a suitable tool, in order to determine the nature of charge carriers in the semiconductor channel. For this purpose, transfer characteristics were measured in air on single nanowire FETs in the gate voltage range [-50 V;+50 V]. A typical measurement, presented in Figure 4.2 (a), shows that the nanowire channel is fully depleted when the the gate voltage is lower than a threshold value, above which the conductivity progressively increases. This result conforms that the investigated ZnO nanowires nanowire are as expected intrinsically n-type doped, as also revealed by previous studies [22, 86, 94–96]. Additionally, a large hysteresis can be observed when the voltage is sweept at first from negative toward positive values and then in the opposite direction.

However, both the voltage threshold and the hysteresis cannot be univoquely determined, as they can be for instance affected by a gate bias conditioning, which consists in the

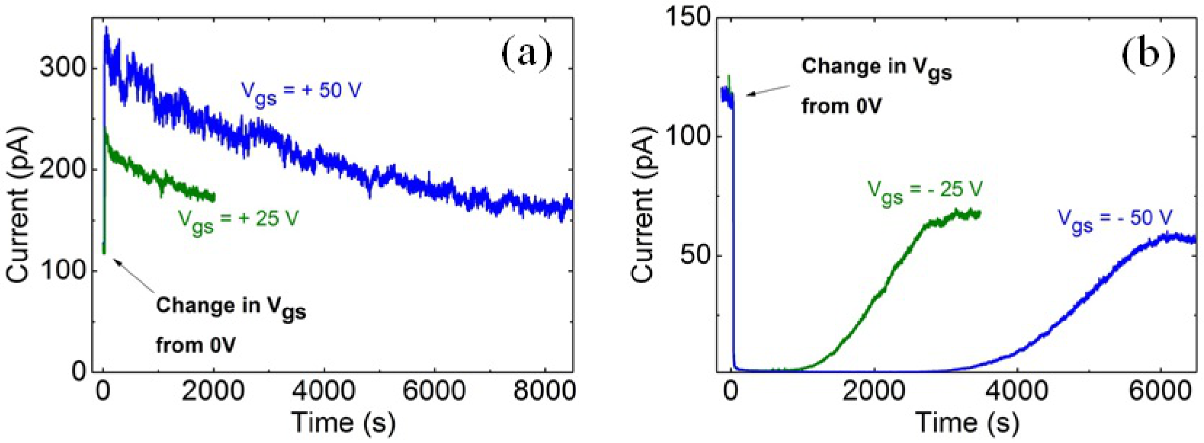

FIGURE 4.3: *Temporal dependence of I_{ds} in a single ZnO NW FET after changing V_{gs} from 0 V toward positive (a) or negative (b) voltage values. In the former case the current increases quickly, but then decreases gradually. The opposite occurs in the latter case.*

application of a constant V_{gs} for an extended time prior measuring the transfer characteristics. As shown in Figure 4.2 (b), a positive bias conditioning induces a positive shift of the threshold voltage and a reduced hysteresis, while the opposite occurs after a negative bias conditioning. The conditioning was performed in the former and latter case by keeping the voltage respectively at V_{gs} = + 50 V and V_{gs} = - 50 V for one hour prior the measurement. This indicates that the current I_{ds} is not exclusively determined by the gate voltage value but is also affectect by the previous gating history. Moreover, instability of the drain-source current was observed in the investigated samples by measuring I_{ds} as a function of the time during a prolonged gating. Specifically, the change in I_{ds} induced by a sudden variation of V_{gs} tends to partially dissipate over the time, as shown in Figure 4.3 in case of positive and negative gating variations. I_{ds} was also measured four times consecutively as a function of the time, three times in air and once in argon, changing V_{gs} from 0 V to - 50 V. At the end of every measurement V_{gs} was switched again to 0 V and left for 10 min at this value of the gate voltage before starting the following measurement. A progressive decrease of the current saturation is observed from the first to the last measurement, but this trend is not significantly affected by the atmosphere conditions, as shown in figure 4.4.

Gating instabilities effects and the appearence of transfer hysteresis have been already observed in ZnO based transistors and mainly attributed to the charging and discharging of interface trap levels [218, 219] or to polarization effects induced by adsorpbed molecules [86, 139]. Since no dependence on the surrounding atmopshere has been observed, the

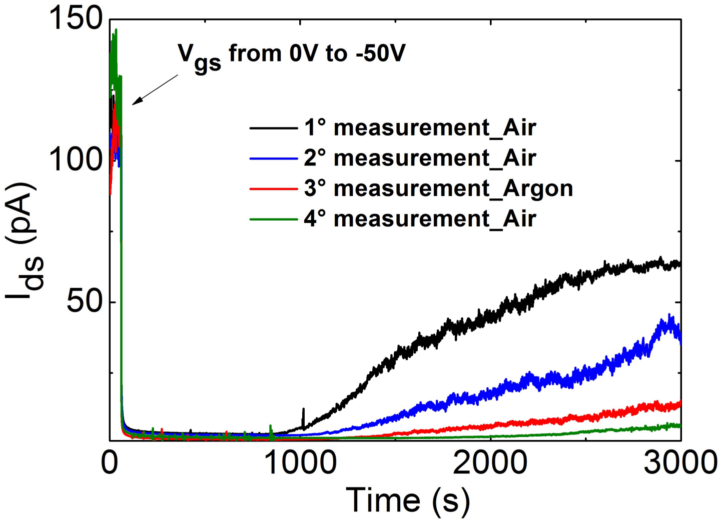

FIGURE 4.4: *Repetition of the same measurement presented in Figure 4.3 in case of* V_{gs} *= -50 V for four times consecutively, three times in air and once in argon. A progressive decrease of the saturation current is observed, not related to the atmosphere conditions.*

former process seems to be predominant in the sample investigated within this work. The corresponding mechanism is based on the electrostatically induced attraction or repulsion experienced by electrons respectively toward or from interface levels, located between the substrate and the SiO_2 layer or between the SiO_2 and the ZnO. Depending on the sign of the gate potential, this results in the progressive formation of positively or negatively charged interface layers, which partially screen the gate field and lead the appearence of the above presented effects. Furthermore, the gating-driven accumulation or depletion of electrons in the proximity of the source and drain contact regions may also determine the occurrence of charging/discharging processes at defect levels, which eventually lead to a local change of the contact Schottky barrier, with corresponding slow variation of I_{ds} [220].

Such instabilities are not necesserely deleterious for the performance of FETs, as they can be for instance positively exploited for the development of non-volatile memories [221, 222]. As such, attempts have been made, in order to achieve a reliable control of the hysteresis. These includes for instance the use of gate dielectrics with superior trapping ability, such as Al_2O_3 [223], or procedures for the generation in the substrate of mobile charges, which can be easily trapped and detrapped from interface states. For the latter purpose, annealing treatments in hydrogen atmospehres [218] and hydrogen implantation [198] have been succesfully exploited. Furthermore, controlling the population of interfacial levels by means of electric gating can be employed in order to modulate the photoconductiviy of nanowire-based FETs under sub-bandgap excitation.

4.3 Gate voltage modulation of photoresponse

The below band gap photoconductivity of ZnO NW FETs was investigated considering single nanowire devices with strongly asymmetric I-V characterisitcs, such as in Figure 4.1 (a), in order to simultaneously evaluate the influence of the gate voltage and that of the source-drain bias on the optical activity of defect levels.

The photoresponse was at first studied under negative gating (V_{gs} = - 50 V) in the range from 400 to 800 nm, in steps of 40 nm. The measurements, shown in Figure 4.5 (a), were conducted initially at V_{ds} = + 5 V, switching V_{gs} from 0 V to - 50 V immediately before starting the data acquisition at t = 0 s. The light excitation was then switched on at t = 5 s. At the end of every measurement V_{gs} was switched back from -50 V to 0 V and left at this gate voltage value for 1 min before starting the following measurement with a different exciting wavelength. Additionally, a reference measurement in the dark was performed under the same experimental conditions.

No increase of I_{ds} was observed in the investigated temporal interval (200 s) with exciting wavelength longer than 640 nm. Only with shorter wavelength an onset of the photocurrent increase appears, untill the current saturates in all investigated cases sligthly below 100 pA. The onset is not immediate and the activation time required to observe it decreases progressively with shorter wavelength. The photoconductivity response was then investigated at gate voltage V_{gs} = 0 V and V_{gs} = + 50 V under illumination at 550 nm. For the measurement at V_{gs} = + 50 V, the same procedure considered for the previous measurements at V_{gs} = - 50 V was adopted. In both cases, no photoresponse was observed, as can be seen in Figure 4.5 (b).

The measurement performed at V_{gs} = - 50 V under illumination at 550 nm was also compared on a larger time scale with that carried out in dark conditions, in order to compare the rise of the photocurrent with the slow gating-induced instablilites in I_{ds} described in the previous section. As shown in Figure 4.6, the photocurrent and the dark current saturate at comparable values. However, the onset of the current increase and the time required to reach the saturation are much reduced under light excitation. This indicates that the charge trapping/detrapping processes occurring at interfacial states or near the contacts, which are responsible for the slow increase of the dark current

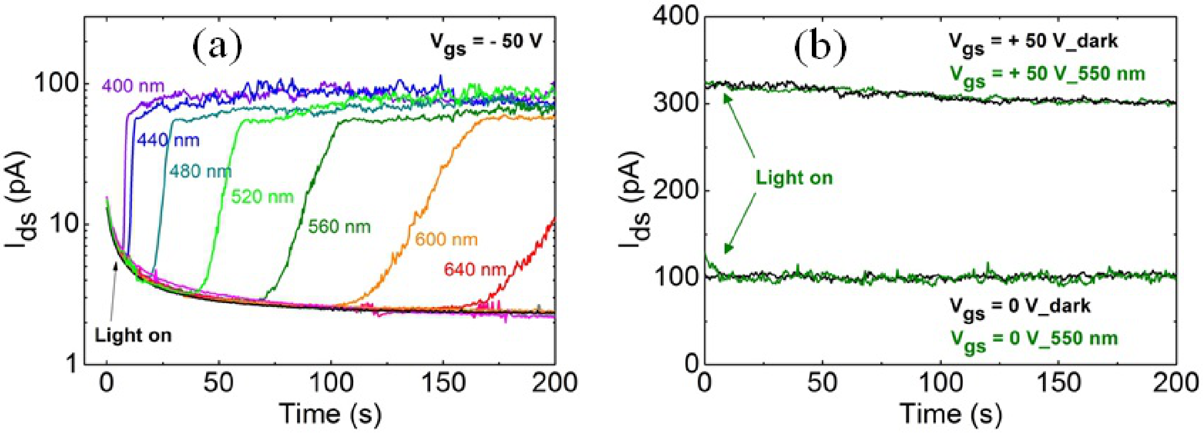

FIGURE 4.5: *I_{ds} as a function of the time in a single ZnO NW FET under below-band-gap excitation in the range 400-800 nm, in steps of 40 nm, at V_{gs} = -50 V (a). In all measurements the photocurrent saturates at similar values. The device does not show any response under photo-excitation at wavelength longer than 640 nm. An equivalent measurement is repeated at V_{gs} = 0 V and V_{gs} = +50 V under photoexcitation at 550 nm (b). In both cases no photoresponse is observed.*

at negative gate voltages, must be effectively involved also under photoexcitation below band gap.

Analogous measurements under photoexcitation at 450 nm and 550 nm were performed also at reversed source-drain bias (V_{ds} = - 5 V). In view of what pointed out in the conclusions of the previous section, a significant difference in terms of photoresponse is to expect, if the defect levels in the proximity of the contact regions play a major role in the photoconduction process. However, as shown in Figure 4.7, the obtained results are comparable with that reported in case of V_{ds} = - 5 V, since photocurrent is measured only at V_{gs} = - 50 V, but not under positive gating. This indicates that the eventual charge/discahrge processes occurring in the proximity of the source and the drain contacts are substantially not responsible for the appearence of the sub-bandgap photoresponse under negative gating.

The eventual contribution of other defect levels, located in the core of the nanowire, was investigated by means of microphotoluminescence measurements. Such measurements were performed at room temperature in the regime of low excitation density, in order to maximize the deep level emission (DLE) intensity and to avoid defect saturation effects [204]. At room temperature, the diffusion length of the exciton in ZnO is in the range of the NW diameter [224] and it is therefore more likely that the excitons are captured at defects, rather than reaching the surface or the SiO_2/ZnO interface. Consequently, the contribution to the photoluminescence signal from the defects located in the core of the

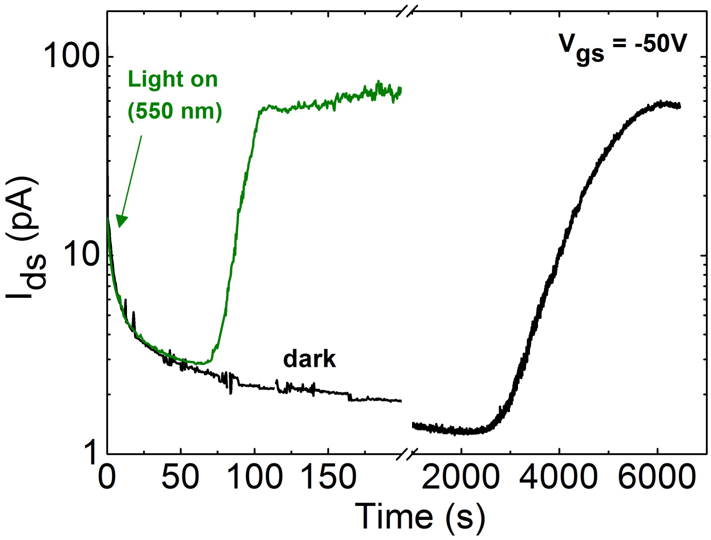

FIGURE 4.6: *Direct comparison of I_{ds} as a function of time under sub-bandgap excitation at 550 nm and in dark conditions at V_{gs} = -50 V. The current saturates in both cases at similar values. However, the temporal onset of the current increase is much reduced under photoexcitation.*

nanowire is expected to be dominant compared to the emission originating from surface or interface levels.

The sample was connected to the same electrical generators, in order to reproduce the same experimental conditions as for the electrical measurements and the spectra, shown in Figure 4.8, were measured at gate voltage $V_{gs} = 0$ V, immediately after switching to V_{gs} = -50 V and after 1 and 2 minutes of prolonged gating at V_{gs} = -50 V. It can be clearly observed that in all investigated cases the change in the gate voltage does not induce any appreciable change of the DLE, which is typically related to defect levels located in the band-gap of ZnO [204]. Therefore, the result of the μPL measurements strongly suggest that the change in the gate voltage does not induce any appreciable variation in the population of defect levels located in the nanowire volume.

This result corroborates the original hypothesis that the switching of the gate voltage toward negative values induces substantially only a variation of the interfacial level occupation. Furthermore, the observation of photoresponse at V_{gs} = - 50 V but not at V_{gs} = 0 V and V_{gs} = + 50 V, implies that only a negligible density of interfacial levels are occupied under positive gating. On the contrary, other authors have instead observed enhancement of the below band gap photoconductivity under positive gating, as a result of photoexcitation of occupied interfacial levels [225, 226]. In principle, a positive gating

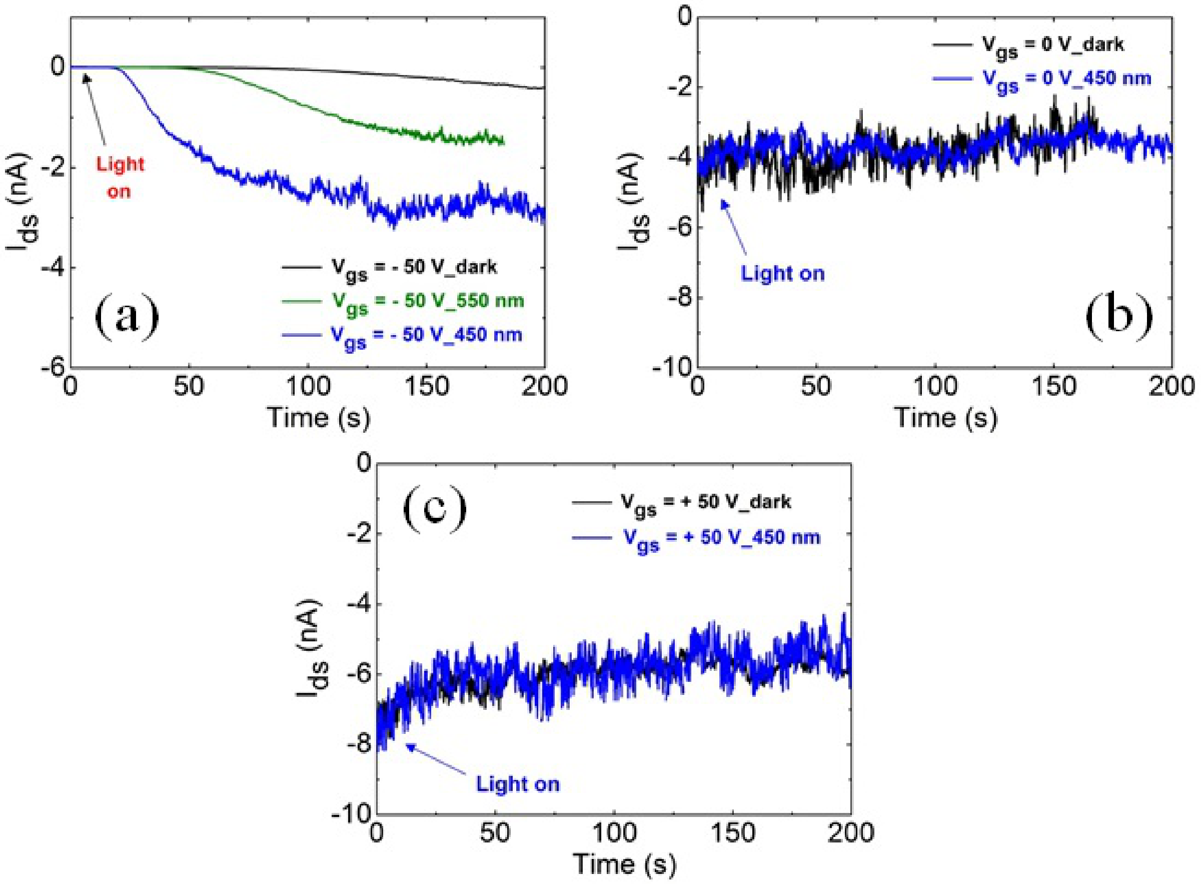

FIGURE 4.7: *I_{ds} as a function of the time in a single ZnO NW FET under photoexcitation at 450 nm and 550 nm and reversed polarity of the drain-source bias (V_{ds} = -5 V). Measurements were performed at V_{gs} = - 50 V (a), V_{gs} = 0 V (b) and V_{gs} = + 50 V (c). As already observed in the measurements performed at V_{ds} = +5 V, photoresponse occurs only under negative gating.*

should induce electron accumulation in ZnO close to the interface with the SiO_2 [225], favoring consequently the filling up of such levels. However, whether this process effectively occurs depends on the effective gate voltage experienced by the semiconductor channel in the proximity of the interface, which critically depends on the screening determined by the gate dielectrics. Since the oxide layer of the FETs produced in the frame of this thesis was at least 4 times thicker than that employed in [225, 226], a stronger screening of the gate field is expected in the proximity of the SiO_2/ZnO. This might consequently hinder the electron trapping from the ZnO toward interface.

The trapping process must therefore proceed in the opposite direction, involving electrons which are already available in the oxide layer. It is well known that electrons can be localized in the gate dielectrics at bulk defect states [209] and at the interface with the substate [227–229]. Under a negative gating these can be repelled toward the interface

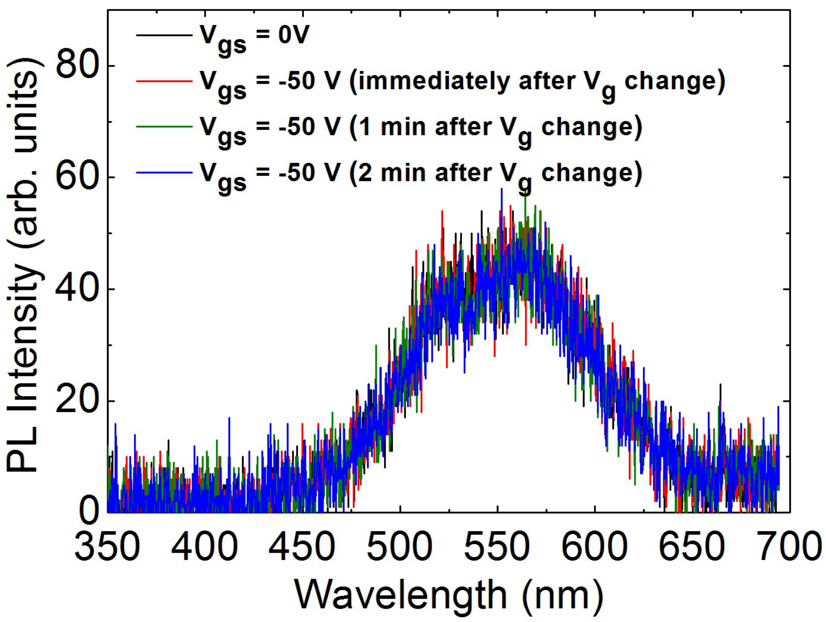

FIGURE 4.8: *μPL spectra of a single ZnO NW FET in the spectral region of the deep-level-emission, at V_{gs} = 0 V and V_{gs} = -50 V. The change of the gate voltage does not induce any appreciable change in the defect-related emission, which is dominating the spectra.*

with the nanowire and there being trapped, as illustrated in Figure 4.9. Since such electron migration is expected to be a slow process, an activation time is most propably required in order to fill the interfacial levels. This might explain the non immediate onset of the photoresponse observed during the photoconductivity measurements.

Despite the uncertain origin of the migration mechanisms in the gate dielectric and the interfacial levels involved in the photoconduction process, the observed results clearly indicate the possibility to succesfully modulate the below band gap photoresponse of ZnO NW FETs by means of electric gating. The intentional generation of further defects at the interface SiO_2/ZnO interface, succesfully reported for instance in case of proton irradiation [230], can be in principle exploited for enhancing and tuning the photoresponse properties of similar nanowire based devices.

On the other hand, the measurements performed reveals that the density of defects in the core of the nanowire is too low, in order to contribute to the photoresponse. Further strategies, including for instance modification of the nanowires by means of ion beam implantation, should be therefore explored, in order to selectively increase the density of optically active defects in the semiconductor channel. A stronger involvment of the nanowire channel in the photoresponse mechanism would be highly beneficial for the

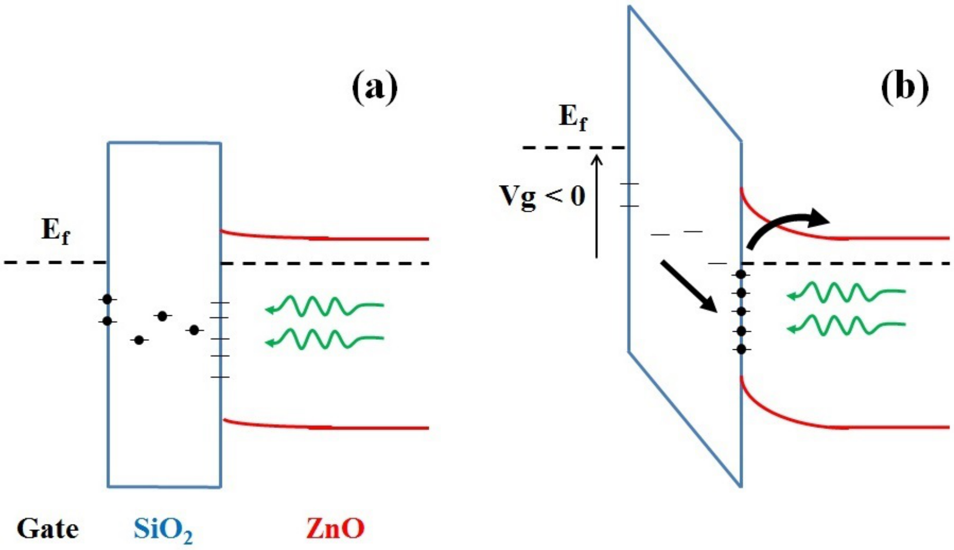

FIGURE 4.9: *Schematic model describing the influence of the electric gating on the sub-bandgap photoresponse properties of a single ZnO NW FET. At* $V_{gs} = 0$ *V interfacial levels between the* SiO_2 *and the ZnO are not occupied and photorsponse is consequently not observed (a). Under negative gating migration of electrons from eventual subtrate/dielectric or dielectric defect states may occurs, leading to the charging of* SiO_2*/ZnO interfacial states and the correpondingly to the observed photoconductivity.*

development of faster sub-bandgap photodetectors, since the gating-induced emptying and occupation of defect levels in ZnO is expected to proceed faster than in SiO_2. As a result, a significant reduction of the temporal onset required to observe the photoresponse is to expect.

4.4 Conclusions

In this chapter the sub-bandgap photoconductivity properties of ZnO nanowire field-effect-transistors (NW FETs) have been investigated. The FET configuration is exploited, because it offers the possibility to control the occupation of defect levels by means of electric gating. Consequently, the photoresponse of such devices can be tuned according to the desired photodetection applications, allowing the development of flexible photodetectors based on ZnO nanowires.

At first, the electrical properties of the NW FETs in dark conditions have been presented and discussed. Current - voltage measurements ($I_{ds} - V_{ds}$) reveal the Schottky nature of the source and drain contacts. Transfer characteristics ($I_{ds} - V_{gs}$) confirm that the ZnO nanowire channel behaves as expected as an n-type semicondutor, showing electron depletion or accumulation under respectively negative or positive gating. However, significant gating instability effects have been observed, including the slow dissipation of the current change induced by a sudden variation of the gate voltage or the influence of a gate bias conditioning on both gate voltage threshold and transfer hysteresis. Such effects have been attributed to the charging/discharging of defect states located at the interface SiO_2/ZnO.

Sub-bandgap photoresponse has been observed in the range 400 - 800 nm under negative gating (V_{gs} = - 50 V), while no reaction occured at positive gate voltage. The photocurrent tends to saturates approximately at the same value independently on the exciting wavelength. However, the onset of the photresponse requires an activation time, which progressively decreases as the exciting wavelength decreases. The obtained results are substantially independent on the drain-source bias polarity.

Photoluminescnece measurement reveal additionally that changes in the gate voltage do not induce any appreciable variation in the population of defect levels located in the nanowire volume. This indicates that the same interfacial levels, which are responsible for the gate instabilites in the dark current, are involved also in the photoconduction process.

Chapter 5

Persistent photoconductivity in ZnO nanowires

This chapter deals with the persistent photoconductivity observed in ZnO nanowires after above band gap excitation. The study is focused in particular on the influence of different surrounding environments on the photoconduction process, as well as on the dependence of the photocurrent decay on the light excitation power. A fitting procedure based on the kinetics of the oxygen adsorption process is then discussed. Part of the results presented in this chapter have been published in [39].

5.1 Atmosphere dependence of the persistent photoconductivity

If the persistence of the photoconductivity is related to the properties of the nanowire surface, a dependence of the photo-current decay on the surrounding environment must be expected. Photoconductivity measurements in different atmospheres were therefore performed, in particular in air, under flow of inert gases (nitrogen and argon) and at low pressure (10^{-5} mbar). For this purpose, several single nanowire devices were selected and their electrical properties investigated.

The I-V characteristics of a typical sample are shown in Figure 5.1 as a function of different environments and UV excitation. In dark, the value of the current in nitrogen, argon and air is substantially comparable in the investigated voltage range, while it is around one order of magnitude lower in vacuum. Upon UV light excitation in steady

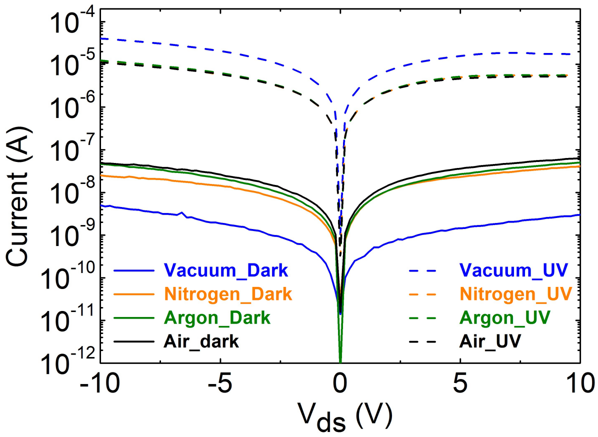

FIGURE 5.1: *Current-voltage (I-V) characteristics of a single ZnO NW device in different environments. The photosensitivity of the nanowires to UV excitation is clearly appreciable, with a particularly pronounced change under vacuum conditions.*

state conditions the conductivity is at least three orders of magnitude higher than in dark, with a particularly pronounced change under vacuum conditions.

The photocurrent as a function of time increases initially quickly under all atmosphere conditions (Figure 5.2 (a)), especially in air, as shown in Figure 5.2 (b). The increase rate slows down progressively and a saturation is reached within one hour in air, nitrogen and argon. The rate reduction is instead less pronounced in vacuum, in which the photocurrent increases approximately linearly with the logarithm of the time. The observed photoresponse can be quantitatively expressed in terms of photoresponsivity R, which is defined as the ratio between the steady state photocurrent and the excitation power absorbed by the nanowire $P_{abs,NW}$ [63]:

$$R = \frac{\Delta I}{P_{abs,NW}}. \tag{5.1}$$

$P_{abs,NW}$ can be calculated in terms of the nanowire lateral area (A_{NW}), light intensity (I_{exc}), reflectivity (R) and absorption coefficient (α) of ZnO at 370 nm, as $P_{abs,NW} = I_{exc}A_{NW}(1-R)(1-e^{-\alpha d})$, where d is the nanowire diamater. The lateral area of the nanowire can be approximated as $A_{NW} \approx d \cdot l$, with $d = 200$ nm and nanowire length l= 5 μm. Assuming $R = 0.1$ and $\alpha = 10^5\ cm^{-1}$ [231], $P_{abs,NW} \approx 10^{-11}$ W. The values of the photocurrent are $I_{ph} = 5 \cdot 10^{-6}$ A in air, argon and nitrogen and $I_{ph} = 1.5 \cdot 10^{-5}$ A in vacuum. Correspondingly, the responsivity in air, argon and nitrogen is estimated as:

$$R \approx 5 \cdot 10^5 \frac{A}{W}, \tag{5.2}$$

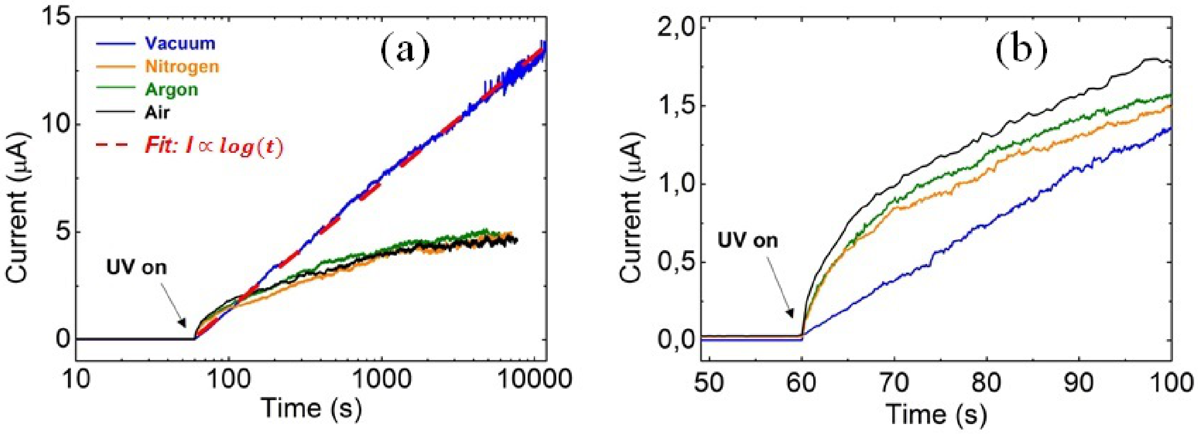

FIGURE 5.2: *Increase of the photocurrent in a single ZnO nanowire device as a function of the time in different environments (a). The current saturates within two hours in air, argon and nitrogen, but not in vacuum. In the latter case the photocurrent increases logarithmically with the time, as shown by the corresponding fitting function. (b) shows a magnification of (a), when the UV light is switched on. The photoresponse is initially stronger in air than in other atmospheres. The measurements were performed at* $V_{ds} = +5$ *V.*

while in vacuum:

$$R \approx 1.5 \cdot 10^6 \, \frac{A}{W}. \tag{5.3}$$

The obtained values are comparable with that observed by other authors in similar ZnO nanowire devices [232–235] and confirm the enormeous potentialities of ZnO nanowires as building blocks for photodetection applications.

After light excitation the photocurrent decays faster in air than in other environment conditions, as shown in Figure 5.3 (a). A significant drop of the conductivity is observed under vacuum conditions and in the inert atmospheres as soon as air is let into the chamber. However, a gradual slowdown of the decay rate occurs few seconds after letting in air, as particularly evident in Figure 5.3 (b).

The photocurrent was then measured as a function of the exciting wavelenth, in order to determine the nature of the charge carriers involved in the photoconduction process. For this purpose, the Xenon Lamp was used as a light source in the spectral range between 300 and 900 nm. The measurement was carried out in air, by scanning the spectral range in steps of 5 nm and keeping the light excitation on for 5 s during every step. As shown in Figure 5.4, a sharp onset of the photocurrent increase is observed around 375 nm, which corresponds to the band gap of ZnO. The decrease of the photocurrent above 350 nm is

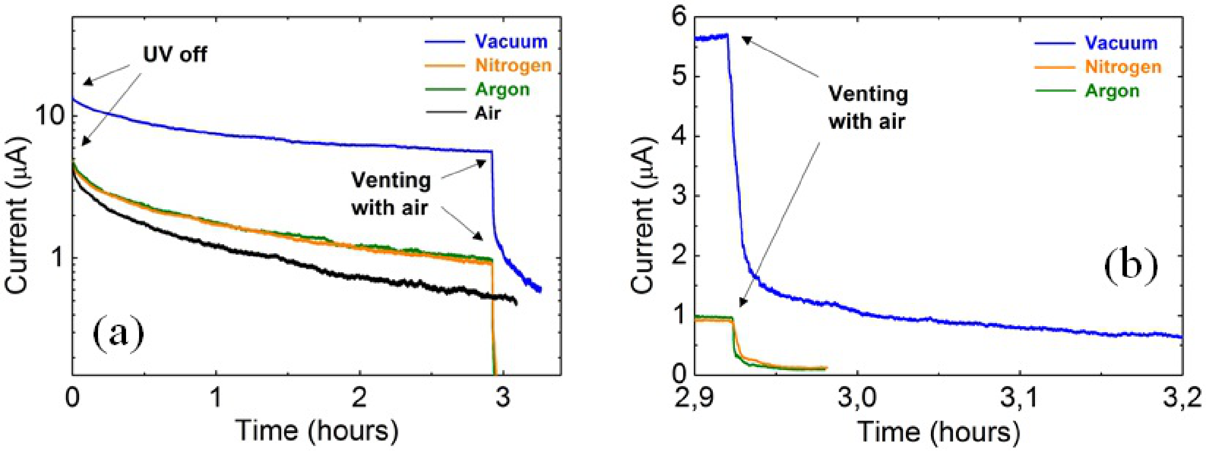

Figure 5.3: *Photocurrent decay in a single ZnO nanowire device in different environments after removing the UV excitation; (b) shows a magnification of (a), when air is let into the chamber. The decay rate increases considerably, but then progressively slows down. The measurements were performed at* $V_{ds} = +5$ *V.*

caused by the reduced light intensity in this spectral region of the used lamp. Since no photoresponse is observed at wavelength longer than 375 nm, the overall photoconduction process can be attributed to the generation of electron-hole pairs from the valence band to the conduction band, with negligible contribution from defect state levels.

However, the direct contribution of free electron-hole pairs to the photocurrent can be substantially neglected, as proved in the following by comparing the experimental photocurrent with that expected under the assumption that all photogenerated electron - hole pairs contribute to the photoconductivity. The latter assumption presupposes that all photogenerated charge carriers remain free during the photoconduction process, namely that their lifetime is not longer than 1 ns.

Under steady state excitation conditions, the density of free electron-holes pairs Δn_{ph} is related to their lifetime τ and to the carrier photogeneration rate G through the following expression [152]:

$$\Delta n_{ph} = \tau \cdot G. \tag{5.4}$$

The photogeneration rate can be expressed as $G = P_{abs,NW}/(E_g \cdot V_{NW})$, where E_g is the band gap of ZnO and $V_{NW} \approx 2 \cdot 10^{-13}\ cm^3$ is the nanowire volume. Thus:

$$G \approx 10^{20}\, s^{-1} \cdot cm^{-3}. \tag{5.5}$$

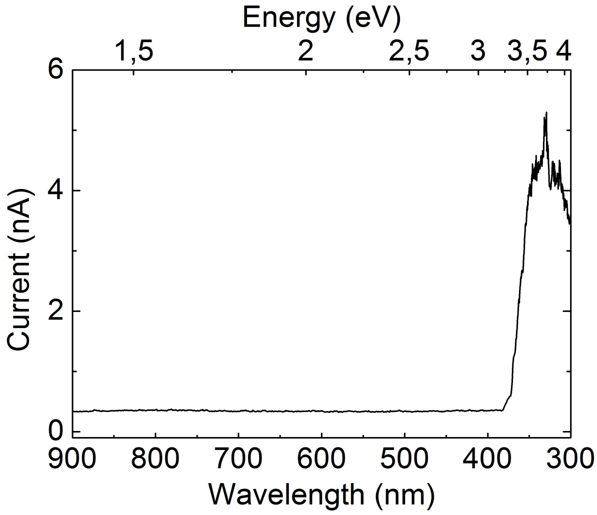

FIGURE 5.4: *Photoresponse of a single ZnO nanowire device as a function of the exciting wavelength. A clear onset is observed for wavelength shorter than 375 nm, which corresponds approximately to the band gap of ZnO. The measurement was performed in air at V_{ds} = +5 V.*

Considering $\tau \approx 1ns$, the density of free electrons-hole pairs is estimated to be $\Delta n_{ph} \approx 10^{11}\,cm^{-3}$. This corresponds to the photocurrent:

$$I_{ph} = S \cdot e \cdot \mu \cdot E \cdot \Delta n_{ph} \approx 1\,pA, \tag{5.6}$$

assuming a nanowire cross section $S = (d/2)^2\pi \approx 10^{-9}\ cm^2$, an electron mobility $\mu \approx 20\ cm \cdot V^{-1} \cdot s^{-1}$ [37] and an electric field between the electrodes $E = 5$ V/5 μm $= 10^4\ V/cm$. The calculated value of the photocurrent is clearly much lower than the experimental ones, which is in the order of few μA in all considered environments. The large discrepancy reveals therefore that the lifetime of the photogenerated charge carriers must be significantly longer than 1 ns. This reflects a reduction of the electron-hole recombination probability, which can be caused by the trapping of either electrons or holes, which leave free umpaired charge carriers with prolonged lifetime. Since previous Hall measurements revealed that the photoconductivity in ZnO is determined by photogenerated electrons [236], hole trapping mechanisms must be effective. Among these, hole trapping at surface states is most likely dominant, since the dynamics of the photocurrent increase depends on the environment conditions. In particular, the evidence that the photocurrent rises initially faster in air than in vacuum, indicates that oxygen adsorbed species promote such surface trapping process. These results are in accordance to that obtained by Melnick [164] and attributed to the migration of holes toward the surface, induced by the ionosorbed-oxygen related surface band bending (Figure 5.5 (a)).

Furthermore, the logaritmic dependence of the photocurrent increase over the time observed in vacuum suggests that the photocurrent increase is accompanied by a photodesortion process, since the photodesorption from semiconductor surfaces is typically characterized by a logaritmic kinetics [237]. This further supports the original intuition of Melnick, according to which ionosorbed oxygen is desorbed from the surface as a result of the recombination between trapped electrons and holes accumulated at the surface. The desorption process leaves consequently a certain fraction of umpaired photogenerated electrons in conduction band with the required prolonged lifetime. More quantitative considerations about this point will be discussed in section 5.2. The fact that such logaritmic dependence is clearly observed only in vacuum, suggests that the oxygen desorption occurs more effectively at reduced pressure than in other atmosphere conditions. This appears reasonable, because the release of oxygen species can be hindered at higher pressure by the enhanced collision rate with other gas molecules in the proximity of the surface, resulting in a lower net desorption rate.

Since the density of adsorbed oxygen is progressively reduced during the photoconducton process, it is likely that oxygen molecules tend to readsorb on the nanowire surface after stopping the illumination, in order to recover the oringinal equilibrium coverage. Furthermore, it is expected that, due to its high electronegativity, the oxygen readsorption is accompanied by the simultaneous trapping of photogenerated electrons at the surface and correspondingly by a decrease in the nanowire conductivity (Figure 5.5 (b)). This explains the observed drop of the photocurrent as soon as air is added to an oxygen poor atmosphere. However, the progressive accumulation of electrons at the surface is responsible for a gradual increase of the surface electrostatic potential, which hinders further adsoprtion and determines consequently the observed slowdown of the photocurrent decay rate.

A more detailed description of such recombination mechanism requires however a quantitative analysis of the temporal evolution of the photocurrent decay, including in particular its dependence on the photogenerated charge carrier density. The determination of an appropriate fitting function, which can realistically describe the adsorption-assisted electron trapping, permits in particular to overcome the limitation of previously proposed analysis procedures, which typically lack a reliable underlying physical model. Additionally, it allows to evaluate the weight of such recombination mechanism on the overall photocurrent

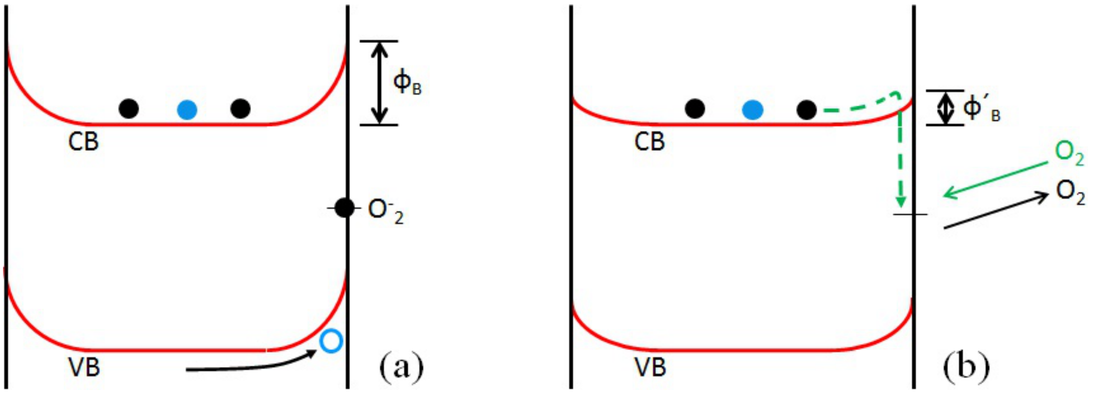

FIGURE 5.5: *The photo-generated electrons and holes in a ZnO nanowire are separated by the built-in electric field, induced by ionosorbed oxygen (a). The charge carrier lifetime is thus increased, determining a quick rise of the photoconductivity. After illumination oxygen molecules readsorb and trap simultaneously electrons from the conduction band, causing the observed drop of the photoconductivity (b). This model corresponds to that proposed by Melnick in case of porous sintered ZnO [164]. In both figures, the color of photogenerated charge carriers is blue, whereas other electrons in the conduction band determine the intrinsic n-type conductivity of ZnO and are indicated in black. The green arrows describe the re-trapping of electrons and the oxygen readsorption.*

decay, revealing the eventual partecipation of other eventual relaxation processes. These aspects will be widely discussed in the next section.

5.2 Dynamics of the photoconductivity decay

The results presented in the previous section indicate qualitatively that after above band gap excitation photogenerated electrons tend to be trapped at the surface during the simultaneous readsoprtion of oxygen molecules at the nanowire surface. This hyphotesis can be quantitatively discussed by comparing the temporal dependence of the photocurrent decay with the kinetics of the oxygen adsorption process. Indeed, if the adsorption of oxygen molecules causes the simultaneous trapping of photogenerated electrons at the surface, both processes should be characterized by the same time dependence.

Although the kinetics of oxygen adsorption on ZnO was not experimentally investigated in the frame of this thesis, previous studies revealed that it can be accurately described by the so called Elovich equation, which is widely employed for the description of adsorption processes on solids [238]. In its differential form, the Elovich equation is expressed as:

$$\frac{dq}{dt} = a \cdot e^{-bq}, \tag{5.7}$$

where q is the density of adsorbed molecules and a and b are constants, which represent respectively the initial adsorption rate and the rate of change of the adsorption energy with the coverage [188]. The integral form of equation 5.7 is given by:

$$q = \frac{1}{b} \cdot ln((ab)t + 1). \tag{5.8}$$

In view of the previous considerations, equation 5.8 can be exploited to describe also the temporal evolution of the electron trapping at the surface. Assuming the latter as the only effective recombination mechanism, the density of electrons in conduction band during the photocurrent decay is $n_{cb,Elov}(t) = n_{ph} - n_{tr,Elov}(t)$, where n_{ph} is the photoelectron density maximum and $n_{tr,Elov}(t)$ is the density of trapped electrons. The latter quantity can be expressed in terms of q, taking into account that it represents a volume density, while q is a surface density:

$$n_{tr,Elov}(t) = q \cdot \frac{S_{NW}}{V_{NW}}, \tag{5.9}$$

where S_{NW} and V_{NW} are respectively the nanowire lateral area and volume. Therefore:

$$n_{cb,Elov}(t) = n_{ph} - \frac{S_{NW}}{V_{NW}} \cdot \frac{1}{b} \cdot ln((ab)t + 1), \tag{5.10}$$

Within this approximated model, in which all other eventual recombination mechanisms are not considered, the photocurrent decay is consequently expressed as:

$$I_{Elov}(t) = S \cdot e \cdot \mu \cdot E \cdot n_{cb,Elov}(t) = S \cdot e \cdot \mu \cdot E \cdot (n_{ph} - \frac{S_{NW}}{V_{NW}} \cdot \frac{1}{b} \cdot ln((ab)t + 1)). \tag{5.11}$$

Equation 5.11 represents the required fitting function for the evaluation of the photocurrent decay in terms of the adosorption-assisted electron trapping. Since it includes the generated photocurrent maximum n_{ph} as a parameter, it is particularly suitable for the analysis of the photocurrent decay as a function of the excitation intensity.

For this purpose, photoconductivity measurements were performed in air under different excitation intensities, ranging from 20 $\mu W/cm^2$ up to 5 mW/cm^2. During every measurement, the current was initially measured in the dark for 60 s, then the samples were illuminated for 5 s and the photocurrent decay was recorded until the original dark current was completely recovered. The decay curves are shown in Figure 5.6 (a), in which

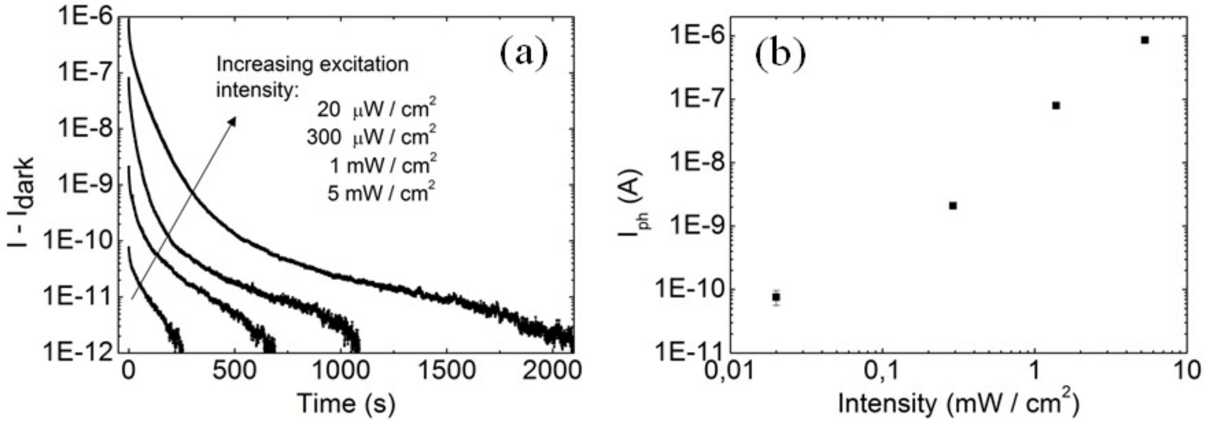

FIGURE 5.6: *Photocurrent decay in a single ZnO nanowire device after light excitation at various intensities (a). The measurements are plotted immediately after removing the illumination, which lasted for 5 s. The generated photocurrent maximum,* I_{ph}*, increases approximately linearly with the excitation intensity (b). The measurements were performed in air at* $V_{ds} = +5V$.

the photocurrent $I(t)$ - I_{dark} is plotted as a function of the time immediately after removing the illumination at t = 0. The maximum generated photocurrent I_{ph} increases approximately linearly with the excitation intensity, as evident in Figure 5.6 (b).

The experimental decay curves were fitted with equation 5.11, leaving only the constant b as a fitting parameter without constrains. The other parameters, a and n_{ph}, were instead determined prior fitting procedure.

The initial adsorption rate after illumination, a, was calculated in terms of the experimental rate of the photoelectron density decay. In principle, these two rates do not necessarely correspond, since it is not evident a priori that the adsorption-induced electron trapping is the unique mechanism responsible for the initial decay of the photocurrent. It is therefore necessary to quantify the weight of additional recombination mechansims to the initial part of the photocurrent decay in air, by comparing the decay rate observed in air, $\frac{dI}{dt}_{air,\,t=0}$, with that observed under inert atmosphere, $\frac{dI}{dt}_{inert,\,t=0}$. For this purpose, considering as a reference the measurements presented in section 5.1, both rates were determined as the slope of a linear function, which can fit the photocurrent decay within few seconds after removing the illumination (Figure 5.7). As shown in the same figure, $\frac{dI}{dt}_{air,\,t=0}$ was determined to be approximately 10 times higher than $\frac{dI}{dt}_{inert,\,t=0}$. However, it must be taken into account that air residuals were present in the chamber while measuring under inert atmospheres. The air residual concentration immediately after light excitation was quantified as the ratio between the total volume of inert gas flowing in the chamber and the original air volume prior introducing the gas, which corresponds

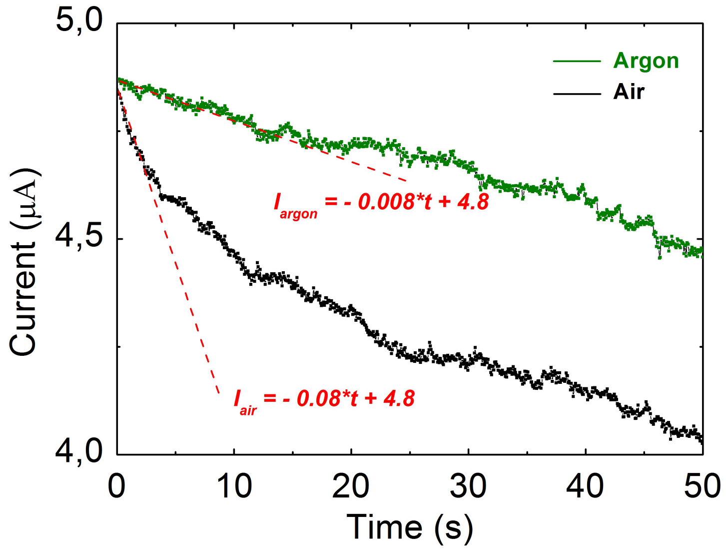

FIGURE 5.7: *Comparison between the photocurrent decay rate in a single ZnO nanowire device in air and in argon atmosphere. The dashed lines represent linear fitting functions, which fit the curves within few seconds after removing the illumination at* $t = 0$ *s. The measurements were performed at* $V_{ds} = +5V$.

obviously to the volume of the chamber. The total volume of inert gas was calculated as $V_{tot} = F_g \cdot t$, where F_g is the gas flow and t = 4 hours, which accounts for the temporal interval between letting the gas into the chamber prior the measurement (see section 3.3) and removing the UV illumination (see Figure 5.2). Considering the values of the chamber volume and the gas flow reported in section 3.3, the air concentration was estimated to be 8 times lower than that of the inert gas. The ratio between $\frac{dI}{dt}_{inert,\, t=0}$ and $\frac{dI}{dt}_{air,\, t=0}$ and that between the air residual concentration and the inert gas concentration are therefore substantially comparable. This strongly suggests that the initial photocurrent decay in argon or nitrogen is mainly caused by adsorption-assisted electron trapping, induced by residuals of oxygen in the chamber. Therefore, compared to the latter process, the weight of additional recombination mechansims to the initial part of the photocurrent decay in air must be significantly lower than 10 % and can be consequently neglected. As such, when the measurement is performed in air, the initial adsorption rate a can be approximated to the initial rate of the photoelectron density decay:

$$a \approx \frac{dn_{cb}}{dt}_{\,t=0} = \frac{1}{Se\mu E} \cdot \frac{dI}{dt}_{t=0}, \tag{5.12}$$

where n_{cb} is the electron density in the conduction band and the other quantities are defined as in the previous section.

TABLE 5.1: *Numerical values of the parameters contained in equation 5.11, which was used for fitting the photocurrent decay in ZnO nanowire devices.* a *and* n_{ph} *were determined prior fitting procedure, while* b *was obtained as fitting parameter without constrains.*

Excitation Intensity	a ($\mathrm{cm^{-2}s^{-1}}$)	b ($\mathrm{cm^{2}}$)	n_{ph} ($\mathrm{cm^{-3}}$)
20 μW/cm^2	$5{\cdot}10^{6} \pm 10^{5}$	$2{\cdot}10^{-7} \pm 10^{-9}$	$6{\cdot}10^{12} \pm 10^{10}$
300 μW/cm^2	$2{\cdot}10^{9} \pm 10^{8}$	$7{\cdot}10^{-9} \pm 10^{-11}$	$1.6{\cdot}10^{14} \pm 10^{13}$
1 mW/cm^2	$3{\cdot}10^{10} \pm 10^{9}$	$2{\cdot}10^{-10} \pm 10^{-12}$	$6.2{\cdot}10^{15} \pm 10^{14}$
5 mW/cm^2	$4{\cdot}10^{11} \pm 10^{10}$	$2{\cdot}10^{-11} \pm 10^{-12}$	$6.7{\cdot}10^{16} \pm 10^{14}$

Finally, the electron density immediately after photoexcitation, n_{ph}, was calculated from the experimental value of the photocurrent at t = 0, I_{ph}:

$$n_{ph} = \frac{I_{ph}}{Se\mu E}. \tag{5.13}$$

The obtained fitting parameters are summarized in table 5.1. These were used to fit the photocurrent decay curves, which were measured in air after light excitation at various intensities (Figure 5.8). For clarity reasons, the temporal scale of the graphs (a) (b), (c) and (d) is much reduced compared to the original one in Figure 5.6. An excellent accordance between the experimetal data and equation 5.11 is observable within few tens of seconds after light excitation. A following discrepancy can be appreciated, due to the slower experimental decay compared to the one theoretically predicted. As a quantitative criterium, it is assumed that the experimental curve starts to deviate from the theoretical one when the discrepancy amounts at least the estimated noise level of the measurements, otherwise the deviation is considered as not significant. The noise level was estimated as the standard deviation of a constant current flowing through the sample under equilibrium conditions. The measurement was carried out with several contacted nanowires grown under the same conditions, in order to obtain a large and reliable statistics. The results allowed to conclude that the noise amounts on average to 5-10% of the current value. Assuming 10% as a reference value, the photocurrent at which the discrepancy becomes significant and the corresponding intercept on the temporal scale were determined and highlighted in figure 5.8. The relative decay ratio was then calculated for every excitation intensity as the difference between I_{ph} and the highlighted current value (I_{tr}), divided by I_{ph}:

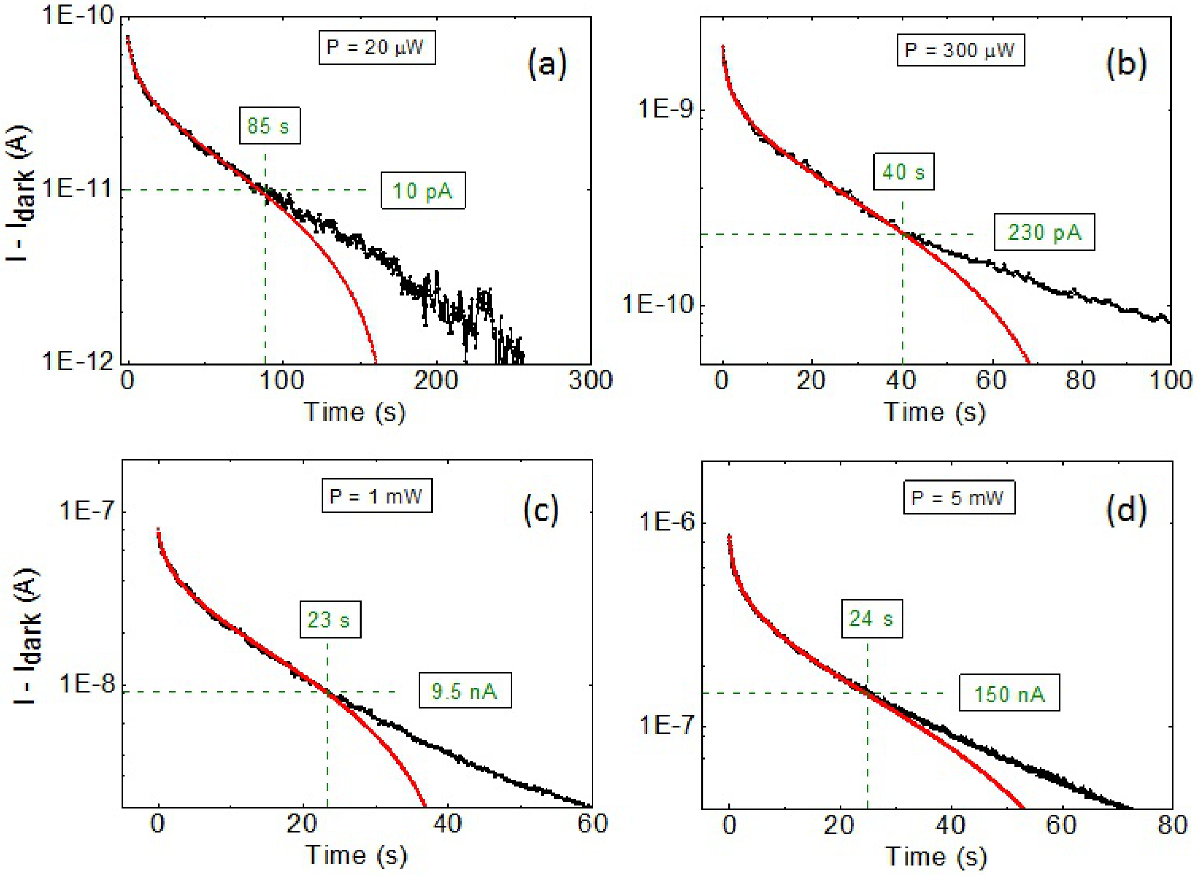

FIGURE 5.8: *Photocurrent decay curves measured in air after light excitation at various intensities are fitted in red with equation 5.11, which is based on the Elovich equation for adsorption processes. The fitting procedure shows an excellent agreement within few few tens of seconds after illumination. Afterwards, the experimental decay proceeds in all investigated cases faster than that theoretically predicted.*

$$\Delta I_{rel,Elov} = \frac{I_{ph} - I_{tr}}{I_{ph}}. \tag{5.14}$$

As shown in Fugure 5.9, $\Delta I_{rel,Elov}$ amounts approximately to 0.9 independently on the generated photocurrent, indicating that around 90 % of the photogenerated electrons recombine through the adsorption-assisted trapping mechanism. Furthermore, the time required to observe such partial decay shortens progressively as the excitation intensity increases.

Such shortening of the recombination time can be explained by considering a simple electrostatic model describing the surface trapping process. In order to penetrate to the surface and there get trapped, electrons must must overcome the electrostatic barrier

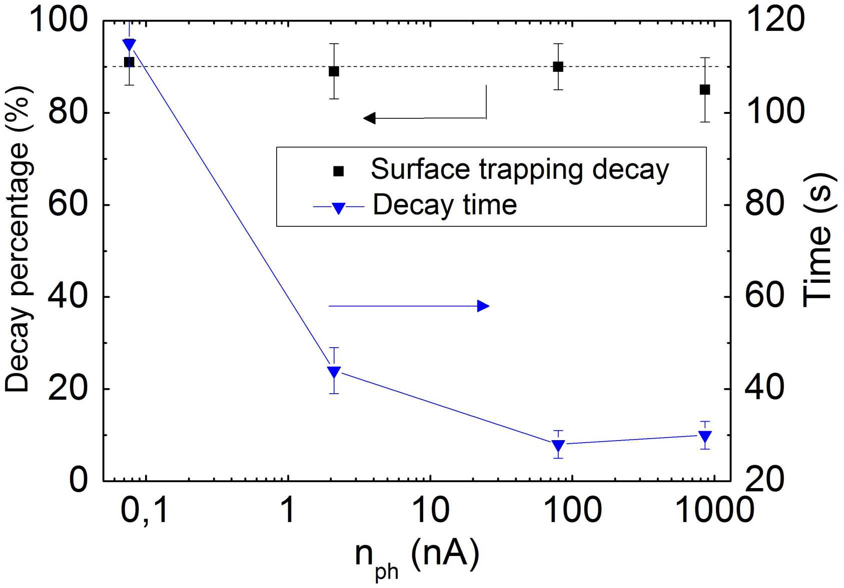

FIGURE 5.9: *The fraction of the experimental photocurrent, which decays in accordance with equation 5.11, is plotted as a function of the photoelectron density maximum. This fraction amounts approximately to 0.9 in all investigated cases. The time required to observe this partial photocurrent decay is shown in the same graph. This reduces progressively as the photocurrent maximum increases.*

originating from the negatively charged ionosorbed oxygen. As such, the penetration rate is expressed in terms of the corresponding Boltzmann factor as [164]:

$$\frac{dn_{tr}}{dt} \propto exp(-\frac{\phi}{kT}). \tag{5.15}$$

The height of the barrier ϕ is proportional to the density of adsorbed molecules (see equation 2.2), and can be therefore reduced by the hole-induced surface discharge during photoexcitation. Accordingly, it is expected that an increasingly excitation intensity leads to a stronger reduction of the surface barrier and consequently to a faster trapping rate after illumination, as experimentally observed. The dynamics of this process is schematically depicted in Figure 5.10, where (a) describes the surface band bending in dark and (b) and (c) the modulation of the surface barrier height as a function of increasing excitation intensity.

On the other hand, the relaxation of the remaining 10% of charge carriers dominates the long-term overall photocurrent decay process. This can be appreciated in Figure 5.11, by comparing the corresponding recovery time ($\tau_{10\%,rest}$) as a function of I_{ph} with that required to observe the first 90 % of the relaxation ($\tau_{90\%}$) and the complete recovery of the dark current ($\tau_{100\%}$). The recovery time $\tau_{10\%,rest}$ was calculated as the difference between

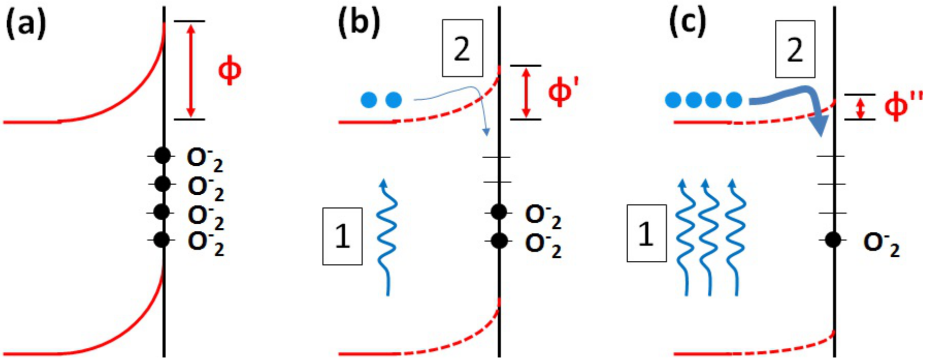

FIGURE 5.10: *The influence of the light excitation intensity on the surface discharge process is illustrated. The surface band bend bending in dark, induced by ionosorbed oxygen, is shown in (a), with the corresponding electrostatic potential* Φ*. Under photoexcitation (step 1)* Φ *is gradually reduced (b). As the excitation intensity increases, the reduction becomes more significant (c). As a result, the oxygen readsorption and the simultaneous electron trapping (step 2) proceed progressively faster as the excitation intensity increases.*

$\tau_{100\%}$ and $\tau_{90\%}$. The similarity between $\tau_{100\%}$ and $\tau_{10\%,rest}$, particularly at high excitation intensity, is evident. Furthermore, unlike $\tau_{90\%}$, $\tau_{10\%,rest}$ becomes progressively longer as I_{ph} increases.

A deeper insight into the nature of the involved relaxation mechanisms was gained by investigating the temporal evolution of the corresponding photocurrent decay. As shown in Figure 5.12 (a), the tail for long times of all decay curves can be well fitted with a simple exponential function, whose recombination constant (see Figure 5.12 (b)) increases with the excitation intensity. At low excitation intensity, this exponential component completely describes the remaining 10 % of the decay. This can be appreciated in the same figure, where also the fitting curve corresponding to equation 5.11 is added to the plot. As the excitation intensity increases, an additional intermediate component appears, which does not show a pure exponential character. Such non exponential component of the decay might be related to several factors, including a possible deviation of the adsorption kinetics from the Elovich equation or the superposition between various recombination processes.

The simple exponential profile of the decay tail indicates instead the dominance of a single recombination mechanism. The functional form of an exponential photocurrent decay is compared in the following with that related to a surface trapping process, in order to clarify whether the observed exponential component can attributed to a surface related

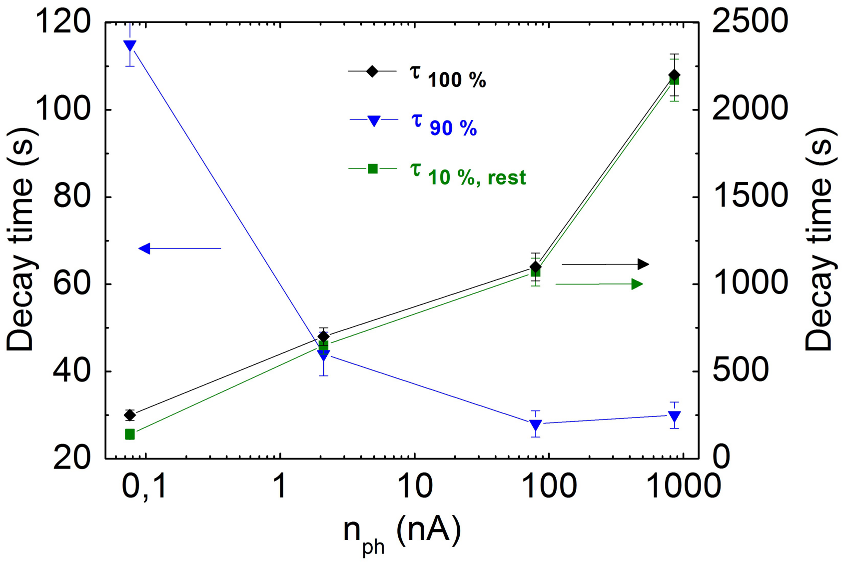

FIGURE 5.11: *The full recovery time* $\tau_{100\%}$ *is compared with the time required to observe 90 % of the photocurrent decay (*$\tau_{90\%}$*) and that to observe the remaining 10 % (*$\tau_{10\%,rest}$*). The similarity between the former and the latter is clearly appreciable.*

process. The rate of a pure exponential photocurrent decay is simply proportional to the density of electrons in conduction band:

$$(\frac{dn_{cb}}{dt})_{exp} \propto -n_{cb}. \tag{5.16}$$

On the other hand, the rate of a surface trapping process can be written including the corresponding Boltzmann factor, as well as its dependence on the density of non occupied surface states available for the trapping process, $N_{s,0}$ [239]:

$$(\frac{dn_{tr}}{dt})_{trap} \propto N_{s,0} \cdot exp(-\frac{\phi}{kT}). \tag{5.17}$$

Assuming that non occupied surface states are formed during light excitation as a result of the hole-induced surface discharge, their density is proportional to the density of photogenerated electrons in the conduction band n_{cb}: $N_{s,0} = b \cdot n_{cb}$. The constant b, which is comprised between 0 and 1, represents the efficiency of the discharge process. Therefore, equation 5.17 can be rewritten as:

$$(\frac{dn_{tr}}{dt})_{trap} \propto n_{cb} \cdot exp(-\frac{\phi}{kT}). \tag{5.18}$$

Assuming that the decay is entirely caused by the surface trapping process, $n_{cb} = n_{ph} - n_{tr}$, and, correspondingly:

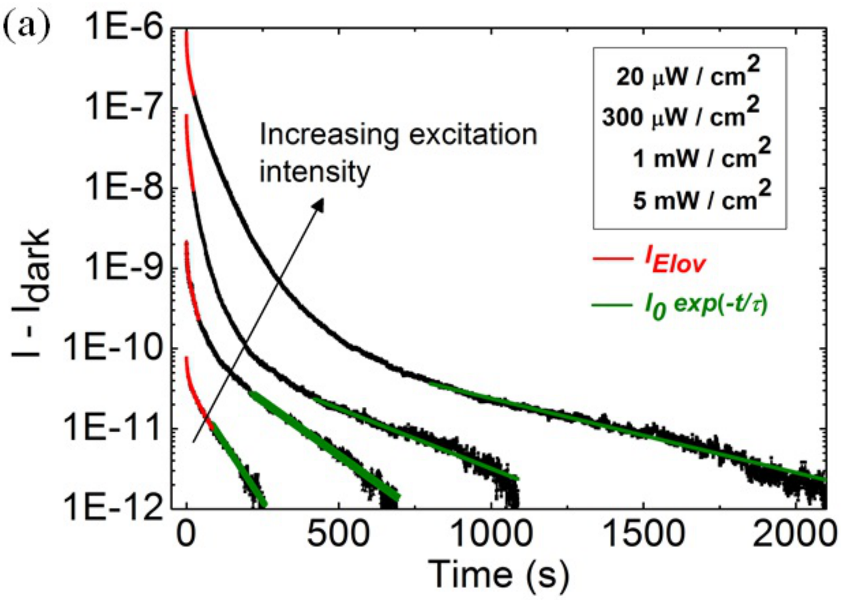

(b)

Excitation intensity	Recovery Time (τ)
20 μW / cm ^{2}	(75 ± 10) s
300 μW / cm ^{2}	(160 ± 20) s
1 mW / cm ^{2}	(270 ± 25) s
5 mW / cm ^{2}	(470 ± 50) s

FIGURE 5.12: *Exponential fitting of the photocurrent decay tail after light excitation at various excitation intensity (a). The corresponding recombination time, shown in the underlying table (b), increases progressively with the excitation intensity.*

$$(\frac{dn_{cb}}{dt})_{trap} = -\frac{dn_{tr}}{dt} \propto n_{cb} \cdot exp(-\frac{\phi}{kT}). \tag{5.19}$$

Finally, expressing ϕ as in equation 2.2 in terms of n_{tr}:

$$(\frac{dn_{cb}}{dt})_{trap} \propto -n_{cb} \cdot exp(-\frac{\frac{e^2 n_{tr}^2}{2N\epsilon_0\epsilon_r}}{kT}). \tag{5.20}$$

Comparing equations 5.20 and 5.16 it can be observed that both rates are proportional to the density of electrons in conduction band. However, the exponential one lacks the dependence on the surface barrier, or in other terms, on the density of trapped electrons at the surface, which progressively increases as the decay proceeds and represents consequently a self-limitation factor for further electron trapping. This consideration indicates that the observed exponential component of the photocurrent decay is caused by a different mechanisms, rather than by a pure electron trapping at surface states. As such, previous studies [235, 240, 241], which attributed the observed exponential photocurrent decay to the surface trapping process, should be considered suspiciously.

More in general, also trapping of photogenerated electrons at defect states located in the surface depletion region can be ruled out as a possible relaxation mechanism. The occupation probability of such trap levels and consequently their trapping rate critically depend on their position in respect to the Fermi level, which is affected by the profile of the surface band bending [217]. Since the latter enlarges during the photocurrent decay, due to the progressive decrease of the electron density (see equation 2.1), the trap levels are progressively shifted up in respect to the Fermi level and their occupation probability consequently decreases. Similarly to what previously described in case of adsorption-assisted electron trapping, this represents a self-limitation factor for the recombination of charge carriers in the surface depletion region. As such, the rate of such relaxation process cannot be simply proportional to the density of electrons in conduction band, as in case of a simple exponential function.

Therefore, the exponential tail of the photocurrent decay seems to be prevalently related to the slow recombination of charge carriers in the core of the nanowire. As introduced in section 2.5, the prolonged lifetime of electrons in the conduction band can be caused in principle by two main distinct mechanisms, namely the trapping of electrons in metastable excited states of oxygen vacancies or the trapping of holes at localized levels in the band gap. However, the former process would require the photoexcitation of oxygen vacancies, which does not occur as suggested by the absence of photoresponse under below band gap excitation. The contribution of such highly conductive metastable electron states to the PPC can be thus ruled out. Consequently, the exponential component of the PPC is most probably caused by the reduced electron - hole recombination probability, induced by the hole trapping at bulk defect states.

The measurements performed do not allow to univocally determine the specific nature of these trap levels, which could be in principle revealed by a detailed investigation of the active electron - hole recombination paths. Among the radiative ones, the most commonly observed in as grown ZnO include the direct recombination of electrons from the conduction band with trapped holes at such defect levels [242] or the recombination following the thermal release of trapped holes into the valence band [243]. The rate of the latter recombination mechanism, in particular, is expected to increase with the temperature, since the de-trapping process is typically activated by phonons. It might be thus effectively involved in the exponential component of the photocurrent relaxation, since a significant reduction of the PPC has been observed in several semiconductors for decreasing temperature [150, 236, 239, 244]. However, in most of the previous studies the experimental decay curves were simply fitted with a phenomenological strechted exponential function, in which the superposition of several recombination processes is described by a single constant parameter. Consequently, such analysis procedure does not allow to independently evaluate the influence of the temperature on distinct recombination mechanisms. Therefore, previous results cannot be conclusively compared with that presented in this section and further photoconductivity measurements as a function of the temperature would be highly beneficial for a deeper insight on bulk processes responsible for the appearence of the PPC in ZnO nanowires.

In view of the discussed results, some conclusive comments can be done. Firsty, the results presented in this section indicate that, within the investigated excitation intensity range, only the minority of the photogenerated holes get trapped at bulk states, while the majority migrate to the surface and contribute to the desorption of ionosorbed oxygen. These results are consistent with previous time resolved photoluminescence studies, which revealed the higher hole trapping efficiency of surface states compared to other trap levels [245]. However, this conclusion might be not true in case of significantly higher excitation intensity. Indeed, under the highest excitation intensity considered (5 mW/cm^2), the generated photocurrent amounts to $I_{ph} \approx 1$ μA. This corresponds to a hole density of $n_h = I_{ph}/Se\mu E \approx 10^{17}$ cm^{-3}, which per nanowire volume ($\approx 10^{-13}$ cm^3) amounts to $\approx 10^4$. Such value is comparable to the expected density of adsorbed oxygen per nanowire surface under equilibrium conditions: $S_{ads,NW} = S_{ads} \cdot A_{NW} \approx 10^4$ - 10^5 (see section 2.2.2) and is therefore close to the maximum density of holes, which can be entirely involved in the surface discharge process. If the excitation intensity exceeds few tens of mW/cm^2, it is thus expected that an increasing fraction of photogenerated holes can be trapped through other mechanisms, in particular involving bulk trap levels. This may have obviously a dramatic influence on the dynamics of the charge carrier recombination, which should be carefully considered in view of photodection applications with ZnO nanowires.

Secondly, the common perception, according to which the appearence of the PPC in ZnO nanowires is primarily caused by the slow re-adsoprtion of oxygen at the surface, should be partially changed. Indeed, although it involves the majoity of photogenerated electrons (at least 90 %), the adsorption-assisted surface trapping proceeds relatively fast compared to other bulk trapping processes, which dominate the slow tail of the photocurrent decay. Within this perspective, the decay of the photocurrent can be effectively described in terms of fast and slow components, as suggested in few previous studies but without any specific identification of the involved mechanisms [235, 246]. The obtained results reveal correspondingly the inadequacy of more commonly adopted analysis approaches, which are typically based on the modelling of the photocurrent decay with simple or stretched exponential functions.

The proposed approach, based on the comparison between the dynamics of the photocurrent decay and the kinetics of the oxygen adospriton, can be extended also to other structures based on ZnO and more generally to other semicondutors, such as various metal oxides and GaN, whose photoconductivity properties strongly depend on the surrounding environment [247–249].

5.3 Conclusions

In this chapter the above band gap photoconductivtiy properties of contated ZnO nanowires have been investigated, focusing in particular on their dependence on the atmosphere conditions. For this purpose, photoconductivity measurements under UV excitation were performed in vacuum, inert amospheres and air.

High photoresponse has been observed in all considered conditions, with responsivity up $10^6 \frac{A}{W}$ in vacuum and slighly lower in other atmospheres. The photoconduction process has been attributed to the discharge of the surface, as a result of iosorbed oxygen desoprtion.

The decay of the photocurrent shows a strong dependence on the surrounding environment, being particularly slow in vacuum and inert atmospheres. The charge carrier relaxation proceeds instead faster in air, due to the readsorbtion of oxygen molecules and the simultaneuos trapping of electrons at the surface.

This process has been quantitatively evaluated by comparing the temporal evolution of the decay with the kinetics of the oxygen adsorption. The latter has been described assuming that the adsorption rate follows the Elovich equation. The analysis revealed that, in the investigated light excitation range, approximately 90 % of charge carriers recombine through the adsorption-assisted surface trapping within few tens of seconds. The rest of the photocurrent decay proceeds instead much slower, in the order of hundreds or thousands of seconds, and is caused by different recombination mechanisms, which include in particular hole trapping in the nanowire volume.

Chapter 6

Activation of Al dopants in ZnO nanowires

This chapter reports on argon and aluminum implantation in ZnO nanowires, focusing in particular on the thermal stability as well as on the electrical, optical and photoconductivity properties of the implanted nanowires. The photoluminescence measurements were performed in collaboration with Robert Röder, while the electrical characterization were conducted in collaboration with Michelle Geelen within the scope of her Master thesis [250]. The implantation of the nanowires were carried out with the support of Andreas Johannes.

6.1 Introduction

Enhancement of the n-type conductivity of ZnO nanowires by doping is essential in view of various applications, especially in transparent and flexible eletronics [251] and, in conjunction with eventual future achievements in p-type doping, for the development of ZnO NW based LEDs and laser diodes. In particular, it has been claimed that the use of ZnO nanowires as a buiding component in transparent transistors [252] as well as in conductive window layers and anti-reflection coatings in solar cells [253, 254] may present several advantages over the corresponding technology based on thin films, including for instance higher flexibility, lower reflectivity and more efficient fabrication procedures [253]. Additional successful applications of n-type doped ZnO nanowires include the development of gas sensors [255, 256], novel photoswitches [257] and memory devices [258].

Among possible donor impurities in ZnO (see section also 2.1.4), aluminiun is one of the most commonly used because of its large availability, low cost and non toxicity.

Aluminum doping of ZnO nanowires during growth has been successfully performed by means of several methodes, including thermal evaporation [259], low temperature solution synthesis [128, 260], sol-gel spin-coating technique [261], and chemical vapor deposition [262].

On the other hand, the literature about attempts to dope ZnO nanowires with aluminum by post-growth ion beam implantation is rare, leaving this issue substantially unexplored. As introduced in section 2.1.4, ion beam implantation offers various advantages over other doping techiques, including in particular the possibility to introduce the desired impurities in the semiconductor crystal beyond their solubility limit and to achieve a homogeneous doping profile. As a drawback, a large density of defects may be generated during the implantation process, which can dramatically alter and deteriorate the electrical and optical properties of the implanted semiconductor. As such, post-implantation thermal treatments are typically performed, in order to recover the original crystal structure and to activate the implanted ions. However, this is a critical issue in case of contacted nanowires, since at the high temperatures typically required for this purpose, effects such as alloying near the contact regions [212], formation of new interface states [263] and eventually sample degradation [220, 264, 265] may occur. Therefore, a detailed investigation of the thermal stability properties of aluminum implanted contacted ZnO nanowires is highly required, in order to optimize the annealing conditions and more in general the entire doping procedure. This would be greatly beneficial for a more intense exploitation of the ion implantation technique for the doping of contacted ZnO nanowires.

Particularly important is also the analysis of the electrical properties of the implanted nanowires in dark as well as under illumination conditions. First of all, since some of the generated intrinsic defects may act as shallow donors (see also section 2.1.1), it is crucial to distinguish their contribution to the conductivity from that which can be attributed to the implanted aluminum atoms. For this reason, it is fundamental to investigate the electrical properties of argon implanted ZnO nanowires, in which the only expected effect of the implantation process is the generation of defects in the nanowire. Secondly, a deep understanding of the photoconduction process in the implanted nanowires is highly desirable, since the introduced impurities and the generated defects in the host crystal may drastically affect the photoresponse of ZnO, as well as the dynamics of the photoconductivity decay after light excitation. Specifically, the aluminum-related and intrinsic levels may be photoactive or act as trap centers for charge carriers, affecting consequently the electron-hole recombination rate. Additionally, change in the donor density determines a modification of the surface band bending, since the latter depends directly on the charge carrier density (see equation 2.1). As such, aluminum doping may drastically affect surface-related processes such as the electron-hole separation and the adsorption-assisted trapping at the surface of photogenerated electrons, which were described in Chapter 5 and play a fundamental role in the photoconduction process in ZnO nanowires.

6.2 Implantation procedure

The aluminum implantations were performed on contacted ZnO nanowires (see also section 3.2) with diameter between 300 nm and 400 nm at the IFK/Jena using the implanter ROMEO (see also section 3.5). The distribution of the implanted ions in the crystal was simulated prior the implantation procedure using the Monte Carlo package SRIM [206, 207]. According to the simulation results, ion energy of 100 keV and fluence of $1.25 \cdot 10^{14}$ cm^{-2} were selected as the optimal implantation parameters, in order to obtain an aluminum concentration maximum of around 10^{19} cm^{-3} at a depth of 100 nm.

Additionally, similar samples were implanted with argon, in order to separately investigate the influence of the generated intrinsic defects on the optical and electrical properties of contacted ZnO nanowires. The implantations were performed with an ion energy of 160 keV and a fluence of $1.1 \cdot 10^{14}$ cm^{-2}, in order to obtain a comparable ion range profile as in the aluminum implanted nanowires.

According to the SRIM simulations, the density of defects, which were generated at the interface between the nanowires and the SiO_2 interface, as well as near the contact regions, is substantially negligible.

6.3 Thermal stability of implanted ZnO nanowire devices

At the investigated ion energies and fluences only formation of point defects is expected in ZnO nanowires, while amorphization does not likely occur [266–268]. This is due to the high resistence of ZnO to the ion-beam damaging and the occurrence of pronounced dynamic annealing effects during implantation, which are typically observed in highly ionic semiconductors and determine the immediate disappearence of a large fraction of defects [269–272]. Nevertheless, the significant formation of defects during argon implantation is proved by the drastic reduction of the dark conductivity in the implanted sample immediately after implantation (Figure 6.1 (a)). The I-V characteristics of sam-

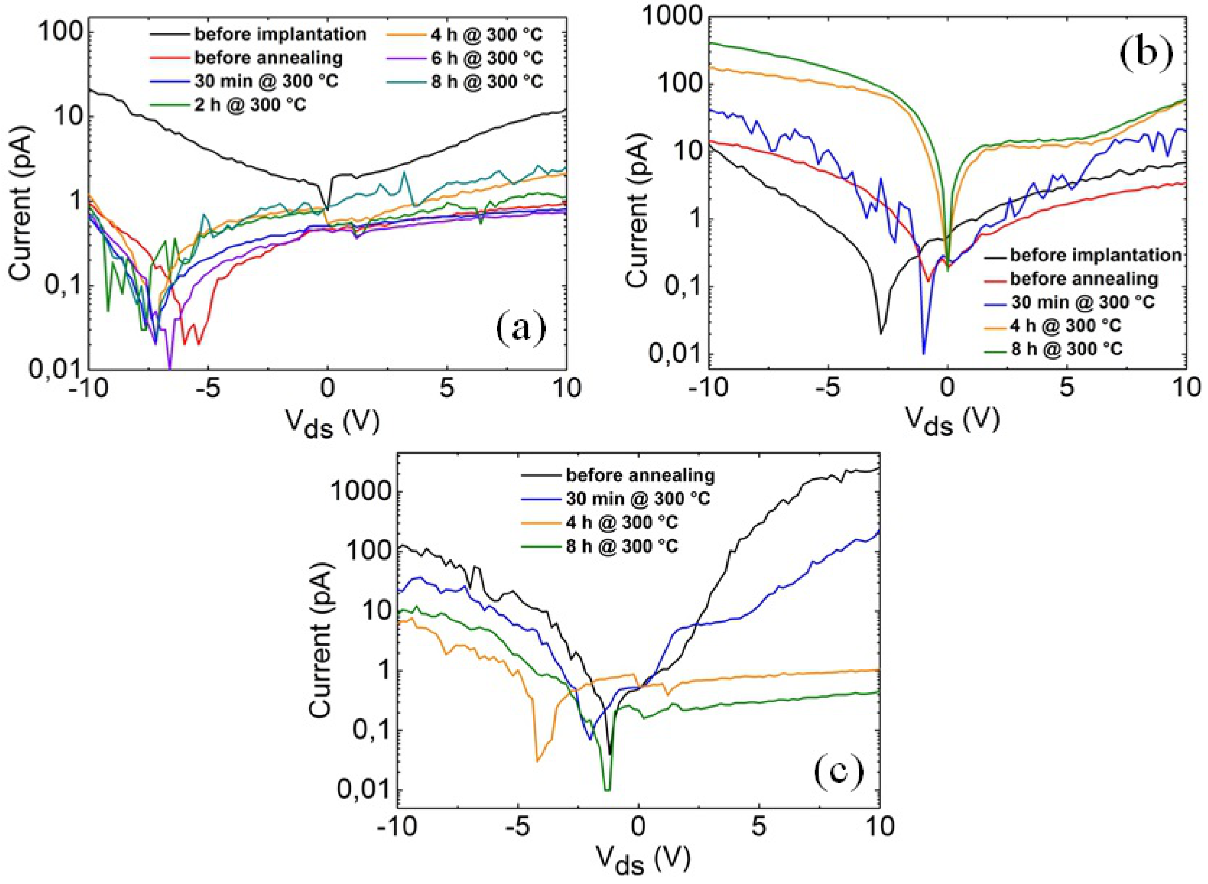

FIGURE 6.1: *I-V characteristics of contacted ZnO nanowires before and after argon (a) and aluminum implantation (b) and following post-implantation annealing treatments. Argon implanted nanowires are seriously deteriored by the implantation process, while increase in the conductivity is observed after aluminum implantation. The I-V characteristics of a non implanted sample, which is used as a reference for the annealing procedures, are presented in (c).*

ple before and immediately after aluminum implantation are instead substantially similar (Figure 6.1 (b)), probably due to the lower concentration of generated defects or to the counteracting effect of the incorporated aluminum ions, which may act as shallow donors even immediately after implantation. Annealing procedures were then performed, in order to drastically reduce the concentration of generated defects. In general, the optimal temperature of a post-implantation annealing treatment strongly depends on the defect formation process, which is typically affected by the nature of the target material as well as on the mass and the chemical nature of the implanted ions. For instance, in uncontacted ZnO nanowires implanted with transition metals or rare earths the original crystal structure is recovered after annealing treatments in the temperature range between 700 °C and 900 °C [204, 273], while a lower temperature (500 °C) is required after argon implantation [274]. However, it has been shown that annealing performed in air at temperature higher than 350 °C with contacted ZnO nanowires leads to a complete sample degradation [220], which can be mainly attributed to the large modification of the contact properties due to the occurrence of allowing effects of the ZnO nanowires with Ti and Au.

Thus, argon and aluminum implanted ZnO nanwoires were annealed at 300 °C. Various annealing durations were considered, in order to investigate the thermal stability of the device with the implanted nanowires and to optimize the conditions of the thermal treatment. Additionally, a pristine non-implanted sample was repeatedly annealed under the same conditions and used as a reference, in order to distinghish the modifications induced by the implantation process from that eventually related to the annealing procedure.

As shown in Figure 6.1 (b), a thermal treatment for 30 min does not induce any appreciable change in the I-V characteristics of the aluminum implanted sample, while a substantial increase of the dark conductivity, by more than one order of magnitude, is observed after 4 hours annealing. A further thermal treatment for 8 hours leads only to a slight improvment of the I-V characteristics, indicating the eventual saturation of the conductivity increase. Since the thermal treatments were performed at relatively low temperature, it is unlikely that the original crystal structure of the nanowires is completely recovered. This assumption is also corroborated by the investigation of the optical properties of the implanted nanowires, which will be discussed in the next section. It is therefore likely that the observed saturation of the conductivity increase is caused by the occurrence of the previously mentioned thermally-induced degradation effects.

On the other hand, the device conductivity is drastically reduced in the argon implanted sample immediately after implantation and is not recovered after analogous annealing procedures (Figure 6.1 (a)). Deterioration of the I-V characteristics is also observed in the annealed reference sample (Figure 6.1 (c)). As such, the observed increase of the conductivity in aluminum implanted ZnO nanowires can be entirely attributed to the partial recovery of the crystallinity and simultaneous ionization of the aluminum donors, without significant contribution from intrinsic defects.

SEM pictures taken after implantation and following annealing treatments reveal that the implantation process does not induce apprecciable surface roughness, although a slight reduction of the nanowire diameter can be observed after argon implantation (Figure 6.2). This can be attributed to the occurrence of sputtering effects, which are induced by the implanted argon ions [275].

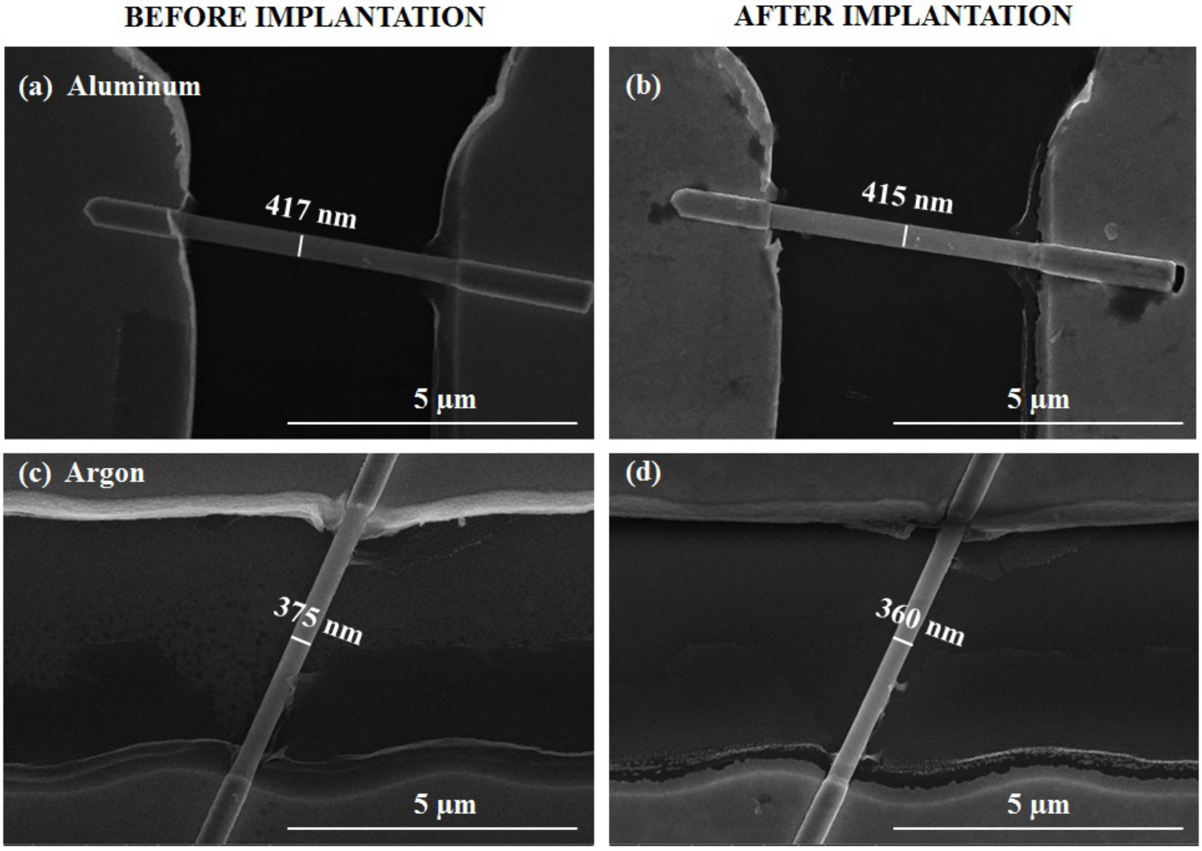

FIGURE 6.2: *SEM pictures of contacted ZnO nanowires after argon and aluminum implantation and following post-implantation annealing treatments. Both implantation processes do not induce apprecciable surface roughness. Only a slight reduction of the nanowire diameter can be observed after argon implantation.*

6.4 Optical properties of implanted ZnO nanowires

The impact of the aluminum and argon implantation on the optical properties of the contacted ZnO nanowires was investigated by means of micro-photoluminescence spectroscopy. The measurements were performed at 4 K after the longest post-implantation annealing (8 hours), using a He-Cd laser as excitation light source at 325 nm.

The complete spectra of the implanted samples are shown in Figure 6.3. As a reference, the spectra of an untreated contacted nanowire is added to the graph. All spectra are characterized by two distinct emission bands, namely the near band edge emission (NBE) and the deep level emission (DLE) of ZnO, which are located respectively in the UV and in the visible spectral range. The photoluminescence intensity is normalized in respect to the NBE.

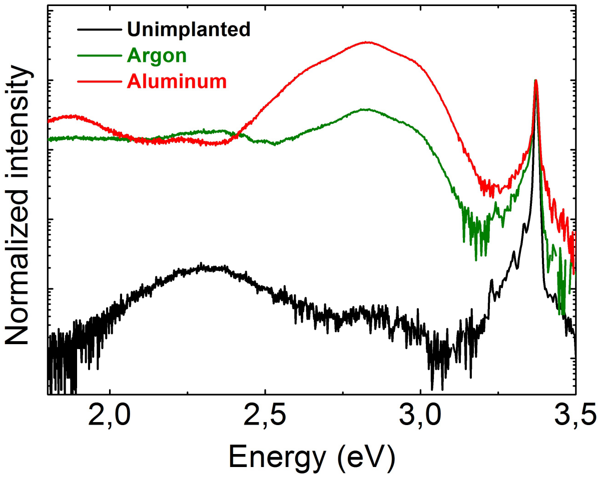

FIGURE 6.3: *Photoluminescence spectra of contacted ZnO nanowires before and after argon and aluminum implantation. The samples underwent various post-implantation annealing treatments at 300 °C, with maximum duration of 8 hours. The spectrum of a pristine sample is also presented. The spectra are characterized by a near band edge emission in the UV spectral range and a broad emission band in the visible range, which is caused by various recombinations at deep levels. The band centered around 2.8 eV is an artifact of the PL seput.*

The DLE of the pristine sample is dominated by the green luminescence, which has the maximum intensity at around 2.4 eV. This emission originates from the recombination at defect levels located in the bulk as well as at the nanowire surface, including in particular oxygen and zinc vacancies [276–279]. The NBE results instead from the overlap of various excitonic emissions, which will be described in more detail in the following paragraph. In comparison to the pristine sample, the NBE of the implanted nanowires is much broader and the ratio with the DLE decreases, indicating that the performed annealing procedures do not completely recover the original crystal structure of the nanowires. Moreover, an additional component of the DLE, which is substantially absent in the as-grown nanowires, appears in the argon and especially in the aluminum implantend samples at photon energies lower than 2 eV. This can be attributed to the recombination between donor levels and oxygen interstitials [280, 281], which can be likely generated during implantation, while are typically present in low concentration in as grown ZnO nanowires (see also section 2.1.1). The large band centered around 2.8 eV is instead an artifact of the PL measurement setup, which was caused by the back reflection of white light into the monochromator.

High resolution spectra of the NBE from the same nanowires are shown in Figure 6.4 (a). The dominant emission peak is centered approximately at 3.36 eV in all investigated

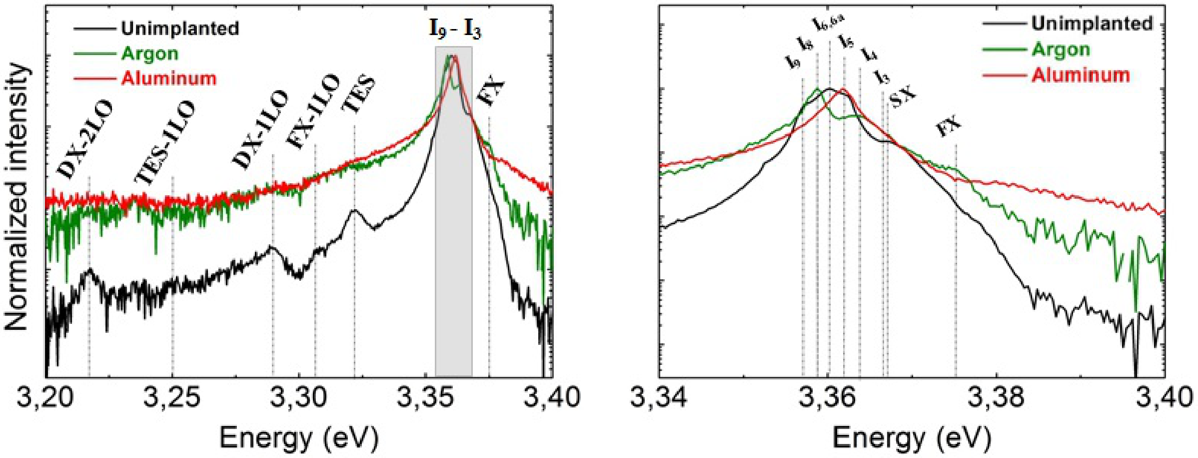

FIGURE 6.4: *High resolution photoluminescence spectra of the near band edge emission (NBE) of contacted ZnO nanowires before and after argon and aluminum implantation (a). The spectrum of a pristine sample is also presented. A close up of the NBE maximum in (b) shows the main emission lines, which are caused by the recombination of bound excitons.*

samples and is composed by various emission bands (I_9 - I_3), which are highlighted more in detail in Figure 6.4 (b) and are related to the recombination of several neutral donor bound excitons (D^0X) [282, 283]. The NBE from the pristine sample is dominated by the lines $I_{6,6a}$ and I_5, which are related to aluminum acting as a shallow donor [282, 284]. This was probably incorporated as a trace during growth of the ZnO nanowires from the Al_2O_3 boat and the tube of the furnace. In the pristine sample also the emission lines I_9, I_8, I_4 and the SX can be recognized. The former two are typically attributed to excitons bound respectively to indium [285] and gallium [286], which are present as contamination impurities in the used ZnO powder, while I_4 is related to hydrogen acting as a shallow donor [282], which is also unintentionally incorporated during growth. The emission line SX is instead assigned to surface bound excitons (SX) [287, 288]. The emission line I_5 fully dominates the NBE emission from the aluminum implanted sample, proving thus the optical activation of implanted aluminum atoms as shallow donors. On the other hand, it is much weaker in the argon implanted sample. Additionally, in both implanted samples also the line I_3 can be recognized, which is related to Zn interstitials eventually generated during implantation. The high energy shoulder of the NBE originates instead from the free exciton recombination (FX) [289], while on the lower energy side several peaks can be recognized. These include in particular the two-electron-satellite emission (TES) [282], which occurs when the neutral donor is excited from the 1s ground state to an excited state after recombination of the bound exciton [290], and the longitudinal phonon replica

1LO and 2LO of the excitonic emissions [282]. Such emission lines substantially disappear after argon and aluminum implantation, indicating once again the non complete recovery of the crystal structure after the post-implantation annealing procedures.

6.5 Photoconductivity properties of implanted ZnO nanowires

6.5.1 Photoresponse

The impact of the ion implantation on the photoresponse properties of contacted ZnO nanowires was investigated by measuring the photocurrent in air under steady state excitation conditions before and after implantation. The measurements were conducted under UV illumination at 20 μW/cm^2 and 5 mW/cm^2, in order to explore different excitation intensity regimes. Additionally, also the photoresponse properties of the reference sample for the annealing procedures were investigated, in order to distiguish the modifications induced by the implantation process from that eventually attributable to the post-implantation annealing procedure. In particular, thermal treatments may affect the photoconduction process mainly due the induced change in the defect concentration, as well as the modification of the contact and surface properties.

The measured values of the dark current (I_{dark}) and the photocurrent (I_{ph}) are summarized in table 6.1. Immediately after argon implantation and the following annealing for 4 hours, the dark current and the photocurrent values were below the sensitivity of the SMU and are thus not reported. The photoresponse is quantified in Figure 6.5 in terms of the photosensitivity, which is the ratio between I_{ph} and I_{dark}.

Enhanced photoresponse is observed in the sample implanted with aluminum after post implantation annealing under light excitation at 20 μW/cm^2 (Figure 6.5 (a)). In particular, a progressive increase of the annealing duration leads to increasing photosensitivity. However, this effect cannot be simply attributed to the gradual recovery of the crystal structure, since decreasing photosensitivity is observed in the argon implanted as well as in the reference sample after analogous annealing treatments. Although the literature about this point is quite rare, enhancement of the photoresponse under below band gap excitation has been observed in porous aluminium-doped zinc oxide nanofibers and attributed to the photoexcitation of aluminum related shallow levels [257]. A similar effect might thus also occur in the nanowires investigated within this work. On the other hand, decreased photoresponse is observed in all samples under excitation at 5 mW/cm^2. The

Table 6.1: *Values of the dark current and the photocurrent in contacted ZnO nanowires before and after argon and aluminum implantation. The corresponding values of a non-implanted sample, which is used as a reference for the annealing procedures, are also presented. The missing values marked as X in the argon implanted sample were lower than the SMU sensitivity and are therefore not reported.*

Sample	**Treatment**	$\mathbf{I}_{dark}$	$\mathbf{I}_{UV}$ **(20 μW)**	$\mathbf{I}_{UV}$ **(5 mW)**
Al implanted	Before Implantation	(0.10 ± 0.05) pA	(9 ± 1) pA	(46 ± 4) nA
	After Implantation, before annealing	(1.0 ± 0.3) pA	(4.7 ± 0.5) pA	(0.66 ± 0.08) nA
	After Implantation and annealing (4h at 300 °C)	(10 ± 1) pA	(1.4 ± 0.2) nA	(0.32 ± 0.05) μA
	After Implantation and annealing (8h at 300 °C)	(15 ± 1) pA	(3.8 ± 0.5) nA	(0.73 ± 0.05) μA
Ar implanted	Before Implantation	(1.5 ± 0.5) pA	(3.0 ± 0.5) pA	(13 ± 1) nA
	After Implantation, before annealing	X	X	X
	After Implantation and annealing (4h at 300 °C)	X	X	X
	After Implantation and annealing (8h at 300 °C)	(0.1 ± 0.05) pA	X	(2.2 ± 0.3) pA
Annealed reference	Before Annealing	(0.3 ± 0.05) pA	(85 ± 1) pA	(0.33 ± 0.05) nA
	After annealing (4h at 300 °C)	(0.1 ± 0.05) pA	(5.3 ± 0.7) pA	(82 ± 1) pA
	After annealing (8h at 300 °C)	(0.10 ± 0.05) pA	(4.7 ± 0.5) pA	(8 ± 1) pA

evidence that the photosensitivity of aluminum implanted ZnO nanowires is effectively enhanced only under excitation at low intensity, suggests that the photogeneration of higher density of charge carriers leads most likely to enhanced scattering effects, which cause the observed reduction of the photosensitivity.

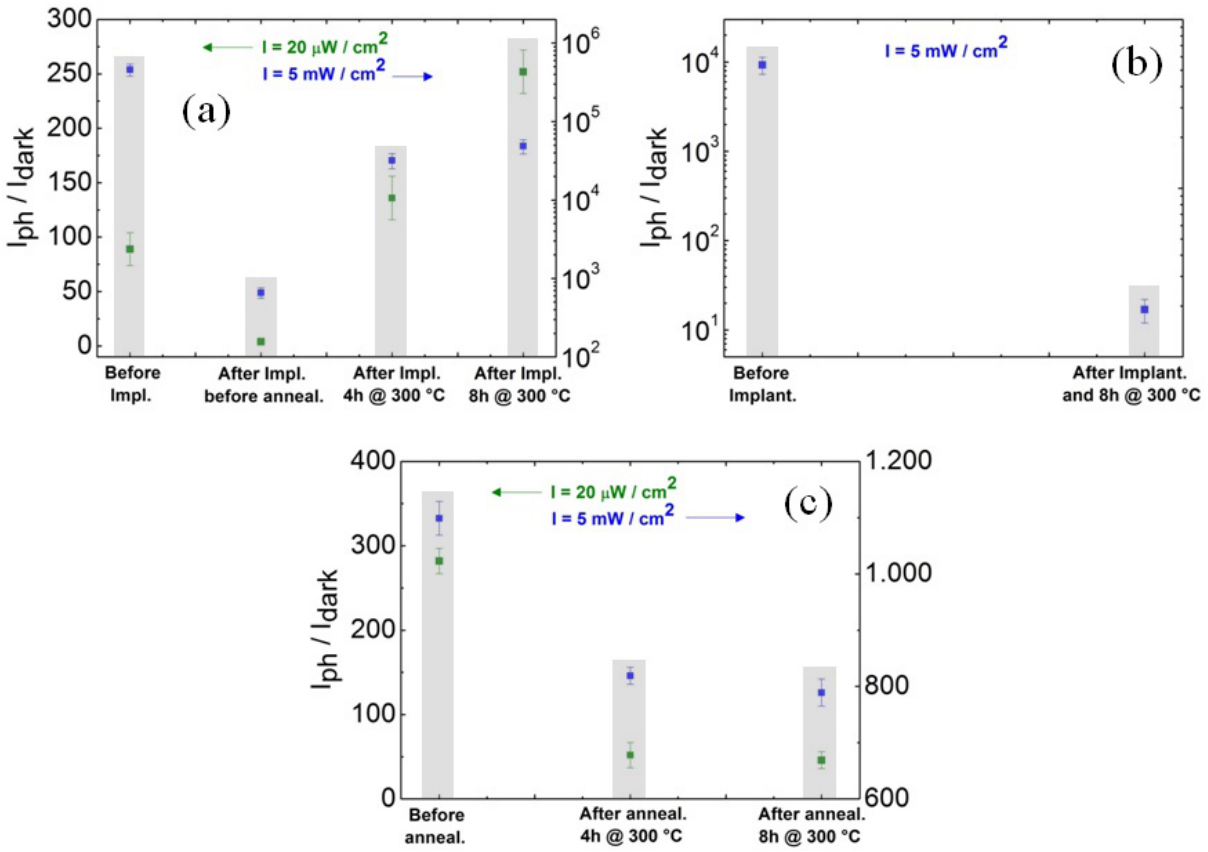

FIGURE 6.5: *UV Photosensitivity in aluminum (a) and argon implanted ZnO nanowires under steady state UV excitation at 20 μW/cm^2 and 5 mW/cm^2. The photosensitivity is measured immediately after implantation and following post-implantation annealing treatments. The photosensitivity is calculated as a ration between the photocurrent and the dark current, which were taken from table 6.1. The photosensitivity of a non implanted sample, which is used as a reference for the annealing procedures, is also reported.*

6.5.2 Persistent photoconductivity in Al doped ZnO nanowires

The dynamics of the persistent photoconductivity in aluminum implanted ZnO nanowires was investigated by measuring the photocurrent decay after UV illumination at various excitation intensity, ranging from 20 μW/cm^2 up to 5 mW/cm^2. The light excitation was keept on for 5 s and the decay was measured until the complete recovery of the original dark current. Similarly to the previous investigations presented in this chapter, analogous measurements were performed using the argon implanted as well as the reference samples.

A preliminary remark concerns the optimal method to accurately compare the photocurrent decay times in the investigated nanowires before and after doping or annealing. In fact, it has been shown in the previous section that such treatments drastically modify the photoresponse properties of the nanowires, leading to significantly different values

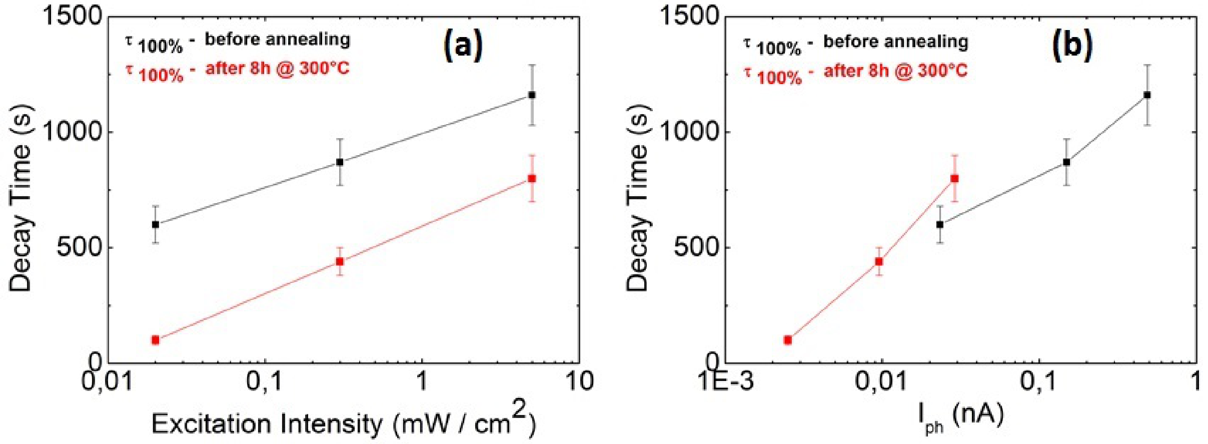

FIGURE 6.6: *Comparison of the photocurrent decay times of not-implanted ZnO nanowires before and after annealing at 300 °C for 8 hours. The decay times are plotted in (a) as a function of the excitation intensity and in (b) as a function of the corresponding generated photocurrent. The latter graph reveals that the decay times cannot be compared straightforwardly.*

of the photocurrent values in the untreated and treated samples. This fact complicates obviously the comparison of the photoconductivity decay in different samples, since even in the same sample the dynamics of the decay critically depends on the value of the generated photocurrent, as detailed described in section 5.2. As such, any treatment of the nanowires may impact the photoconductivity decay process through two distinct effects: by direct modification of the decay mechanisms, for instance by generating or suppressing charge carrier recombination channels, or indirectly by changing the photoresponse properties. It is therefore crucial to distinguish the latter from the former contribution, in order to avoid misleading or wrong intepretations of the experimental results. These may occur for instance when the photocurrent decay times are compared as a function of the excitation intensity, as shown for example in figure 6.6 (a) in case of the reference sample before and after thermal annealing. The graph clearly suggests that the relaxation of the photogenerated charge carriers proceeds much faster in the annealed sample. However, the eventual difference in photoresponse of the two samples is not taken into account. In order to circumnavigate this problem, a possible solution is to plot both decay times as a function of the generated photocurrent. Considering the previous example, the new graph in figure 6.6 (b) reveals instead that the comparison for this specific sample cannot be done straightforwardly, due to poor overlap of the generated photocurrents. Extrapolation of the experimental data can be therefore required, in order to meaningfully compare the photocurrent decay in different samples.

The analysis of the slow photoconductivity decay (PPC) in non-implanted ZnO nanowires, which was conducted in chapter 5, revealed that the decay process can be described in terms of two distinct components. The initial part of decay involves around 90 % of the photogenerated charge carriers and is caused by a pure surface effect, which consists in the adsorption-assisted trapping of electrons at the surface. The rest of the photocurrent decay is instead induced by different recombination mechanisms, which include in particular the trapping of holes at various bulk defect states. It is therefore reasonable to investigate the relaxation of photogenerated charge carriers in aluminum implantend ZnO nanowires, by individually analysing the mentioned components of the decay, in order to precisely evaluate the impact of the implantation on the corresponding recombination mechanisms.

The decay time related to the first component ($\tau_{90\%}$) in the aluminum implanted sample is compared in figure 6.7 (a) with that measured before implantation as a function of the generated photocurrent. For both sets of data, increasing values of the photocurrent correspond to increasing excitation power. To be rigorous, the decay times corresponding to the same excitation intensity cannot be individually compared, as the corresponding values of the photocurrent slighly differ. Nevertheless, since the ranges spanned by the generated photocurrent before and after implantation overlap for more than 2 orders of magnitude, it can be in general concluded that the the photoconductivity decay after implantation proceeds significantly slower than before. Similarly, also the remaining 10 % of photogenerated charge carriers recombine slower after aluminum implantation, as shown in figure 6.7 (b).

On the other hand, the thermal annealing alone does not affect substantially the dynamics of the photocurrent decay, as can be seen in figures 6.7 (c) and (d). Only at low excitation intensity a slight increase of $\tau_{90\%}$ by less than a factor of 2 is observed (figure 6.7 (d)), which is anyway negligible in comparison to the corresponding increase by few orders of magnitude observed in the aluminum implanted sample. In both graphs 6.7 (c) and 6.7 (d) the originally poor overlap of the photocurrent ranges was improved by adding experimetal data, which were obtained from a similar pristine sample under the same excitation conditions. No data from the argon implanted nanowires are instead reported, as the generated photocurrent was lower than the sensitivity as the SMU.

The performed analysis suggests thus that the drastic modification of the photoconductivity decay properties in aluminum implanted ZnO nanowires can be completely ascribed to the implantation process and not to the following post-implantation annealing treatment. The observed enhancement of the persistent photoconductivity indicates a prolongation

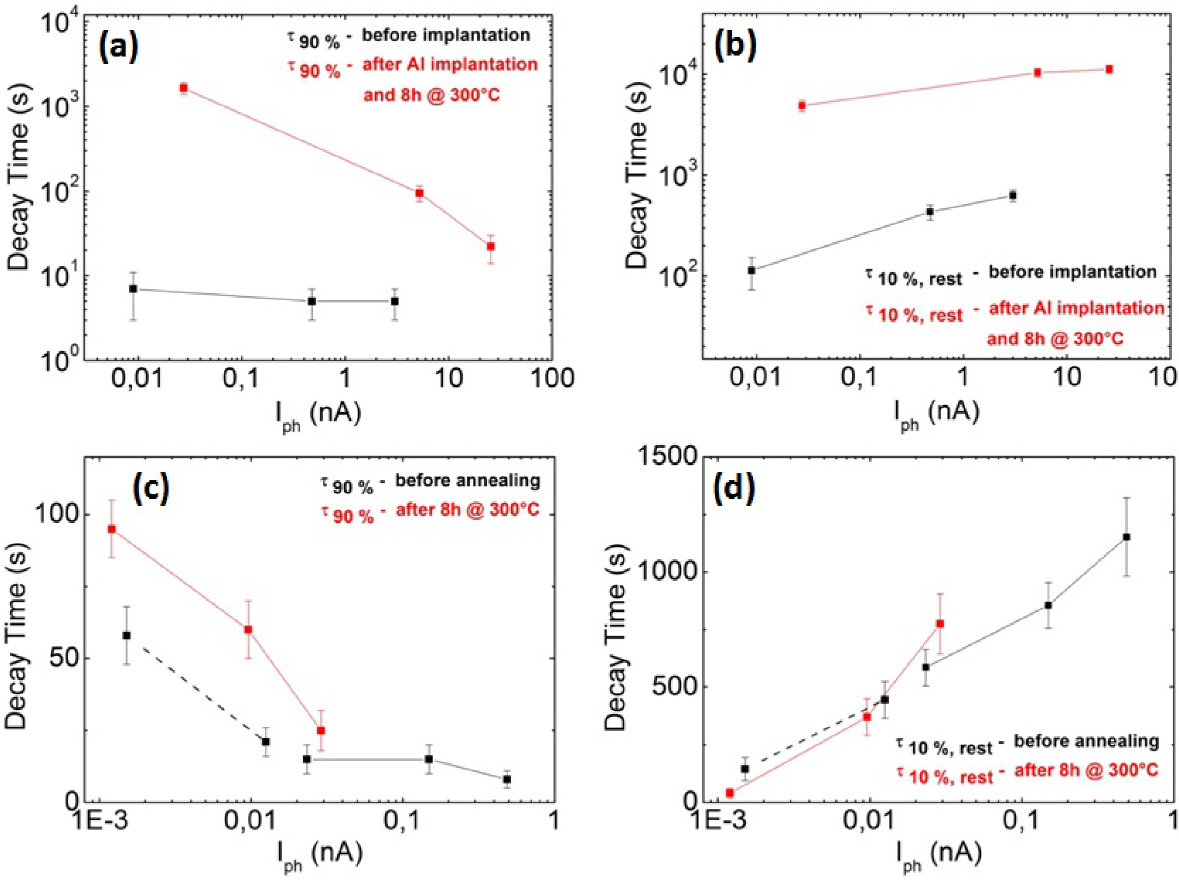

FIGURE 6.7: *Photocurrent decay times in contacted ZnO nanowires before and after aluminum implantation and following thermal annealing. The decay times corresponding to the initial 90 % of the decay are plotted in (a), while that related to the remaining 10 % are presented in (b). The analogous decay times in the sample used as a reference for the annealing procedure are shown respectively in (c) and (d). The experimental data connected by the dashed lines were obtained with a similar pristine sample.*

of the electron lifetime in conduction band with a corresponding reduction of the charge carrier recombination rate. In particular, the slowing down of the adsorption-assisted electron trapping may be caused by the enlargement of the surface depletion region (see also chapter 5) or the increase of the surface potential barrier, which hinder the penetration of electrons toward the trapping sites at the surface. Both the depletion region width and the surface barrier height depends explicitly on the electron density and on the density of occupid surface states (see equations 2.1 and 2.2). The increase of the electron density causes a reduction of both the depletion region width and the surface barrier height, while the increase of the density of occupied surface states determines their enlargement. As such, the enhancement of the n-type conductivity in ZnO by Al doping should in principle favor a faster electron trapping and a consequent reduction of the

PPC. However, the observed reduction of the electron trapping rate at the surface after Al implantation reveals a significant increase in the density of occupied surface states, which seems to dominate on the former counteracting effect. A possible explanation is based on the fact that the implantation process likely generates further surface states by sputtering [269, 275], which may cause the increase of the surface barrier height. Moreover, the generation of defect states may be also responsible for the slower charge carrier relaxation in the volume of the nanowire after implantation. The photoluminescence measurements presented in section 6.4 revealed the increased density of defect levels, which are involved in the DLE in ZnO nanowires. In particular, oxygen interstitial, which are responsible for the appearence of the red luminescence in the aluminum implanted sample, are known to act as hole trap centers [291]. As such, an enhancement of the hole trapping in the volume of the nanowire is likely to occur in aluminum implanted nanowires, leading to a reduction of the electron-hole recombination probability and to the observed prolongation of the photocurrent decay time.

6.6 Conclusions

In this chapter the thermal stability as well as the optical and above band-gap photoconductivity properties of argon and aluminum implanted ZnO nanowire devices have been investigated. Post-implantation annealing procedures were conducted, in order to reduce the density of point defects, which were generated during implantation. Despite the non complete recovery of the original crystal structure, electrical and optical characterizations revealed the successful activation of the aluminum ions as shallow donors in ZnO after thermal annealing at 300 °C for 8 hours. Steady state photoconductivity measurements were performed, in order to investigate the photoresponse properties in the implanted nanowires. Enhancement of the UV photosensivity after aluminum implantation has been observed at low excitation intensity and attributed to the photoexcitation of aluminum-related states. On the other hand, significant deterioration of the photoresponse properties has been observed in argon implanted nanowires, as well as in the non-implanted sample, which was used as a reference for the annealing procedure.

The dynamics of the photoconductivity decay has been investigated as a function of the excitation intensity, revealing a significant enhancement of the persistent photoconductivtiy in the aluminum implanted nanowires. The reduced rate of the adsorption-assisted electron trapping at the surface, which is responsible for the decay of 90 % of the photocurrent in non implanted ZnO nanowires, is attributed to the possible increase of the surface barrier height after implantation. Such effect is most likely caused by the generation of further surface states during implantation. Furthermore, the generation of defects in the volume of the nanowire has a strong impact on other bulk-related recombination channels. In particular, the increased concentration of oxygen interstitials, which is revealed by the photoluminescence measurements, leads to enhanced hole trapping processes. This determines a reduction of the electron-hole recombination probability and the observed enhancement of the persistent photoconductivity.

Chapter 7

Hydrogen sensing with ZnO nanowires

This chapter deals with the room temperature hydrogen sensing properties of contacted ZnO nanowires. The gas sensing mechanism in the pristine devices is investigated by comparing the dynamics of the device conductivity change upon interaction with hydrogen molecules and UV excitation. A corresponding model for the H_2/ZnO interaction is proposed. Plasma treatments in argon and oxygen atmospheres as well as thermal annealing procedures under oxygen flow are investigated as possible methods for the enhancement of the gas sensitivity. The sensing measurements on the argon plasma-treated devices were conducted in collaboration with Maximilian Zapf within the scope of his Bachelor thesis [292]. Ronny Nawrodt and Christian Schwarz assisted in performing the plasma treatments.

7.1 Motivation

The strong influence of the surrounding environment on the electrical properties of ZnO nanowires, which was investigated in chapter 5, makes such nanostructures excellent candidates for the develompment of a novel generation of miniaturized gas sensors with enhanced performances. The enhanced surface to volume ratio as well as the easy to specifically functionalize or modify the surface properties [293], are among the most remarkable features of ZnO nanowire based gas sensors. Further advantages of using ZnO nanowires for gas sensing applications as alternative to the correponding thin film technology include their superior stability [294], possible large-scale production [295] and considerable reduction in terms of power consumption [110, 111].

The pronounced sensitivity of ZnO nanowires toward a large variety of gas molecules has been proved by an exponentially growing number of publications during the last decade (see for example [35, 296–298]). In particular, there is increasing interest in the development of hydrogen gas sensors based on ZnO nanowires. Hydrogen is the most abundant element in nature and finds application in several industrial processes, such as oil and metal refining, food processing and electronics manufacturing [299]. Furthermore, it is considered as a potential source of clean energy [300]. However, hydrogen has a wide concentration window of flammability and, due to its extremely reduced weight, the greatest tendecy to leak among atomic and molecular species [301]. Therefore, the development of suitable and efficient hydrogen sensors is fundamental for the implementation of appropriate safety procedures.

Several types of hydrogen sensors based on ZnO nanowires have been demostrated, including in particular ZnO nanowire arrays and networks [302] and single nanowire devices [35, 140, 296]. Surface functionalization with noble metal nanoparticles is often considered, in order to enhance both gas sensitivity and selectivity [297, 303]. However, drastic lowering of the operation temperatures is highly desirable, since most of the gas sensors operate typically at few hundreds degrees Celsius [304], at which hydrogen may potentially become explosive [305]. Furthermore, the use of metallic nanoparticles as a functionalizing elements may be eventually deleterious for the electrical properties of ZnO nanowires, since it is known that metallic coatings on ZnO induce the formation of mid-gap states in the proximity of the surface, which can act as trap centers for charge carriers [92, 93]. Novel strategies must be therefore developed, in order to find alternative methods for enhancing the room temperature hydrogen sensitivity of ZnO nanowires.

Secondly, despite the extensive activity in reseach and development of such gas sensors, the understanding of the sensing mechanism is still quite poor [185]. Although it is typically believed that the detection occurs as a result of the interaction between hydrogen molecules in gas phase and adsorbed oxygen species on the ZnO surface [185], a convincing evidence for the occurrence of this process is still missing. This is mainly due to the lack of experimental techniques able to probe the dynamics of the detection process and to the fact that most of the computational studies do not include in the simulations the presence of adsorbed species on the nanowire surface. Additionally, even assuming that the hydrogen molecules interact effectively with the adsorbed oxygen species, it is also not know whether the hydrogen leave the surface after the interaction or gets irreversibly adsorbed. Furthermore, the occurrence of different detection mechanisms cannot be completely excluded. For instance, it is in principle possible that under dissociation of the hydrogen molecules at the surface, the atomic hydrogen components diffuse into the nanowire and act as a shallow donors, causing the increase of the sensor conductivity. This could occur in particular on reduced ZnO surfaces or after functionalization with noble metal nanoparticles, since in both conditions the molecular dissociation is favored [34, 107, 306].

Further investigations about the interaction mechanism between hydrogen molecules and ZnO nanowires are therefore highly required. Deeper understanding about the hydrogen detection mechanism is fundamental for the enhancement of several sensor parameters, such as sensitivity, selectivety as well as response and recovery speed. Furthermore, the development of an accurate model for the hydrogen sensing mechanism in ZnO nanowires could represent the basis for more sophisticated models describing the detection of more complex molecules.

7.2 Hydrogen sensing properties of untreated ZnO nanowire devices

Hydrogen sensing measurements with contacted ZnO nanowires were performed by measuring the change of the electrical conductivity in single ZnO nanowire devices upon interaction with hydrogen molecules. The measurements were performed at a pressure of 1 atm in a reference atmosphere of nitrogen flowing at 1000 sccm, by letting into the measuring chamber hydrogen from a formier gas supply at various flow values between 10 and 1000 sccm. Further details concerning the measurement setup and the experimental procedures, including the method for the calculation of the hydrogen sensitivity, are described in section 3.3.3.

As shown in Figure 7.1 (b), the conductivity of the devices increases as soon as hydrogen molecules are introduced in the chamber. After stopping the hydrogen flow, the conductivity starts to decay slowly. As soon as air is added to the nitrogen atmosphere, the decay speeds up significantly, until the current reaches the original reference value. The dependence of the gas sensitivity (see section 3.3.3) on the hydrogen concentration is presented in Figure 7.1 (a). The nanowires do not show any sensitivity toward hydrogen concentration lower than 500 ppm, which represents the threshold for a measurable change in the nanowire conductivity. Higher hydrogen concentration leads to an increase of the gas sensitivitiy, which tends progressively to saturate.

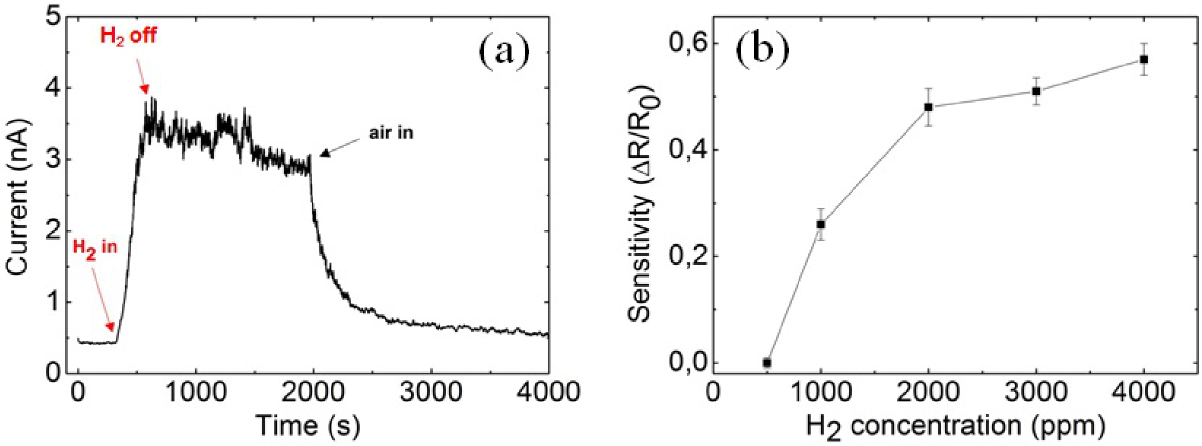

FIGURE 7.1: *Change of the conductivity in contacted ZnO nanowires when hydrogen flow is introduced in a reference nitrogen atmosphere (a). The conductivity decays slowly after stopping the hydrogen flow. Faster decay rate is observed as soon as air is introduced into the measuring chamber. The dependence of the gas sensitivity on the hydrogen concentration is shown in (b).*

The obtained results indicate that an electron transfer occurs from the hydrogen molecules into the conduction band of the nanowires. After stopping the hydrogen flow, the transferred electrons relax, as suggested by the observed decay of the condutivity. The conductivity decay is characterized by a remarkable dependence on the atmosphere conditions, being slow in the inert nitrogen atmosphere and faster in air. This behaviour resembles that already observed in similar samples after UV excitation, which was detailed investigated in section 5.1. This evidence suggests that the respective electron relaxation mechanism might be similar.

In order to corroborate this hyphotesis, the electron relaxation processes after hydrogen detection and UV excitation will be quantitatively compared in the following. For this purpose, a new sensing measurement was performed in a reference atmosphere containing air. Hydrogen flow was let into the chamber in concentration of 4000 ppm and kept on until saturation of the current. Air was considered as a reference atmosphere instead of nitrogen in order to speed up the recovery of the reference current after stopping the hydrogen flow. The photoconductivity measurement was carrier out in air under UV excitation intensity of 20 μW/cm^2. The UV excitation was kept on for the time sufficient to induce the same change of the current, which was observed upon interaction with hydrogen molecules. Under these conditions, the respective decay processes can be directly compared.

Both current decays are shown in figure 7.2, immediately after stopping respectively the

UV illumination and the hydrogen flow at t = 0 s. In both plots the reference and the dark currents have been subtracted. It can be observed that the decay rates are substantially equal until the current decays by 90 % of its maximum value. In chapter 5 it was proved that the UV illumination induces the desorption of oxygen species, which are typically adsorbed on the ZnO surface in equilibrium conditions. After light excitation, oxygen molecules tends to readsorb from the surrounding environment, trapping simultaneously photogenerated electrons and causing around 90 % of the photocurrent decay. The experimental evidence that this fraction of the current decay proceeds at the same rate after UV excitation as well as after hydrogen flow, suggests that also the majority of the electrons, which are transferred from the hydrogen molecules into the conduction band of the nanowire, relax after detection through the same adsorption-assisted trapping mechanism. This fundamental conclusion can be further exploited, in order to gain deeper insight about the interaction mechanism between hydrogen molecules and the nanowire surface. In fact, it has been observed that after stopping the hydrogen flow, the decay of the current in air proceeds until the original value of the reference current is recovered (Figure 7.1). This indicates that the density of oxygen adsorbed species at the end of the decay process and before introducing hydrogen in the chamber must be the same. In other terms, oxygen molecules tend to readsorb after stopping the hydrogen flow, in order to recover the coverage density of equilibrium conditions. Therefore, a reduction of the density of adsorbed oxygen species must occur during the interaction between hydrogen molecules and the nanowire surface. In the light of this conclusion, two possible alternative mechanisms for the interaction between hydrogen molecules and ZnO nanowires can be discussed:

1. hydrogen molecules simply remove adsorbed oxygen species from the adsorption sites and get there adsorbed (Figure 7.3 (a));
2. hydrogen molecules interact with adsorbed oxygen species, eventually forming water molecules, which desorb from the surface of the nanowire and leave unoccupied adsorption sites (Figure 7.3 (b)).

The former process has been proposed to occur in case of ethanol sensing with ZnO nanowires and is based on the different adsorption energies of ethanol and oxygen on ZnO [307]. Since the adsorption energy of the former is higher than that of the latter, it is likely that under ethanol flow the previously adsorbed oxygen molecules are removed from the surface and substituted at the adsorption sites by ethanol molecules. However, this process is unlikely to occur in case of hydrogen sensing, as the adsorption energy

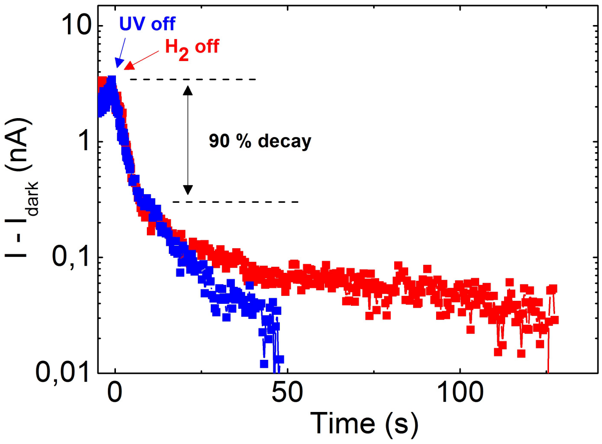

Figure 7.2: *Comparison of the current decays in contacted ZnO nanowires after stopping respectively the hydrogen flow and UV excitation in air atmosphere. The major part of the charge carriers (90 %) relax in both cases at the same rate, suggesting the occurrence of the same recombination mechanism.*

of hydrogen on ZnO is lower than that of oxygen [308–310]. Additionally, the eventual presence of nearly irreversibly adsorbed hydrogen species on the previous oxygen adsorption sites would change the dynamics of the following oxygen readsoprtion after stopping the hydrogen flow. However, this would be in contracdition with the evidence that the readsorption proceeds at the same rate also after UV excitation in absence of hydrogen in the surrounding atmosphere (figure 7.2). As such, the second proposed model is probably more realistic. The hydrogen sensing mechanism in ZnO nanowires can be therefore described in terms of injection of previously trapped electrons into the conduction band of ZnO, as a result of a chemical reaction between hydrogen molecules and oxygen adsorbed species.

7.3 Argon and oxygen plasma treatments

Since the detection of hydrogen molecules with ZnO nanowires results from a chemical reaction between hydrogen molecules in gas phase and adsorbed oxygen molecules, a change of the density of the latter species may drastically alter the hydrogen sensitivity of ZnO nanowire devices.

Plasma treatments are among the most effective methods for the modification of the surface properties of semiconductors [311]. In particular, plasma treatment in oxygen atmosphere has been proven to enhance the density of ionic oxygen related species, such as O_2^-, O^- and OH^-, on the ZnO surface [312]. Additionally, plasma treatments at typical

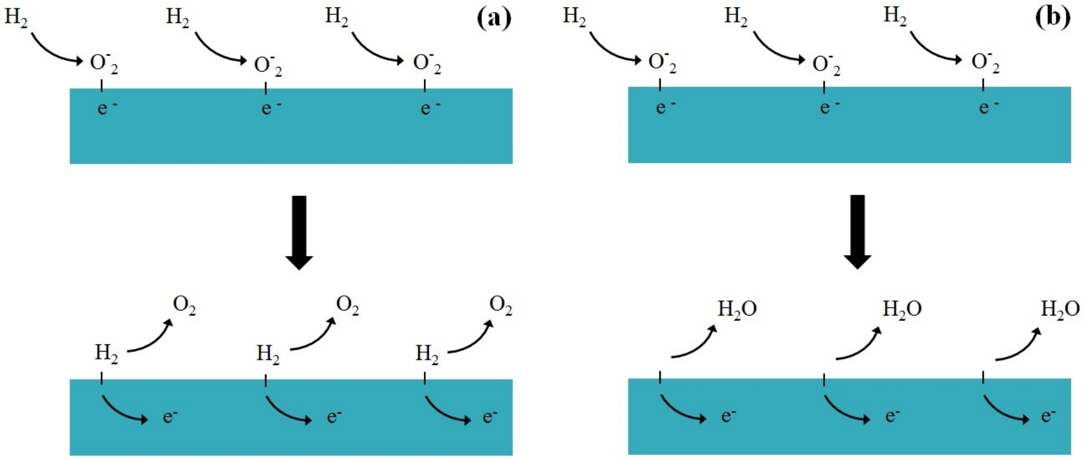

FIGURE 7.3: *Alternative models for the hydrogen sensing mechanism in contacted ZnO nanowires. The injection of electrons into the conduction band of the nanowire upon interaction with hydrogen molecules might result from the replacement of previously adsorbed oxygen molecules with hydrogen molecules at the adsorption sites (a) or from a chemical reaction with the adsorbed oxygen species, which generates desorbing water molecules (b). The latter model seems to be more realistic (see also text).*

power values of several tens of Watts may generate oxygen vacancies at the surface of ZnO nanowires as a result of the bombardment process [313, 314], since these have formation energy of around 2.8 eV [315]. It is under debate whether oxygen vancancies may act as preferential adsorption sites for oxygen molecules and more in general for other gas molecules. While some theoretical studies revealed an enhancement in the gas sensitivity [310, 316], some others [307] have shown that that the presence of oxygen vacancies on the nanowire surface lead to a reduced interaction between the ethanol molecules and the nanowire, leading consequently to a decrease of the gas sensitivity.

In addition to the plasma treatment in oxygen atmosphere, it is therefore interesting to consider the effect of plasma in argon, in order to separately investigate the influence of the ionic oxygen related species on the hydrogen sensing properties of ZnO nanowires, from that induced by the oxygen vacancies. For this purpose, single nanowire devices were selected and divided in two groups, which were treated either in argon or in oxygen atmosphere.

Since the litarature about the investigation of plasma treatments on ZnO nanowires for sensing applications is quite rare, low values of the plasma parameters were selected, in order to avoid the occurrence of significant sample degradation effects. For both atmospheres the gas flow and the chamber pressure were kept respectively at 50 sccm and 0.7 mbar. The lowest values for the plasma power and the treatment duration,

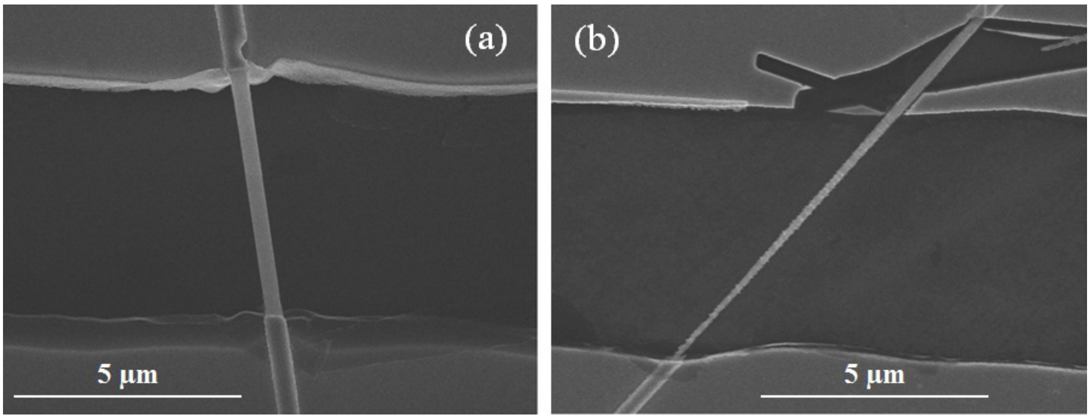

Figure 7.4: *SEM pictures of contacted ZnO nanowires several weeks after plasma treatments in oxygen (a) and argon atmospheres (b). The surface of the oxygen-treated nanowire is characterized only by slight roughness, while after plasma treatment in argon the roughness is more significant and a shrinking of the nanowire diameter can be observed.*

which could ensure sufficient operation stability of the plasma system, were respectively 30 W and 60 s. Scanning electron microscope pictures were taken a few weeks after the treatments, at the end of the electrical and gas sensing measurements. Two examples of treated nanowire devices are shown in figure 7.4. While the surface of the oxygen-treated nanowire is characterized by only slight roughness (figure 7.4 (a)), that of the argon-treated nanowire is significantly more rough (figure 7.4 (b)). In the latter case also a considerable shrinking of the nanowire diameter can be observed. This indicates a more significant occurrence of sputtering effects for the treatment in argon compared to that in oxygen, which is due to the heavier mass of argon. As such, the plasma treatment in argon atmosphere results more aggressive for ZnO nanowire devices.

The impact of the plasma treatments on the electrical properties of the nanowires is presented in figures 7.5 (a) and (b). An increase of the device conductivity is observed immediately after the treatment in argon. However, the induced change is not stable, as the conductivity is significantly reduced one week after the treatment. On the contrary, an initial deterioration of the I-V characteristics is observed immediately after plasma in oxygen, while the original conductivity is recovered after one week. A previous study about the photoluminescence properties of uncontacted ZnO nanowires [317] suggested that hydrogen atoms are eventually incorporated during plasma treatments in a contaminated argon atmosphere. Therefore, the temporary increase of the device conductivtiy observed after argon plasma can be attributed to the incoporated hydrogen atoms acting as shallow donors [49]. The decrease of the conductivtiy after one week is caused most

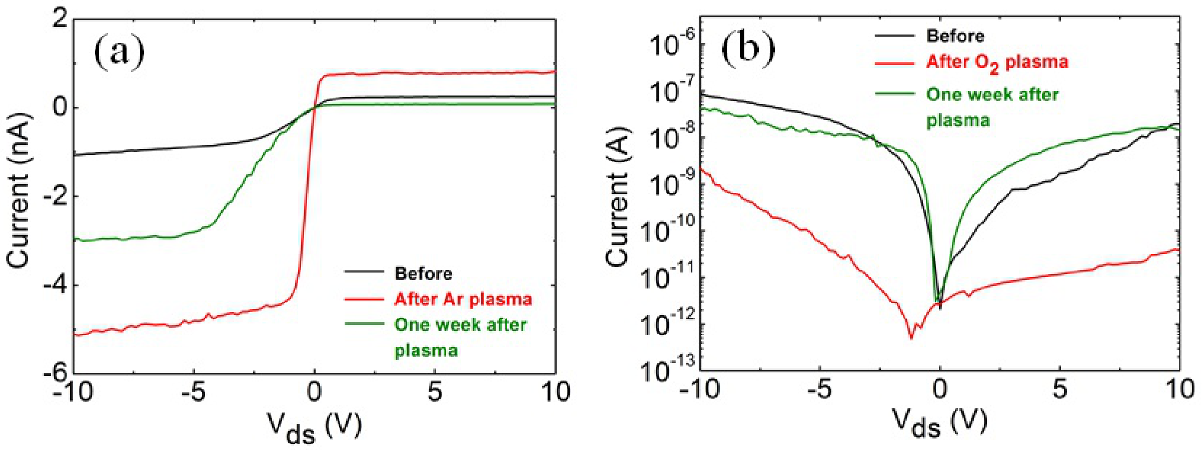

FIGURE 7.5: *I-V characteristics of contacted ZnO nanowires before and after plasma treatments in argon (a) and oxygen (b) atmospheres. Increased conductivity is observed immediately after plasma treatment in argon, which substantially reduces after one week. The treatment in oxygen induces a temporary degradation of the I-V characteristics, which are completely recovered after one week.*

likely by the progressive diffusion of hydrogen out of the nanowire due to its high mobility in ZnO [318]. The generation of oxygen vacancies at the surface during the treatment also occurs, as suggested by previous studies [313, 319] and by the increased roughness of the nanowire surface (figure 7.4). On the other hand, the temporary degradation of the I-V characteristics after the plasma treatment in oxygen atmosphere indicates the reduction of either the electron density or the electron mobility. Previous studies conducted on ZnO nanowire FETs revealed a positive shift of the threshold gate voltage after oxygen plasma [319], which clearly indicates that the reduction of the electron density is the dominant effect. This is most probably due to the increased density of oxygen related species on the surface of the nanowires after plasma treatment in oxygen atmosphere [312], which capture electrons from the conduction band of ZnO. Since these species are highly reactive, it is possible that they easily react with other molecules in air or leave the surface of the nanowire, releasing progressively the captured electrons back to the conduction band. This process may therefore lead to the observed recovery of the pristine conductivity one week after the treatment.

The sensing measurements with the plasma-treated devices were performed under hydrogen concentration of 4000 ppm in a nitrogen reference atmosphere. The hydrogen flow was kept on until the current saturates. As shown in figure 7.6, the gas sensitivity is drastically reduced immediately after both treatments. It is substantially recovered after one week only in the oxygen-treated devices, while it vanishes in the other samples.

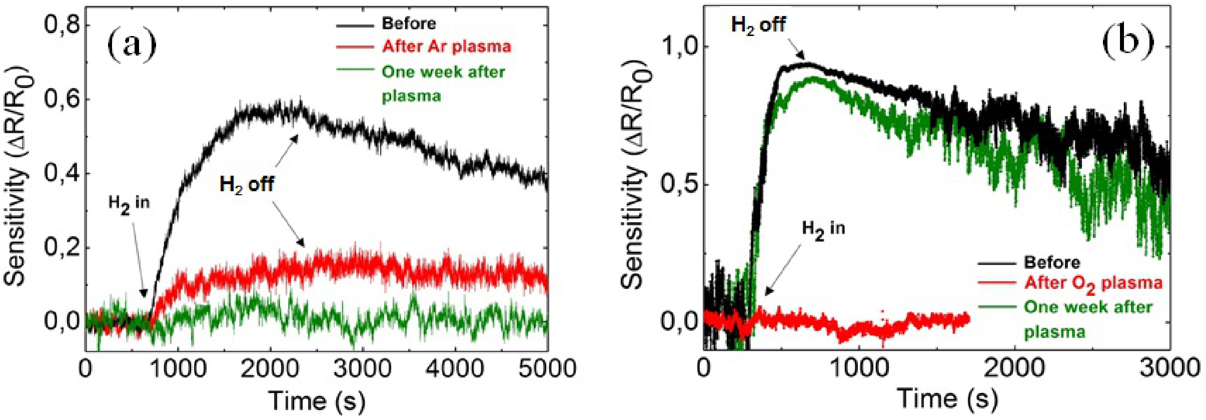

FIGURE 7.6: *Influence of plasma treatments in argon (a) and oxygen (b) atmospheres on the hydrogen sensitivity of contacted ZnO nanowires. Significant reduction of the sensitivity is observed immediately after both treatments. However, the pristine sensitivity is recovered in the oxygen-treated devices one week after the treatment.*

These results indicate that plasma treatments in argon and oxygen atmosphere have a deleterious impact on the hydrogen sensing properties of ZnO nanowires. The reason of the temporarly vanishing sensitivity immediately after plasma treatment in oxygen is not clear, as the specific interaction of the hydrogen molecules with the reactive species, which are introduced at the surface by the treatment, may differ from that with the simply adsorbed oxygen molecules (Figure 7.3). However, the recovery of the gas sensitivity one week after the treatment confirms that the ionic oxygen related species introduced by the treatment on the surface of the nanowires are particularly reactive and therefore not stable, as previously suggested by the analysis of the I-V characteristics. On the other hand, the progressive reduction of the hydrogen sensitivity after plasma in argon is most probably related to the generation of oxygen vacancies at the nanowire surface. Since such defects are highly unstable, it is expected they tend to be refilled by oxygen molecules from the surrounding environment. According to previous DFT calculations [306], the presence of oxygen vacancies at the ZnO surface induces the molecular dissociation of the adsorbing oxygen molecules, which bound at the surface with higher adsorption energy than on a clean surface. Therefore, in comparison to prior the plasma treatment in argon, these adsorbed oxygen atomic components may be more stable and less sensitive to the eventual chemical reaction with hydrogen molecules in gas phase. These results seem to confirm the prediction of previous studies [307], according to which defected ZnO surfaces show reduced gas sensitivity.

7.4 Annealing in oxygen atmosphere

Since plasma treatments in argon and oxygen atmospheres cause a reduction of the hydrogen sensitivity of ZnO nanowire devices, thermal annealing treatments in oxygen atmosphere were considered as an alternative method to enhance their gas sensitivity. Similarly to the plasma treatment in oxygen, also annealing procedures under oxygen flow increase typically the density of adsorbed oxygen species on the surface of ZnO nanowires [320, 321], which can potentially interact with hydrogen molecules in gas phase. However, the impact on the surface properties is expected to be milder in comparison to that induced by plasma treatments. Therefore, this shoud avoid the occurrence of sputtering and etching effects, which have been proven in the previous section to be deleterious for an effective detection of hydrogen molecules.

Annealing treatments were performed at various temperatures between 200 °C and 400 °C, under oxygen flow of 100 sccm and at a pressure of 1 atm. The devices were annealed for 2 hours, since it has been shown in chapter 6 that longer thermal treatments in air at similar temperatures lead to significant sample degradation effects.

The impact of the annealing treatments on the I-V characteristics of the investigated devices in shown in figure 7.7 (a). After thermal annealing at temperatures lower than 400 °C, the I-V characteristics remain substantially similar, while after treatment at 400 °C the samples are completely degradated. Since the profile of the curves remain sustantially unaltered, the annealing procedures at temperatures lower than 400 °C do not affect significantly the contact properties, which are responsible for the observed highly asymmetric profile of the I-V characteristics. Furthermore, it is unlikely to observe at these temperatures a drastic change of the defect concentration in the volume of the nanowires. It is instead more probable that the performed annealing treatments affect the properties of the nanowire surface. In principle, two possible processes can occur, namely enhanced adsorption of oxygen molecules and passivation of surface states. While the former causes a reduction of the conductivity, due to the trapping of electrons from the conduction band, the latter tends to increase it, by reducing charge carrier scattering effects at the surface. The observed results suggest that these two distinct effects substantially compensate each other, leading only to a slight change of the device conductivity.

Sensing measurements were initially performed at maximum hydrogen concentration of 4000 ppm in nitrogen, as previously did with the plasma-treated devices. The hydrogen flow was kept on until the current saturates. As shown in figure 7.7 (b), only after

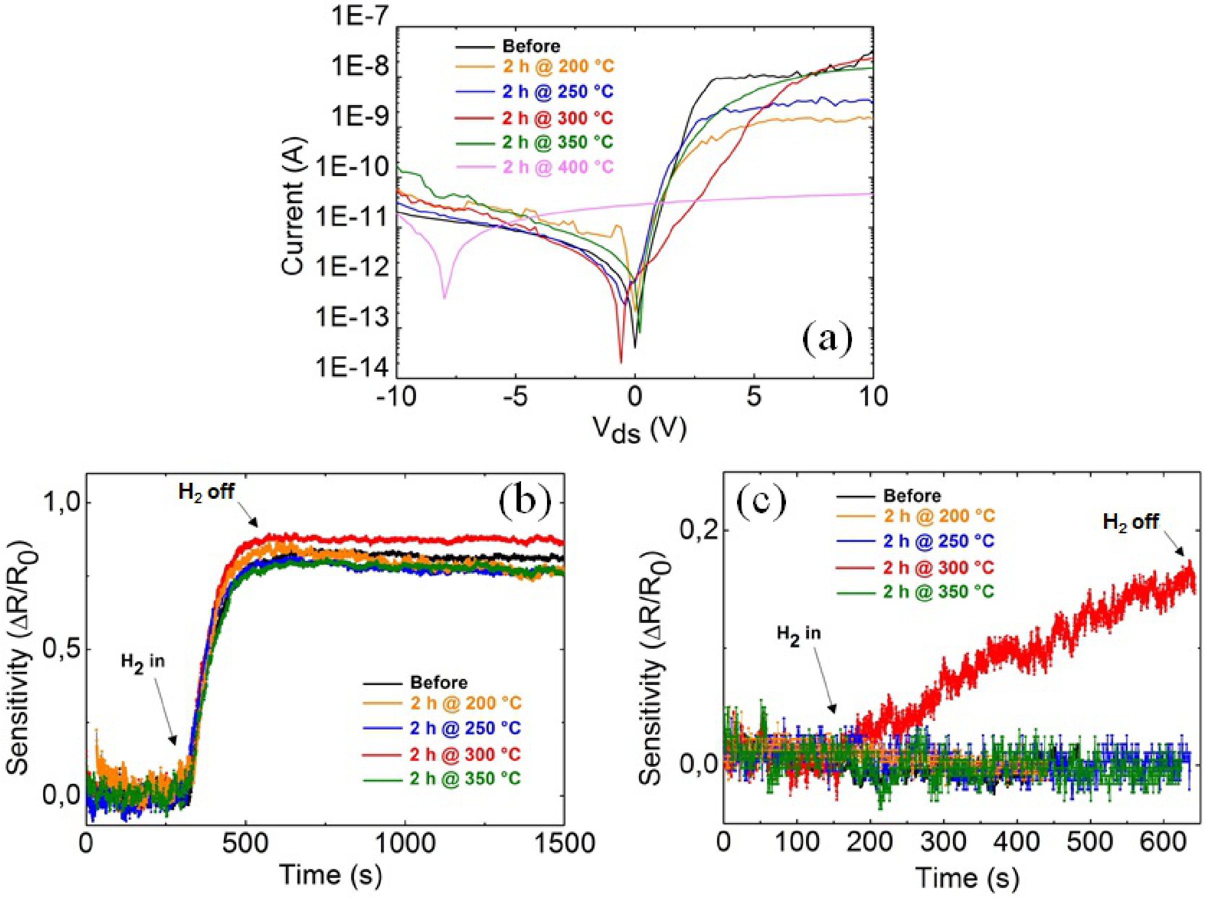

FIGURE 7.7: *I-V characteristics of contacted ZnO nanowires before and after thermal annealing of various duration in oxygen atmosphere (a). The annealing procedures do not change significantly the profile of the curves, indicating only a slight modification of the electrical properties of the nanowires below 400 °C. The influence of the treatments on the hydrogen sensing properties of the devices are shown in figure (b) and (c) at hydrogen concentration of respectively 4000 ppm and 500 ppm in a reference nitrogen atmopshere. The enhancement of the gas sensitivity is slight at high hydrogen concentration, while it is looks more significant at lower concentration.*

annealing at 300 °C the gas sensitivity is slighty higher than in the pristine devices. The hydrogen concentration was then reduced to 500 ppm, at which the interaction of hydrogen molecules with the investigated pristine devices is substantially undetectable (figure 7.1). While no enhancement of the gas sensitivity occurs after annealing at 200 °C and 250 °C, a measurable response of the devices to the hydrogen molecules up to a sensitivity of 0.17 is observed after annealing at 300 °C (figure 7.7 (c)). The sensitivity vanishes instead after further annealing at higher temperature.

The observed results can be described in terms of enhanced interaction between hydrogen molecules and the nanowire surface. Since thermal annealing in oxygen atmosphere leads to an increased density of adsorbed oxygen molecules on the surface of ZnO nanowires [320, 321], a higher density of sites for the interaction is most probably available after annealing. However, the enhancement of the hydrogen detection seems to be affected by the concentration of hydrogen molecules in the reference atmosphere. Indeed, since the pristine samples do not show any gas sensitivity at hydrogen concentration of 500 ppm, the sensitivity enhancement after annealing at 300 °C amounts at this gas concentration to around 0.17. However, the maximum sensitivity at hydrogen concentration of 4000 ppm increases from 0.83 before annealing up to 0.88 after the treatment, which amounts to a sensitivity enhancement of only 0.05. Two alternative explanations can be invoked, in order to explain such discrepancy. It is for instance possible that the surface modification, which is induced by the thermal annealing, affects the gas sensing process in a more pronounced way when the concentration of the gas to detect is low. In other terms, hydrogen molecules may feel more effectively the increased density of interaction sites when they surround the surface of the nanowire at low concentration. Alternatively, it might be that the enhanced interaction of hydrogen molecules with the surface, which leads to the injection of electrons from the surface into the conduction band (figure 7.3), is partially compensated by the simultaneous trapping of electrons from the conduction band toward the surface. In fact, as described in chapter 5 in regard to the photoconduction mechanism in ZnO nanowires, the progressive injection of electrons from the surface into the conduction band leads to a partial discharge of the surface and a consequent reduction of the surface band bending. This implies a reduction of the surface potential barrier, which electrons must overcome, in order to penetrate toward the surface and get there trapped. Thus, this process leads to a net reduction of the electron injection rate. The discharge of the surface during hydrogen sensing measurements is expected to be more pronounced at high hydrogen concentration, since a high density of electrons are injected into the conduction band. Therefore, the simultaneous counteracting trapping rate is expected to be higher than at low hydrogen concentration. This would results in the occurrence of the described compensation effect and in the observed lower enhancement of the gas sensitivity at high hydrogen concentration after thermal annealing in oxygen atmosphere.

In the light of the obtained results, thermal annealing in oxygen atmosphere can be considered as a promising method for enhancing the room temperature hydrogen sensitivity of ZnO nanowire devices, in contrast to plasma treatments in oxygen and argon atmospheres. The annealing procedure can be eventually further optimized, by exploring for instance different flow rate or annealing duration. Furthermore, the results support the prediction of previous theoretical studies, according to which clean ZnO surfaces show higher gas sensitivity than defected ones [307]. Mild treatments should be therefore preferred for the surface modification of ZnO nanowires in view of gas sensing applications.

7.5 Conclusions

In this chapter the room temperature hydrogen sensing properties of ZnO nanowire devices have been investigated. The detection of the hydrogen molecules in the gas phase is based on a measurable change of the device conductivity as soon as hydrogen in introduced in a reference nitrogen atmosphere. Gas sensitivity has been observed down to a hydrogen concentration of 500 ppm in pristine devices. A deeper insight about the gas sensing mechanism has been gained by comparing the dynamics of the conductivity relaxation after stopping the hydrogen flow with that observed after UV excitation, which was detailed investigated in chapter 5 and attributed to the adsorption-assisted trapping of electrons at the surface. The analysis revealed that the same recombination mechanism is effective also after interaction of the hydrogen molecules with the surface of the nanowires. This indicates that during the detection process, hydrogen molecules interact directly with previously adsorbed oxygen species. As a result of this chemical reaction, electrons are injected in the conduction band of the nanowire, inducing the observed increase of the device conductivity.

Plasma treatments in argon and oxygen atmospheres and thermal annealing in oxygen were then investigated as possible methods for enhancing the gas sensitivity of the nanowire devices. Both plasma treatments lead to a drastic reduction of the sensitivity, which is partially recovered one week after the treatment only in the oxygen-treated devices. Such instability of the gas sensitivity is probably due to the generation of highly reactive and unstable oxygen related species on the nanowire surface during the treatment in oxygen. The vanishing sensitivity after plasma treatment in argon can be instead attributed to the generation of surface defects and the increased roughness of the nanowire surface. On the one hand, thermal annealing in oxygen atmosphere has a milder impact on the investigated devices. Enhanced hydrogen sensitivity has been observed after annealing at 300 °C and attributed to the increased density of interaction sites for the hydrogen molecules at the surface of the nanowires.

Chapter 8

Summary and outlook

Owing to remarkable features, such as high surface sensitivity, wide band gap and intrinsic n-type conductivity, ZnO nanowires can be assembled as a semiconducting channel in miniaturized electric devices, which can be exploited as a novel generation of gas sensors and UV photodetectors with enhanced performances. However, the large-scale applicability of such devices is currently hindered by the limited control over their electrical properties. In particular, these can be strongly affected by the surrounding environment and by the presence of defects in the nanowire volume or in the proximity of contact or interface regions, whose effect is amplified by the high surface to volume ratio of such nanostructures. Furthermore, the specific modification of the device properties requires the optimization of various treatment procedures, whose impact on ZnO nanowire devices is still largely unexplored.

The work presented in this dissertation addresses the mentioned issues. The thesis is focused initially on the influence of defect levels and surrounding atmosphere on the photoconduction process in ZnO nanowire devices. The use of ion beam implantation for the n-type doping of the contacted nanowires is then discussed. Finally, the hydrogen sensing properties of pristine as well as plasma treated and annealed devices are investigated.

The influence of defect levels on the sub-bandgap photoconductivity properties has been investigated in ZnO nanowire based field-effect transistors, in which the population of photoactive defect levels can be controlled by the gate voltage. While the investigated devices do not show any photosensitivity in the spectral range from 400 to 800 nm at positive gate voltage, photoresponse is observed under negative gating. Photoluminescence measurements revealed that the variation of the gate voltage do not induce any substantial change of the defect population in the volume of the nanowires. The enhanced photoresponse under negative gating was then attributed to the photoexcitation of interfacial trap states, which are located at the interface between the nanowires and the gate oxide and are slowly populated under negative gate voltage. Additionally, the same levels are responsible for the occurrence of gating instability effects, which were observed in dark conditions.

The above band gap photoconductivity properties of contated ZnO nanowires has been investigated, focusing in particular on their dependence on the surrounding atmosphere. Larger photoresponse was observed in vacuum than under standard pressure conditions in inert atmosphere as well as in air. The rise of the conductivity under UV excitation is driven by the separation of photogenerated electron-hole pairs, which is caused by the upward surface band bending. Additionally, the migration of holes toward the surface induces the desorption of previously ionosorbed oxygen species. After stopping UV excitation around 90 % of the photoconductivity decay in air proceeds according to the so-called Elovich equation, which is typically used to quantitatively describe the adsorption kinetics of molecular species on semiconductor surfaces. This decay behavior indicates that around 90 % of the photogenerated electrons relax through trapping at the surface, assisted by the adsorption of oxygen molecules. The remaining photoconductivity decay is driven by different recombination mechanisms in the volume of the nanowire. Depending on the UV excitation intensity, the decay can last for several minutes or hours and the effect is known correspondingly as persistence of the photoconductivity.

The impact of the aluminum doping of ZnO nanowire devices by ion beam implantation on their electrical and photoconductivity properties has been then investigated. Since ion implantation generates typically defects in the implanted crystal, argon implantation was also performed on similar samples, in order to separately investigate the effect of the generated intrinsic defects. The successful activation of the aluminum atoms as shallow donors in ZnO nanowires was achieved after the optimized annealing procedure. Annealing of the pristine and the argon implanted samples under the same conditions leads instead to a significant degradation of the electrical properties, which is likely caused by the partial alloying of the ZnO nanowires with the electrodes. Therefore, despite the non complete recovery of the pristine crystal structure in the argon and aluminum implanted devices, which was proved by photoluminescence measurements, thermal treatments of longer duration or at higher temperature might be deleterious for the thermal stability of the devices. A drastic impact of the implantation process on the photoconductivity properties has been also observed. While a reduced UV photosensitivity has been measured after argon implantation, enhanced photoresponse has been observed in the aluminum implanted devices and attributed to the photoexcitation of aluminum-related states. Furthermore, the aluminum implantation affects the recombination of photogenerated charge carriers at the surface as well as in the volume of ZnO nanowires, leading to enhanced persistence of the photoconductivity. This effect has been attributed to the increased density of defect states in the implanted nanowires, which induce a more pronounced surface band bending and a reduced electron-hole recombination rate.

The final part of the thesis is dedicated to the investigation of the hydrogen sensing properties of ZnO nanowire devices at room temperature. The interaction of hydrogen molecules with the nanowire surface induces a measureable increase of the device conductivtity when hydrogen molecules are introduced into a reference environment in concentration higher than 500 ppm. Insight about the sensing mechanism was gained by comparing the dynamics of the conductivity decay after stopping the hydrogen flow with the persistent photonductivity after UV excitation. The analysis revealed that electrons are injected into the conduction band of the nanowires as a result of a chemical reaction between hydrogen molecules and the previoulsy ionosorbed oxygen species. Plasma treatments in argon and oxygen atmospheres, as well as thermal annealing in oxygen were then investigated as possible methods for enhancing the gas sensitivity of the nanowire devices. While both plasma treatments affect deleteriously the gas sensitivity, due to the increased roughness of the nanowire surface, thermal annealing in oxygen has a beneficial effect on the hydrogen detection process. This is attributed to the increased density of adsorbed oxygen species on the nanowire surface, which act as sites for the interaction between hydrogen molecules and the ZnO nanowire.

In summary, the results presented in this thesis provide new insights about the photoconductivity and gas sensing properties of ZnO nanowire based devices. The successful modulation of the sub-bandgap photoconductivity of ZnO nanowire field-effect transistors is particularly promising for the possible enlargement of the ZnO photosensitivity toward the visible and infrared spectral ranges. The photoexcitation efficiency of defect levels at the interface between the nanowire channel and the gate oxide could be eventually enhanced by specifically modifying the properties of the interface between the nanowire and the gate oxide.

The quantitative analysis of the photoconductivity relaxation after UV excitation in terms of the Elovich equation has been performed for the first time in case of ZnO nanostructures and provide a reliable physical description of the decay process, which overcomes the inadequacy of previous analysis approaches. As such, it could be further exploited in future also for the investigation of the persistent photoconductivity in other nanostructured material systems.

The successful aluminum implantation of ZnO nanowire devices has proved the efficiency of the ion beam implantation as a tool for the improvement of the electrical properties of such devices. The observed enhancement of the UV photoresponse after implantation is promising in view of possible applications of ZnO nanowires as building components for photodetectors. However, additional strategies should be in future adopted, in order to further reduce the density of generated defects. Since the investigated post-implantation annealing procedures present the mentioned limitations, performing implantation directly at higher temperature could represent an alternative solution.

Finally, a new insight into the hydrogen sensing mechanism in ZnO nanowire devices have been presented. The evidence that a significant part of the electron relaxation process in the nanowires after hydrogen detection can be modeled similarly to the electron relaxation after UV excitation, provides the opportunity to develop in future common strategies for both the reduction of the persistent photoconductivity in ZnO nanowire based photodetectors and the enhancement of the recovery speed of corresponding hydrogen sensors.

Bibliography

[1] I. Amato. The apostle of nanotechnology. *Science*, 254(5036):1310–1311, 1991.

[2] D. H. Freedman. Exploiting the nanotechnology of life. *Science*, 254(5036):1308–1310, 1991.

[3] Nanoscience and nanotechnologies: opportunities and uncertainties. *Royal Society*, 2004.

[4] K. Eric Drexler. Nanosystems: Molecular machinery, manufacturing, and computation. *Wiley*, 1992.

[5] M. Law, J. Goldberger, and P. Yang. Semiconductor nanowires and nanotubes. *Annual Review of Materials Research*, 34:83–122, 2004.

[6] D. D. D. Ma, C. S. Lee, F. C. K. Au, S. Y. Tong, and S. T. Lee. Small-diameter silicon nanowire surfaces. *Science*, 299(5614):1874–1877, 2003.

[7] D. Katz, T. Wizansky, O. Millo, E. Rothenberg, T. Mokari, and U. Banin. Size-dependent tunneling and optical spectroscopy of cdse quantum rods. *Physical Review Letters*, 89(8):086801–4, 2002.

[8] X. Zhao, C. M. Wei, L. Yang, and M. Y. Chou. Quantum confinement and electronic properties of silicon nanowires. *Physical Review Letters*, 92(23):236805–4, 2004.

[9] K. S. Yi, K. Trivedi, H. C. Floresca, H. Yuk, W. Hu, and M. J. Kim. Room-temperature quantum confinement effects in transport properties of ultrathin si nanowire field-effect transistors. *Nano Letters*, 11(12):5465–5470, 2011.

[10] L. Chen, T. Niebling, W. Heimbrodt, D. Stichtenoth, C. Ronning, and P. J. Klar. Dimensional dependence of the dynamics of the mn3d5 luminescence in (zn, mn)s nanowires and nanobelts. *Physical Review B*, 76(11):115325–7, 2011.

[11] B. Wu, A. Heidelberg, and J. J. Boland. Mechanical properties of ultrahigh-strength gold nanowires. *Nature Materials*, 4(7):525–529, 2005.

[12] R. Hillenbrand, T. Taubner, and F. Keilmann. Phonon-enhanced light–matter interaction at the nanometre scale. *Nature*, 418:159–162, 2002.

[13] C. M. Lieber. Semiconductor nanowires: A platform for nanoscience and nanotechnology. *MRS Bulletin*, 36(12):1052–1063, 2011.

[14] Z. Fan and J. G. Lu. Chemical sensing with zno nanowire field-effect transistor. *IEEE Transactions on Nanotechnology*, 5(4):393–396, 2006.

[15] S. Amdouni, Y. Coffinier, S. Szunerits, M. A. Zaïbi, M. Oueslati, and R. Boukherroub. Catalytic activity of silicon nanowires decorated with silver and copper nanoparticles. *Semiconductor Science and Technology*, 31(1):014011–8, 2015.

[16] Y. Xia, P. Yang, Y. Sun, Y. Wu, B. Mayers, B. Gates, Y. Yin, F. Kim, and H. Yan. One-dimensional nanostructures: Synthesis, characterization, and applications. *Advanced Materials*, 15(5):353–389, 2003.

[17] S. Luryi, J. Xu, and A. Zaslavsky (Eds). Future trends in microelectronics: The nano millennium. *Wiley-Interscience, New York*, 2002.

[18] X. Duan, Y. Huang, Y. Cui, J. Wang, and C. M. Lieber. Indium phosphide nanowires as building blocks for nanoscale electronic and optoelectronic devices. *Nature*, 409(6816):66–9, 2001.

[19] R. Yan, D. Gargas, and P. Yang. Nanowire photonics. *Nature Photonics*, 3(10): 569–576, 2009.

[20] W. Lu and C. M. Lieber. Semiconductor nanowires. *Journal of Physics D: Applied Physics*, 39(21):R387–R406, 2006.

[21] Y. Cui, Z. Zhong, D. Wang, W. U. Wang, and C. M. Lieber. High performance silicon nanowire field effect transistors. *Nano Letters*, 3(2):149–152, 2003.

[22] P. C. Chang and J. G. Lu. Zno nanowire field-effect transistors. *IEEE Transaction on Electron Devices*, 55(11):2977–2987, 2008.

[23] T. Voss, G. T. Svacha, E. Mazur, S. Müller, C. Ronning, D. Konjhodzic, and F. Marlow. High-order waveguide modes in zno nanowires. *Nano Letters*, 7(12): 3675–3680, 2007.

[24] R. Röder, M. Wille, S. Geburt, J. Rensberg, M. Zhang, J. G. Lu, F. Capasso, R. Buschlinger, U. Peschel, and C. Ronning. Continuous wave nanowire lasing. *Nano Letters*, 13(8):3602–3606, 2013.

[25] Z. L. Wang and J. Song. Piezoelectric nanogenerators based on zinc oxide nanowire array. *Science*, 312(5771):242–246, 2006.

[26] K. K. Korir, G. Cicero, and A. Catellani. Piezoelectric properties of zinc oxide nanowires: an ab initio study. *Nanotechnology*, 24(47):475401–5, 2013.

[27] X. Chen, C. K. Y. Wong, C. A. Yuan, and G. Zhang. Nanowire-based gas sensors. *Sensors and Actuators B: Chemical*, 177:178–195, 2013.

[28] F. Patolsky, G. Zheng, and C. M. Lieber. Nanowire sensors for medicine and the life sciences. *Nanomedicine*, 1(1):51–65, 2006.

[29] G. Shen, P. C. Chen, K. Ryu, and C. Zhou. Devices and chemical sensing applications of metal oxide nanowires. *Journal of Materials Chemistry*, 19(7):828–839, 2009.

[30] E. Comini, C. Baratto, G. Faglia, M. Ferroni, A. Ponzoni, D. Zappa, and G. Sberveglieri. Metal oxide nanowire chemical and biochemical sensors. *Journal of Materials Research*, 28(21):2911–2931, 2013.

[31] A. Janotti and C. G. Van de Walle. Fundamentals of zinc oxide as a semiconductor. *Reports on Progress in Physics*, 72(12):126501–29, 2009.

[32] C. Soci, A. Zhang, B. Xiang, S. A. Dayeh, D. P. R. Aplin, J. Park, X. Y. Bao, Y. H. Lo, and D. Wang. Zno nanowire uv photodetectors with high internal gain. *Nano Letters*, 7(4):1003–1009, 2007.

[33] Z. Fan and J. G. Lu. Gate-refreshable nanowire chemical sensors. *Applied Physics Letters*, 86(12):123510–3, 2005.

[34] T. J. Hsueh and S. J. Chang. Highly sensitive zno nanowire ethanol sensor with pd adsorption. *Applied Physics Letters*, 91(5):053111–3, 2007.

[35] O. Lupan, V. V. Ursaki, G. Chai, L. Chow, G. A. Emelchenko, I. M. Tiginyanu, A. N. Gruzintsev, and A. N. Redkin. Selective hydrogen gas nanosensor using individual zno nanowire with fast response at room temperature. *Sensors and Actuators B: Chemical*, 144(1):56–66, 2010.

[36] R. Niepelt, U. C. Schröder, J. Sommerfeld, I. Slowik, B. Rudolph, R. Möller, B. Seise, A. Csaki, W. Fritzsche, and C. Ronning. Biofunctionalization of zinc oxide nanowires for dna sensory applications. *Nanoscale Research Letters*, 6(511): 1–7, 2011.

[37] J. Bao, I. Shalish, Z. Su, R. Gurwitz, F. Capasso, X. Wang, and Z. Ren. Photoinduced oxygen release and persistent photoconductivity in zno nanowires. *Nanoscale Research Letters*, 6(404):1–7, 2011.

[38] S. Hullavarad, N. Hullavarad, D. Look, and B. Claflin. Persistent photoconductivity studies in nanostructured zno uv sensors. *Nanoscale Research Letters*, 4(12):1421–1427, 2009.

[39] D. Cammi and C. Ronning. Persistent photoconductivity in zno nanowires in different atmospheres. *Advances in Condensed Matter Physics*, 2014(Article ID 184120), 2014.

[40] C. Klingshirn, J. Fallert, H. Zhou, J. Sartor, C. Thielea, F. Maier-Flaig, D. Schneider, and H. Kalt. 65 years of zno research – old and very recent results. *Physica Status Solidi B*, 247(6):1424–1447, 2010.

[41] D. C. Look, D. C. Reynolds, J. R. Sizelove, R. L. Jones, C. W. Litton, G. Cantwell, and W. C. Harsch. Electrical properties of bulk zno. *Solid State Communications*, 105(6):399–401, 1998.

[42] K. Maeda, M. Sato, I. Niikura, and T. Fukuda. Growth of 2 inch zno bulk single crystal by the hydrothermal method. *Semiconductor Science and Technology*, 20 (4):S49–S54, 2005.

[43] C. Neumann, S. Lautenschläger, S. Graubner, J. Sann, N. Volbers, B. K. Meyer, J. Bläsing, A. Krost, F. Bertram, and J. Christen. Homoepitaxy of zno: from the substrates to doping. *Physica Status Solidi B*, 244(5):1451–1457, 2007.

[44] T. Ive, T. Ben-Yaacov, A. Murai, H. Asamizu, C. G Van de Walle, U. Mishra, S. P. Den Baars, and J. S. Speck. Metalorganic chemical vapor deposition of zno(0001) thin films on gan(0001) templates and zno(0001) substrates. *Physica Status Solidi C*, 5(9):3091–3094, 2008.

[45] Z. L. Wang. Zinc oxide nanostructures: growth, properties and applications. *Journal of Physics: Condensed Matter*, 16(25):R829–R858, 2004.

[46] A. Mang, K. Reimann, and St. Ruebenacke. Band gaps, crystal-field splitting, spin-orbit coupling, and exciton binding energies in zno under hydrostatic pressure. *Solid State Communications*, 94(4):251–254, 1995.

[47] H. Morkoç and Ü. Özgür. Zinc oxide: Fundamentals, materials and device technology. *WILEY-VCH Verlag GmbH & Co. KGaA, Weinheim*, 2009.

[48] C. G. Van de Walle. Hydrogen as a cause of doping in zinc oxide. *Physical Review Letters*, 85(5):1012–1015, 2000.

[49] A. Janotti and C. G. Van de Walle. Hydrogen multicenter bonds. *Nature Materials*, 6(1):44–47, 2007.

[50] F. Gallino, G. Pacchioni, and C. Di Valentin. Transition levels of defect centers in zno by hybrid functionals and localized basis set approach. *The Journal of Chemical Physics*, 133(14):144512–10, 2010.

[51] A. Catellani, A. Ruini, G. Cicero, and A. Calzolari. First principles description of the electronic properties of doped zno. *Physica Status Solidi B*, 250(10):2106–2109, 2013.

[52] D. M. Hofmann, A. Hofstätter, F. Leiter, H. Zhou, F. Henecker, B. K. Meyer, S. B. Orlinskii, J. Schmidt, and P. G. Baranov. Hydrogen: a relevant shallow donor in zinc oxide. *Physical Review Letters*, 88(4):045504–4, 2002.

[53] H. Qiu, B. Meyer, Y. Wang, and C. Wöll. Ionization energies of shallow donor states in zno created by reversible formation and depletion of h interstitials. *Physical Review Letters*, 101(23):236401–4, 2008.

[54] E. V. Lavrov, F. Herklotz, and J. Weber. Identification of two hydrogen donors in zno. *Physical Review B*, 79(16):165210–13, 2009.

[55] A. Janotti and C. G. Van de Walle. Oxygen vacancies in zno. *Applied Physics Letters*, 87(12):122102–3, 2005.

[56] A. Janotti and C. G. Van de Walle. New insight into the role of native point defects in zno. *Journal of Crystal Growth*, 287(1):58–65, 2006.

[57] S. Heinze, A. Krtschil, J. Bläsing, T. Hempel, P. Veit, A. Dadgar, J. Christen, and A. Krost. Homoepitaxial growth of zno by metalorganic vapor phase epitaxy in two-dimensional growth mode. *Journal of Crystal Growth*, 308(1):170–175, 2007.

[58] A. Dadgar, N. Oleynik, J. Bläsing, S. Deiter, D. Forster, F. Bertram, A. Diez, M. Seip, A. Greiling, J. Christen, and A. Krost. Heteroepitaxy and nitrogen doping of high-quality zno. *Journal of Crystal Growth*, 272(1-4):800–804, 2004.

[59] T. Ive, T. Ben-Yaacov, C. G. Van de Walle, U. K. Mishra, S. P. DenBaars, and J. S. Speck. Step-flow growth of zno(0 0 0 1) on gan(0 0 0 1) by metalorganic chemical vapor epitaxy. *Journal of Crystal Growth*, 310(15):3407–3412, 2008.

[60] T. Ive, T. Ben-Yaacov, A. Murai, H. Asamizu, C. G. Van de Walle, U. Mishra, S. P. DenBaars, and J. S. Speck. Metalorganic chemical vapor deposition of zno(0001) thin films on gan(0001) templates and zno(0001) substrates. *physica status solidi (c)*, 5(9):3091–3094, 2008.

[61] S. Graubner, C. Neumann, N. Volbers, B. K. Meyer, J. Bläsing, and A. Krost. Preparation of zno substrates for epitaxy: Structural, surface, and electrical properties. *Applied Physics Letters*, 90(4):042103–3, 2007.

[62] A. Tsukazaki, A. Ohtomo, S. Yoshida, M. Kawasaki, C. H. Chia, T. Makino, Y. Segawa, T. Koida, S. F. Chichibu, and H. Koinuma. Layer-by-layer growth of high-optical-quality zno film on atomically smooth and lattice relaxed zno buffer layer. *Applied Physics Letters*, 83(14):2784–2786, 2003.

[63] E. L. Dereniak and D. G. Crowe. Optical radiation detectors. *Wiley Series in Pure and Applied Optics, 1st Edition*, 1984.

[64] Ü. Özgür, D. Hofstetter, and H. Morkoç. Zno devices and applications: a review of current status and future prospects. *Proceedings of the IEEE*, 98(7):1255–1268, 2010.

[65] Y. S. Choi, J. W. Kang, D. K. Hwang, and S. J. Park. Recent advances in zno-based light emitting diodes. *IEEE Transactions on Electron Devices*, 57(1):26–41, 2010.

[66] V. A. Karpina, V. I. Lazorenko, C. V. Lashkarev, V. D. Dobrowolski, L. I. Kopylova, V. A. Baturin, S. A. Pustovoytov, A. J. Karpenko, S. A. Eremin, P. M. Lytvyn, V. P. Ovsyannikov, and E. A. Mazurenko. Zinc oxide – analogue of gan with new perspective possibilities. *Crystal Research and Technology*, 39(11):980–992, 2004.

[67] R. Hoffman. Zno thin film transistors. *Zinc Oxide Bulk, Thin Films and Nanostructures: processing, Properties and Applications*, pages 415–442, C. Jagadish and S. J. Pearton, Elsevier, 2006.

[68] J. Nishii, F. M. Hossain, S. Takagi, T. Aita, K. Saikusa, Y. Ohmaki, I. Ohkubo, S. Kishimoto, A. Ohtomo, T. Fukumura, F. Matsukura, Y. Ohno, H. Koinuma, H. Ohno, and M. Kawasaki. High mobility thin film transistors with transparent zno channels. *Japanese Journal of Applied Physics*, 42(Part 2, Number 4A):L347–L349, 2003.

[69] D. J. Rogers, F. H. Teherani, V. E. Sandana, and M. Razeghi. Zno thin films & nanostructures for emerging optoelectronic applications. *Proceedings of SPIE*, 7605 (Part 2, Number 4A):76050K–11, 2010.

[70] Y. Liu, Y. Li, and H. Zeng. Zno-based transparent conductive thin films: doping, performance and processing. *Journal of Nanomaterials*, 2013(Article ID 196521), 2013.

[71] Y. Liu, C. R. Gorla, S. Liang, N. Emanetoglu, Y. Lu, H. Shen, and M. Wraback. Ultraviolet detectors based on epitaxial zno films grown by mocvd. *Journal of Electronic Materials*, 29(1):69–74, 2000.

[72] Ü. Özgür, Ya. I. Alivov, C. Liu, A. Teke, M. A. Reshchikov, S. Doğan, V. Avrutin, S.-J. Cho, and H. Morkoç. A comprehensive review of zno materials and devices. *Journal of Applied Physics*, 98(4):041301–103, 2005.

[73] C. Ronning, P. X. Gao, Y. Ding, Z. L. Wang, and D. Schwen. Manganese-doped zno nanobelts for spintronics. *Applied Physics Letters*, 84(5):783–785, 2004.

[74] D. C. Reynolds, C. W. Litton, D. C. Look, J. E. Hoelscher, B. Claflin, T. C. Collins, J. Nause, and B. Nemeth. High-quality, melt-grown zno single crystals. *Journal of Applied Physics*, 95(9):4802–4805, 2004.

[75] H. K. Ardakani. Electrical conductivity of in situ “hydrogen-reduced” and structural properties of zinc oxide thin films deposited in different ambients by pulsed excimer laser ablation. *Thin Solid Films*, 207(1-2):280–283, 1996.

[76] F. Quaranta, A. Valentini, F. R. Rizzi, and G. Casamassima. Dual-ion-beam sputter deposition of zno films. *Journal of Applied Physics*, 74(1):244–248, 1993.

[77] K. Kobayashi, T. Matsubara, S. Matsushima, S. Shirakata, S. Isomura, and G. Okada. Preparation of c-axis oriented zno films by low-pressure organometallic chemical vapor deposition. *Thin Solid Films*, 266(2):106–109, 1995.

[78] M. A. L. Johnson, S. Fujita, W. H. Rowland Jr., W. C. Hughes, J. W. Cook Jr., and J. F. Schetzina. Mbe growth and properties of zno on sapphire and sic substrates. *Thin Solid Films*, 25(12):855–862, 1996.

[79] R. J. Lad, P. D. Funkenbusch, and C. R. Aita. Postdeposition annealing behavior of rf sputtered zno films. *Journal of Vacuum Science and & Technology*, 17(4): 808–811, 1980.

[80] W.-C. Shih and M.-S. Wu. Growth of zno films on gaas substrates with a sio2 buffer layer by rf planar magnetron sputtering for surface acoustic wave applications. *Journal of Crystal Growth*, 137(3-4):319–325, 1994.

[81] R. S. Wagner and W. C. Ellis. Vapor-liquid-solid mechanism of single crystal growth. *Applied Physics Letters*, 4(5):89–90, 1964.

[82] H. Simon, T. Krekeler, G. Schaan, and W. Mader. Metal-seeded growth mechanism of zno nanowires. *Crystal Growth & Design*, 13(2):572–580, 2012.

[83] M. Wei, D. Zhi, and J. L. MacManus-Driscoll. Self-catalysed growth of zinc oxide nanowires. *Nanotechnology*, 16(8):1364–1368, 2005.

[84] S. Xu and Z. L. Wang. One-dimensional zno nanostructures: Solution growth and functional properties. *Nano Research*, 4(11):1013–1098, 2011.

[85] L. Wischmeier, T. Voss, S. Börner, and W. Schade. Comparison of the optical properties of as-grown ensembles and single zno nanowires. *Applied Physics A*, 84 (1-2):111–116, 2006.

[86] J. Goldberger, D. J. Sirbuly, M. Law, and P Yang. Zno nanowire transistors. *The Journal of Physical Chemistry B*, 109(1):9–14, 2004.

[87] S. Haffad, G. Cicero, and M. Samah. Structural and electronic properties of zno nanowires: a theoretical study. *Energy Procedia*, 10:128–137, 2011.

[88] Y. Gu, I. L. Kuskovsky, M. Yin, S. O'Brien, and G. F. Neumark. Quantum confinement in zno nanorods. *Applied Physics Letters*, 85(17):3833–3833, 2004.

[89] D. Stichtenoth, C. Ronning, T. Niermann, L. Wischmeier, T. Voss, C.-J. Chien, P.-C. Chang, and J. G. Lu. Optical size effects in ultrathin zno nanowires. *Nanotechnology*, 18(43):435701–5, 2007.

[90] R. T. Senger and K. K. Bajaj. Optical properties of confined polaronic excitons in spherical ionic quantum dots. *Physical Review B*, 68(4):045313–8, 2003.

[91] J. P. Richters, T. Voss, L. Wischmeier, I. Rückmann, and J. Gutowski. Influence of polymer coating on the low-temperature photoluminescence properties of zno nanowires. *Applied Physics Letters*, 92(1):011103–4, 2008.

[92] J. P. Richters, A. Dev, S. Müller, R. Niepelt, C. Borschel, C. Ronning, and T. Voss. Influence of metallic coatings on the photoluminescence properties of zno nanowires. *Physica Status Solidi (RRL) – Rapid Research Letters*, 3(5):166–168, 2009.

[93] D. Yufeng and L. J. Brillson. First-principles studies of metal (111)/zno0001 interfaces. *Journal of Electronic Materials*, 37(5):743–748, 2008.

[94] Z. Fan, D. Wang, P. C. Chang, W. Y. Tseng, and J. G. Lu. Zno nanowire field-effect transistor and oxygen sensing property. *Applied Physics Letters*, 85(24):5923–5925, 2004.

[95] W. I. Park, J. S. Kim, G. C. Yi, M. H. Bae, and H.-J. Lee. Fabrication and electrical characteristics of high-performance zno nanorod field-effect transistors. *Applied Physics Letters*, 85(21):5052–5054, 2004.

[96] P.-C. Chang, Z. Fan, C.-J. Chien, D. Stichtenoth, C. Ronning, and J. C. Lu. High-performance zno nanowire field effect transistors. *Applied Physics Letters*, 89(13): 133113–3, 2006.

[97] A. Soudi, P. Dhakal, and Y. Gu. Diameter dependence of the minority carrier diffusion length in individual zno nanowires. *Applied Physics Letters*, 96(25):253115–3, 2010.

[98] F. M. Hossain, J. Nishii, S. Takagi, T. Sugihara, A. Ohtomo, T. Fukumura, H. Koinuma, H. Ohnoc, and M. Kawasaki. Modeling of grain boundary barrier modulation in zno invisible thin film transistors. *Physica E: Low-dimensional Systems and Nanostructures*, 21(2-4):911–915, 2004.

[99] R. L Hoffman, B. J. Norris, and J. F. Wager. Zno-based transparent thin-film transistors. *Applied Physics Letters*, 82(5):733–735, 2003.

[100] S. Song, W.-K. Hong, S.-S. Kwon, and T. Lee. Passivation effects on zno nanowire field effect transistors under oxygen, ambient, and vacuum environments. *Applied Physics Letters*, 92(26):263109–3, 2008.

[101] C. Han, D. Xiang, M. Zheng, J. Lin, J. Zhong, C. Haur Sow, and W. Chen. Tuning the electronic properties of zno nanowire field effect transistors via surface functionalization. *Nanotechnology*, 26(9):095202–6, 2015.

[102] N. M. J. Ditshego, K. Sun, I. Zeimpekis, P. Ashburn, M. R. R. de Planque, and H. M. H. Chong. Effects of surface passivation on top-down zno nanowire transistors. *Microelectronic Engineering*, 145:91–95, 2015.

[103] W.-K. Hong, S. Song, D.-K. Hwang, S.-S. Kwon, G. Jo, S.-J. Park, and T. Lee. Effects of surface roughness on the electrical characteristics of zno nanowire field effect transistors. *Applied Surface Science*, 254(23):7559–7564, 2008.

[104] S. Choopun, N. Hongsith, and E. Wongrat. Metal-oxide nanowires for gas sensors. *Nanowires - Recent Advances, Prof. Xihong Peng (Ed.)*, 2012.

[105] A. Choi, K. Kim, H.-Il Jung, and S. Y. Lee. Zno nanowire biosensors for detection of biomolecular interactions in enhancement mode. *Sensors and Actuators B: Chemical*, 148(2):577–582, 2010.

[106] E. Oh, H.-Y. Choi, S.-H. Jung, S. Cho, J. C. Kim, K.-H. Lee, S.-W. Kang, J. Kim, J.-Y. Yun, and S.-H. Jeong. High-performance no2 gas sensor based on zno nanorod grown by ultrasonic irradiation. *Sensors and Actuators B: Chemical*, 141(1):239–243, 2009.

[107] T. A. Baker, X. Liu, and C. M. Friend. The mystery of gold's chemical activity: local bonding, morphology and reactivity of atomic oxygen. *Physical Chemistry Chemical Physics*, 13(1):34–46, 2011.

[108] C. Baratto, E. Comini, G. Faglia, G. Sberveglieri, M. Zha, and A. Zappettini. Metal oxide nanocrystals for gas sensing. *Sensors and Actuators B: Chemical*, 109(1):2–6, 2005.

[109] E. Comini and G. Sberveglieri. Metal oxide nanowires as chemical sensors. *materialstoday*, 13(7-8):36–44, 2010.

[110] E. Strelcov, S. Dmitriev, B. Button, J. Cothren, V. Sysoev, and A. Kolmakov. Evidence of the self-heating effect on surface reactivity and gas sensing of metal oxide nanowire chemiresistors. *Nanotechnology*, 19(35):355502 –5, 2008.

[111] J. D. Prades, F. Hernandez-Ramirez, A. Cirera, A. Romano-Rodriguez, and J. R. Morante. Harnessing self-heating in nanowires for energy efficient, fully autonomous and ultra-fast gas sensors. *Sensors and Actuators B: Chemical*, 144(1):1–5, 2010.

[112] O. Hayden, R. Agarwal, and C. M. Lieber. Nanoscale avalanche photodiodes for highly sensitive and spatially resolved photon detection. *Nature Materials*, 5(5): 352–356, 2006.

[113] C. Yang, C. J. Barrelet, F. Capasso, and C. M. Lieber. Single p-type/intrinsic/n-type silicon nanowires as nanoscale avalanche photodetectors. *Nano Letters*, 6(12): 2929–2934, 2006.

[114] C. García Núñez, A. García Marín, P. Nanterne, J. Piqueras, P. Kung, and J. L. Pau. Conducting properties of nearly depleted zno nanowire uv sensors fabricated by dielectrophoresis. *Nanotechnology*, 24(41):415702–10, 2013.

[115] J. H. He, Y. H. Lin, M. E. McConney, V. V. Tsukruk, Z. L. Wang, and G. Bao. Enhancing uv photoconductivity of zno nanobelt by polyacrylonitrile functionalization. *Journal of Applied Physics*, 102(8):084303–4, 2007.

[116] J. R. D. Retamal, C.-Y. Chen, D.-H. Lien, M. R. S. Huang, C.-A. Lin, C.-P. Liu, and J-H. He. Concurrent improvement in photogain and speed of a metal oxide nanowire photodetector through enhancing surface band bending via incorporating a nanoscale heterojunction. *ACS Photonics*, 1(4):354–359, 2014.

[117] C. S. Lao, M.-C Park, Q. Kuang, Y. Deng, A. K. Sood, D. L. Polla, and Z. L. Wang. Giant enhancement in uv response of zno nanobelts by polymer surface-functionalization. *Journal of the American Chemical Society*, 129(40):12096–12097, 2007.

[118] C. Lao, Y. Li, C. P. Wong, and Z. L. Wang. Enhancing the electrical and opto-electronic performance of nanobelt devices by molecular surface functionalization. *Nano Letters*, 7(5):1323–1328, 2007.

[119] M. W. Chen, C. Y. Chen, D. H. Lien, Y. Ding, and J. H. He. Photoconductive enhancement of single zno nanowire through localized schottky effects. *Optics Express*, 18(14):14836–14841, 2010.

[120] A. Pescaglini, A. Martín, D. Cammi, G. Juska, C. Ronning, E. Pelucchi, and D. Iacopino. Hot-electron injection in au nanorod-zno nanowire hybrid device for near-infrared photodetection. *Nano Letters*, 14(11):6202–6209, 2014.

[121] R. S. Aga, D. Jowhar, A. Ueda, Z. Pan, W. E. Collins, R. Mu, K. D. Singer, and J. Shen. Enhanced photoresponse in zno nanowires decorated with cdte quantum dot. *Applied Physics Letters*, 91(5):232108–3, 2007.

[122] D. Hou, A. Dev, K. Frank, A. Rosenauer, and T. Voss. Enhanced photoresponse in zno nanowires decorated with cdte quantum dot. *The Journal of Physical Chemistry C*, 116(36):19604–19610, 2012.

[123] C. Ronning, C. Borschel, S. Geburt, and R. Niepelt. Ion beam doping of semiconductor nanowires. *Materials Science and Engineering: R: Reports*, 70(3-6):30–43, 2010.

[124] Y. Cui and C. M. Lieber. Functional nanoscale electronic devices assembled using silicon nanowire building blocks. *Science*, 291(5505):851–853, 2001.

[125] P. Xie, Y. Hu, Y. Fang, J.Huang, and C.M. Lieber. Diameter-dependent dopant location in silicon and germanium nanowires. *Proceedings of the National Academy of Science*, 106(36):15254–15258, 2009.

[126] P Wickert H A Nilsson J Trägårdh K A Dick G Statkute P Ramvall K Deppert M T Borgström, E Norberg and L Samuelson. Precursor evaluation for in situ inp nanowire doping. *Nanotechnology*, 19(44):445602–6, 2008.

[127] A. Janotti and C. G. Van de Walle. Fundamentals of zinc oxide as a semiconductor. *Reports on Progress in Physics*, 72(12):126501–29, 2009.

[128] R. Noriega, J. Rivnay, L. Goris, D. Kälblein, H. Klauk, K. Kern, L. M. Thompson, A. C. Palke, J. F. Stebbins, J. R. Jokisaari, G. Kusinski, and A. Salleo. Probing the electrical properties of highly-doped al:zno nanowire ensembles. *Journal of Applied Physics*, 107(7):074312–7, 2010.

[129] G.-D. Yuan, W.-J. Zhang, J.-S. Jie, J.-X. Tang, I. Shafiq, Z.-Z Ye, C.-S. Lee, and S.-T. Lee. Tunable n-type conductivity and transport properties of ga-doped zno nanowire arrays. *Advanced Materials*, 20(1):168–173, 2008.

[130] D. Li, L. Zhao, R. Wu, C. Ronning, and J. G. Lu. Temperature-dependent photoconductance of heavily doped zno nanowires. *Nano Research*, 4(11):1110–1116, 2011.

[131] J. Hu and R. G. Gordon. Textured aluminum-doped zinc oxide thin films from atmospheric pressure chemical-vapor deposition. *Journal of Applied Physics*, 71(2): 880–890, 1992.

[132] J. Hu and R. G. Gordon. Atmospheric pressure chemical vapor deposition of gallium doped zinc oxide thin films from diethyl zinc, water, and triethyl gallium. *Journal of Applied Physics*, 72(11):5381–5392, 1992.

[133] H. J. Ko, Y. F. Chen, S. K. Hong, H. Wenisch, T. Yao, and D. C. Look. Ga-doped zno films grown on gan templates by plasma-assisted molecular-beam epitaxy. *Applied Physics Letters*, 77(23):3761–3763, 2000.

[134] C. Xu, M. Kim, J. Chun, and D. Kim. Growth of ga-doped zno nanowires by two-step vapor phase method. *Applied Physics Letters*, 86(13):133107–3, 2005.

[135] A. Janotti and C. G. Van de Walle. Native point defects in zno. *Physical Review B*, 76(16):165202–22, 2007.

[136] T. Yamamoto and H. Katayama-Yoshida. Solution using a codoping method to unipolarity for the fabrication of p-type zno. *Japanese Journal of Applied Physics*, 38(2B):L166–L169, 1999.

[137] P. Yu and M. Cardona. Fundamentals of semiconductors: Physics and materials properties. Springer, 2010.

[138] R. Calarco, M. Marso, T. Richter, A. I. Aykanat, R. Meijers, A. v.d. Hart, T. Stoica, and H. Lüth. Size-dependent photoconductivity in mbe-growth gan-nanowires. *Nano Letters*, 5(5):981–984, 2005.

[139] W. K. Hong, G. Jo, S. S. Kwon, S. Song, and T. Lee. Electrical properties of surface-tailored zno nanowire field-effect transistors. *IEEE Transactions on Electron Devices*, 55(11):3020–3029, 2008.

[140] C. H. Lin, T. T. Chen, and Y. F. Chen. Photocurrent enhancement of sno2 nanowires through au-nanoparticles decoration. *Optics Express*, 16(21):16916–16922, 2008.

[141] A. Kolmakov, D. O. Klenov, Y. Lilach, S. Stemmer, and M. Moskovits. Enhanced gas sensing by individual sno2 nanowires and nanobelts functionalized with pd catalyst particles. *Nano Letters*, 5(4):667–673, 2005.

[142] K. Horn. Semiconductor interface studies using core and valence level photoemission. *Applied Physics A: Materials Science & Processing*, 51(4):289–304, 1990.

[143] O.B. Aphek, L. Kronik, M. Leibovitch, and Y. Shapira. Quantitative assessment of the photosaturation technique. *Surface Science*, 409(3):485–500, 1998.

[144] M. Nirmal and L. Brus. Luminescence photophysics in semiconductor nanocrystals. *Accounts on Chemical Research*, 32(5):407–414, 1999.

[145] A. Soudi, C.-H. Hsu, and Y. Gu. Diameter-dependent surface photovoltage and surface state density in single semiconductor nanowires. *Nano Letters*, 12(10): 5111–5116, 2012.

[146] Z.-M. Liao, H.-Z. Zhang, Y.-B. Zhou, J. Xu, J.-M. Zhang, and D.-P. Yu. Surface effects on photoluminescence of single zno nanowires. *Physics Letters A*, 372(24): 4505–4509, 2008.

[147] C. Y. Chen, J. R. Duran Retamal, I. W. Wu, D. H. Lien, M. W. Chen, Y. Ding, Y. L. Chueh, C. I. Wu, and J. H. He. Probing surface band bending of surface-engineered metal oxide nanowires. *ACSNano*, 6(11):9366–9372, 2012.

[148] Y. Lin, D. Wang, Q. Zhao, Z. Li, Y. Ma, and M. Yang. Influence of adsorbed oxygen on the surface photovoltage and photoluminescence of zno nanorods. *Nanotechnology*, 17(9):2110–2115, 2006.

[149] P. B. Weisz. Effects of electronic charge transfer between adsorbate and solid on chemisorption and catalysis. *The Journal of Chemical Physics*, 21(9):1531–1538, 1953.

[150] J. D. Prades, F. Hernandez-Ramirez, R. Jimenez-Diaz, M. Manzanares, T. Andreu, A. Cirera, A. Romano-Rodriguez, and J. R. Morante. The effects of electron–hole separation on the photoconductivity of individual metal oxide nanowires. *Nanotechnology*, 19(46):465501–7, 2008.

[151] S. R. Morrison. Measurement of surface state energy levels of one-equivalent absorbates on zno. *Surface Science*, 27(3):586–604, 1971.

[152] S. M. Sze. Semiconductor devices: Physics and technology. John Wiley and Sons, inc., 2002.

[153] R. Enderlein and N. J. M Horing. Fundamentals of semiconductor physics. World Scientific, 1999.

[154] Z. Zhang and J. T. Yates Jr. Band bending in semiconductors: Chemical and physical consequences at surfaces and interfaces. *Chemical Reviews*, 112:5520–5551, 2012.

[155] H. T. Ng, J. Han, T. Yamada, P. Nguyen, Y. P. Chen, and M. Meyyappan. Single crystal nanowire vertical surround-gate field-effect transistor. *Nanotechnology*, 4 (7):1247–1252, 2004.

[156] Y. W. Heo, L. C. Tien, Y. Kwon, D. P. Norton, S. J. Pearton, B. S. Kang, and F. Ren. Depletion-mode zno nanowire field-effect transistor. *Applied Physics Letters*, 85(12):2274–2276, 2004.

[157] S. N. Cha, J. E. Jang, Y. Choi, G. A. J. Amaratunga, G. W. Ho, M. E. Welland, D. G. Hasko, D.-J. Kang, and J. M. Kim. High performance zno nanowire field effect transistor using self-aligned nanogap gate electrodes. *Applied Physics Letters*, 89 (26):263102–3, 2006.

[158] Y. Huang, X. Duan, Q. Wei, and C. M. Lieber. Directed assembly of one-dimensional nanostructures into functional networks. *Science*, 291(5504):630–633, 2001.

[159] W. Kim and K. S. Chu. Zno nanowire field-effect transistor as a uv photodetector; optimization for maximum sensitivity. *physica status solidi (a)*, 206(1):179–182, 2009.

[160] T. Oga, Y. Izawa, K. Kuriyama, K. Kushida, and Q. Xu. Persistent photoconductivity in electron-irradiated zno bulk single crystals: Evaluation of the metastable conductive state by the dual light illumination. *Solid State Communications*, 151 (22):1700–1703, 2011.

[161] P. I. Reyes, C.-J. Ku, Z. Duan, Y. Xu, E. Garfunkel, and Y. Lu. Reduction of persistent photoconductivity in zno thin film transistor-based uv photodetector. *Applied Physics Letters*, 101(3):031118–4, 2012.

[162] Y. Haddab and R. S. Popovic. Persistent photoconductivity in silicon wafers. *Semiconductor Science and Technology*, 13(11):1294–1297, 1998.

[163] C. H. Qiu and J. I. Pankove. Deep levels and persistent photoconductivity in gan thin films. *Applied Physics Letters*, 70(15):1983–1985, 1997.

[164] D. A. Melnick. Zinc oxide photoconduction, an oxygen adsorption process. *The Journal of Chemical Physics*, 26(5):1136–1146, 1957.

[165] K. Kuriyama, K. Matsumoto, Y. Suzuki, K. Kushida, and Q. Xu. Persistent photoconductivity and thermally stimulated current related to electron-irradiation induced defects in single crystal zno bulk. *Solid State Communications*, 149(33-34): 1347–1350, 2009.

[166] J. Reemts and A. Kitte. Persistent photoconductivity in highly porous zno films. *Journal of Applied Physics*, 101(1):013709–5, 2007.

[167] K. Moazzami, T. E. Murphy, J. D. Phillips, M. C.-K. Cheung, and A. N. Cartwright. Sub-bandgap photoconductivity in zno epilayers and extraction of trap density spectra. *Semiconductor Science and Technology*, 21(6):717–723, 2006.

[168] S. Lany and A. Zunger. Anion vacancies as a source of persistent photoconductivity in ii-vi and chalcopyrite semiconductors. *Physical Review B*, 72(3):035215–13, 2005.

[169] S. B. Zhang, S.-H. Wei, and Alex Zunger. Intrinsic n-type versus p-type doping asymmetry and the defect physics of zno. *Physical Review B*, 63(7):075205–7, 2001.

[170] A. v. Dijken, E. A. Meulenkamp, D. Vanmaekelbergh, and A. Meijerink. The kinetics of the radiative and nonradiative processes in nanocrystalline zno particles upon photoexcitation. *The Journal of Physical Chemistry B*, 104(8):1715–1723, 2001.

[171] S. A. Studenikin, N. Golego, and M. Cocivera. Optical and electrical properties of undoped zno films grown by spray pyrolysis of zinc nitrate solution. *Journal of Applied Physics*, 83(4):2104–2111, 1998.

[172] B. F. Spencer, D. M. Graham, S. J. O. Hardman, E. A. Seddon, M. J. Cliffe, K. L. Syres, A. G. Thomas, S. K. Stubbs, F. Sirotti, M. G. Silly, P. F. Kirkham, A. R. Kumarasinghe, G. J. Hirst, A. J. Moss, S. F. Hill, D. A. Shaw, S. Chattopadhyay, and W. R. Flavell. Time-resolved surface photovoltage measurements at n-type photovoltaic surfaces: Si(111) and zno(10 -10). *Physical Review B*, 88(19):195301–16, 2013.

[173] M. C. Tarun, F. A. Selim, and M. D. McCluskey. Persistent photoconductivity in strontium titanate. *Physical Review Letters*, 111(18):187403–5, 2013.

[174] S. H. Hosseini Shokouh, S. R. Raza, H. S. Lee HS, and S. Im. Non-classical logic inverter coupling a zno nanowire-based schottky barrier transistor and adjacent schottky diode. *Physical Chemistry Chemical Physics*, 16(31):16367–16372, 2014.

[175] E. Arslan, S. Bütün, S. B. Lisesivdin, M. Kasap, S. Ozcelik, and E. Ozbay. The persistent photoconductivity effect in algan/gan heterostructures grown on sapphire and sic substrates. *Journal of Applied Physics*, 103(10):103701–7, 2008.

[176] M. N. Berberan-Santos, E. N. Bodunov, and B. Valeur. Mathematical functions for the analysis of luminescence decays with underlying distributions 1. kohlrausch decay function (stretched exponential). *Chemical Physics*, 315(1-2):171–182, 2005.

[177] R. White, A. Colli, H. Li, and J. Kivioja. Input/output pulse operation of zno nanowire threshold integrators. *Nanotechnology*, 22(2):025207–8, 2011.

[178] G. Korotcenkov. Metal oxides for solid-state gas sensors: What determines our choice? *Materials Science and Engineering: B*, 139(1):1–23, 2007.

[179] T. Ishihara and S. Matsubara. Capacitive type gas sensors. *Journal of Electroceramics*, 2(4):215–228, 1998.

[180] I. Eisele, T. Doll, and M. Burgmair. Low power gas detection with fet sensors. *Sensors and Actuators B*, 78(1-3):19–25, 2001.

[181] S. Fanget, S. Hentz, P. Puget, J. Arcamone, M. Matheron, E. Colinet, P. Andreucci, L. Duraffourg, Ed. Myers, and M. L. Roukes. Gas sensors based on gravimetric detection-a review. *Sensors and Actuators B: Chemical*, 160(1):804–821, 2011.

[182] S. Todros, C. Baratto, E. Comini, G. Faglia, M. Ferroni, G. Sberveglieri, S. Lettieri, A. Setaro, L. Santamaria, and P. Maddalena. Optical gas sensing properties of zno nanowires. *Sensors and Microsystems, Lecture Notes in Electrical Engineering*, 54: 173–176, 2010.

[183] S. Capone, A. Forleo, L. Francioso, R. Rella, P. Siciliano, J. Spadavecchia, D. S. Presicce, and A. M. Taurino. Solid state gas sensors: State of the art and future activities. *Journal of Optoelectronics and Advanced Materials*, 5(5):1335–1348, 2003.

[184] I.-D. Kima, A. Rothschild, and H. L. Tuller. Advances and new directions in gas-sensing devices. *Acta Materialia*, 61(3):974–1000, 2013.

[185] N. Barsan and U. Weimar. Conduction model of metal oxide gas sensors. *Journal of Electroceramics*, 7(3):143–167, 2001.

[186] Q. Yuan, Y.-P. Zhao, L. Li, and T. Wang. Ab initio study of zno-based gas-sensing mechanisms: Surface reconstruction and charge transfer. *The Journal of Physical Chemistry C*, 113(15):6107–6113, 2009.

[187] S.-J. Chang, T.-J. Hsueh, I.-C. Chen, and B.-R. Huang. Highly sensitive zno nanowire co sensors with the adsorption of au nanoparticles. *Nanotechnology*, 19 (17):175502–5, 2008.

[188] T. I. Barry and F. S. Stone. The reactions of oxygen at dark and irradiated zinc oxide surface. *Proceedings of the Royal Society of London*, 255(1280):124–144, 1960.

[189] Y. Yan, M. M. Al-Jassim, and S.-H. Wei. Oxygen-vacancy mediated adsorption and reactions of molecular oxygen on the zno(101-0) surface. *Physical Review B*, 72(16):161307–4, 2005.

[190] G. Eranna. Metal oxide nanostructures as gas sensing devices. *CRC Press*, 2011.

[191] Q. Yuan, Y.-P. Zha, L. Li, and T. Wang. Ab initio study of zno-based gas-sensing mechanisms: Surface reconstruction and charge transfer. *The Journal of Physical Chemistry C*, 113(15):6107–6113, 2009.

[192] C. Borchers, S. Müller, D. Stichtenoth, D. Schwen, and C. Ronning. Catalyst-nanostructure interaction in the growth of 1-d zno nanostructures. *The Journal of Physical Chemistry B*, 110(4):1656–60, 2006.

[193] S. Müller. Wachstum von zno nanodrähten und deren dotierung durch ionenstrahlen. *Diplomarbeit, Universität Göttingen*, 2005.

[194] M. Gnauck. Elektrische kontaktierung von zno-nanostrukturen und deren verwendung für sensorische zwecke. *Diplomarbeit, Universität Jena*, 2010.

[195] M. Kozlik. Synthese von halbleiternanodrähten für die photonik. *Diplomarbeit, Universität Jena*, 2009.

[196] S. Milz. Konzepte zur realisierung von einfachen nanodrahtbauelementen für die energiegewinnung. *Diplomarbeit, Universität Jena*, 2010.

[197] A. K.-K. Wong. Resolution enhancement techniques in optical lithography. *(SPIE Tutorial Texts in Optical Engineering Vol. TT47)*, 2001.

[198] R. Niepelt. Characterisation and selective modification of semiconductor nanowires for electrical applications. *Doktorarbeit, Universität Jena*, 2012.

[199] Fotolithografie. MicroChemicals GmbH, Ulm, www.microchemicals.eu, 2012.

[200] R. Pretorius, J.M. Harris, and M. A. Nicolet. Reaction of thin metal films with sio2 substrates. *Solid-State Electronics*, 21(4):667–675, 1978.

[201] Keithley instruments, inc. www.keithley.com, 2012.

[202] SÜss microtec ag. www.suss.com, 2012.

[203] Mks instruments deutschland gmbh. *http://www.mksinst.com/intl/DE1.aspx.*

[204] S. Geburt. Lasing and ion beam doping of semiconductor nanowires. pages 212106–3, University of Jena, Jena, Germany, 2013; http://www.db-thueringen.de/servlets/DocumentServlet?id=22078.

[205] High Voltage Engineering Europa B.V. High voltage ion accelerator. www.highvolteng.com.2012, 2012.

[206] J. F. Ziegler, J. P. Biersack, and U. Littmark. The stopping and ranges of ions in solids. *Pergamon Press, New York*, 1985.

[207] J. F. Ziegler, M. D. Ziegler, and J. P. Biersack. Srim-the stopping and range of ions in matter. *Nuclear Instruments and Methods in Physics Research Section B: Beam Interactions with Materials and Atoms*, 268(11-12):1818–1823, 2010.

[208] D. Cammi, R. Roeder, and C. Ronning. Gate modulation of below-band-gap photoconductivity in zno nanowire field-effect-transistors. *Journal of Physics D: Applied Physics*, 47(39):394014–6, 2014.

[209] D. K. Schroder. Semiconductor material and device characterization, 3rd edition. *Wiley, New York*, 2006.

[210] A. J Chiquito, C. A. Amorim, O. M Berengue, L. S Araujo, E. P Bernardo, and E. R Leite. Back-to-back schottky diodes: the generalization of the diode theory in analysis and extraction of electrical parameters of nanodevices. *Journal of Physics: Condensed Matter*, 24(22):225303–7, 2012.

[211] Z.-M. Liao, C. Hou, Y.-B. Zhou, J. Xu, J.-M. Zhang, and D.-P. Yu. Influence of temperature and illumination on surface barrier of individual zno nanowires. *The Journal of Chemical Physics*, 130(8):084708–4, 2009.

[212] K. Ip, G. T. Thaler, H. Yang, H. S. Youn Han, Y. Li, D. P. Norton, S. J. Pearton, S. Jang, and F. Ren. Contacts to zno. *Journal of Crystal Growth*, 287(1):149–156, 2006.

[213] H. S. Yang, D. P. Norton, S. J. Pearton, and F. Ren. Ti/ au n-type ohmic contacts to bulk zno substrates. *Applied Physics letters*, 87(21):212106–3, 2005.

[214] D. Somvanshi and S. Jit. Mean barrier height and richardson constant for pd/zno thin film-based schottky diodes grown on n-si substrates by thermal evaporation method. *IEEE Electron Device Letters*, 34(10):1238–1240, 2013.

[215] K. Jacobi, G. Zwicker, and A. Gutmann. Work function, electron affinity and band bending of zinc oxide surfaces. *Surface Science*, 141(1):109–125, 1984.

[216] J. Hölzl and F. K. Schulte. Work functions of metals. *Solid Surface Physics*, 1979.

[217] Carlo Lamberti and Giovanni Agostini. Characterization of semiconductor heterostructures and nanostructures, second edition. *Elsevier*, 2013.

[218] J. Yoon, W.-K. Hong, M. Jo, G. Jo, M. Choe, W. Park, J. I. Sohn, S. Nedic, H. Hwang, M. E. Welland, and T. Lee. Nonvolatile memory functionality of zno nanowire transistors controlled by mobile protons. *ACS Nano*, 5(1):558–564, 2011.

[219] M. Choe M, W. Park, J. W. Kang, S. Jeong, W. K. Hong, B. H. Lee, S. J. Park, and T. Lee. Investigation of threshold voltage instability induced by gate bias stress in zno nanowire field effect transistors. *Nanotechnology*, 23(48):485201–7, 2012.

[220] A. Johannes. In-situ characterisation of ion-doped zinc oxide nanowires. *Diplomarbeit, Universität Jena*, 2011.

[221] K. Keem, J. Kang, C. Yoon, D. Yeom, D. Y. Jeong, B. Park, J. Park, and S. Kim. Zno nanowire-based nonvolatile memory devices with al2o3 layers as storage nodes. *Journal of Nanoscience and Nanotechnology*, 9(7):4240–4243, 2009.

[222] J. I. Sohn, S. S. Choi, S. M. Morris, J. S. Bendall, H. J. Coles, W.-K. Hong, G. Jo, T. Lee, and M. E. Welland. Novel nonvolatile memory with multibit storage based on a zno nanowire transistor. *Nano Letters*, 10(11):4316–4320, 2010.

[223] K. Keem, J. Kang, C. Yoon, D. Yeom, D. Y. Jeong, B. Park, J. Park, and S. Kim. Zno nanowire-based nonvolatile memory devices with al2o3 layers as storage nodes. *Journal of Nanoscience and Nanotechnology*, 9(7):4240–4243, 2009.

[224] M. Noltemeyer, F. Bertram, T. Hempel, B. Bastek, A. Polyakov, J. Christen, M. Brandt, M. Lorenz, and M. Grundmann. Excitonic transport in zno. *Journal of Materials Research*, 27(17):2225–2231, 2012.

[225] S. R. Raza, Y. T. Lee, Y. G. Chang, P. J. Jeon, J. H. Kim, R. Ha, H. J. Choi, and S. Im. Photoelectric probing of the interfacial trap density-of-states in zno nanowire field-effect transistors. *Physical Chemistry Chemical Physics*, 15(8):2660–2664, 2013.

[226] L. Yang, Q. Wang, X. Tao, S. P. Taylor, and Y. Gu. Gate-tunable photocurrent in zno nanowires mediated by nanowire-substrate interface states. *Applied Physics Letters*, 106(9):093111–5, 2015.

[227] K. L. Ngai and C. T. White. A model of interface states and charges at the si-sio2 interface: Its predictions and comparison with experiments. *Applied Physics Letters*, 52(1):320–337, 1981.

[228] J. M. Sung and S. A. Lyon. Cycling of defects between trapped negative charge and interface states at the si-sio2 interface. *Applied Physics Letters*, 50(17):1152–1154, 1987.

[229] T.-Y. Chen, C.-S. Pang, and J.-G. Hwu. Effect of electrons trapping/de-trapping at si-sio2 interface on two-state current in mos(p) structure with ultra-thin sio2 by anodization. *ECS Journal of Solid State Science and Technology*, 2(9):Q159–Q164, 2013.

[230] W.-K. Hong, G. Jo, J. I. Sohn, W. Park, M. Choe, G. Wang, Y. H. Kahng, M. E. Welland, and T. Lee. Tuning of the electronic characteristics of zno nanowire field effect transistors by proton irradiation. *ACS Nano*, 4(2):811–818, 2010.

[231] Z. H. Zhang, X. Y. Qi, J. K. Jian, and X. F. Duan. Investigation on optical properties of zno nanowires by electron energy-loss spectroscopy. *Micron*, 37(3): 229–233, 2006.

[232] C García Núñez, A. García Marín, P. Nanterne, J. Piqueras, P. Kung, and J. L. Pau. Conducting properties of nearly depleted zno nanowire uv sensors fabricated by dielectrophoresis. *Nanotechnology*, 24(41):415702–10, 2013.

[233] J. D. Prades, R. Jimenez-Diaz, F. Hernandez-Ramirez, L. Fernandez-Romero, T. Andreu, A. Cirera, A. Romano-Rodriguez, A. Cornet, J. Ramon Morante, S. Barth, and S. Mathur. Toward a systematic understanding of photodetectors based on individual metal oxide nanowires. *The Journal of Physical Chemistry C*, 112(37):14639–14644, 2008.

[234] H. Zhang, A. V. Babichev, G. Jacopin, P. Lavenus, F. H. Julien, A. Yu. Egorov, J. Zhang, T. Pauporté, and M. Tchernycheva. Characterization and modeling of a zno nanowire ultraviolet photodetector with graphene transparent contact. *Journal of Applied Physics*, 114(23):234505–9, 2013.

[235] B. Mallampati, S. V. Nair, H. E. Ruda, and U. Philipose. Role of surface in high photoconductive gain measured in zno nanowire-based photodetector. *Journal of Nanoparticle Research*, 17(4):1–10, 2015.

[236] S. A. Studenikin, N. Golego, and M. Cocivera. Carrier mobility and density contributions to photoconductivity transients in polycrystalline zno films. *Journal of Applied Physics*, 87(5):2413–2421, 2000.

[237] C. Aharoni and F. C. Tompkins. Kinetics of adsorption and desorption and the elovich equation. *Advances in Catalysis*, 21:1–49, 1970.

[238] M. J. D. Low. Kinetics of chemisorption of gases on solids. *Chemical Reviews*, 60 (3):267–312, 1960.

[239] J. C. Moore and C. V. Thompson. A phenomenological model for the photocurrent transient relaxation observed in zno-based photodetector devices. *Sensors (Basel)*, 13(8):9921–9940, 2013.

[240] M.-W. Chen, J. R. D. Retamal, C.-Y. Chen, and J.-H. He. Photocarrier relaxation behavior of a single zno nanowire uv photodetector: Effect of surface band bending. *IEEE Electron Device Letters*, 33(3):411–413, 2012.

[241] S. Mridha and D. Basak. Aluminium doped zno films: electrical, optical and photoresponse studies. *Journal of Physics D: Applied Physics*, 40(22):6902–6907, 2007.

[242] M. Li, G. Xing, G. Xing, B. Wu, T. Wu, X. Zhangi, and T. C. Sum. Origin of green emission and charge trapping dynamics in zno nanowires. *Physical Review B*, 87 (11):115309–8, 2013.

[243] V. A. Nikitenko, K. E. Tarkpea, I. V. Pykanov, S. V. Mukhin, S. G. Stoyukhin, and P. G. Pas'ko. Thermally stimulated electron-hole and ionic processes in zinc oxide crystals. *Journal of Applied Spectroscopy*, 67(5):883–887, 2000.

[244] H.-Y. Chen, R. S. Chen, N. K. Rajan, F.-C. Chang, L.-C. Chen, K.-H. Chen, Y.-J. Yang, and M. A. Reed. Size-dependent persistent photocurrent and surface band bending in m-axial gan nanowires. *Physical Review B*, 84(20):205443–7, 2011.

[245] M. Li, G. Xing, Q. Ah, F. N. Lloyd, G. Xing, T. Wu, C. H. A. Huan, X. Zhang, and T. C. Sum. Tailoring the charge carrier dynamics in zno nanowires: the role of surface hole/electron traps. *Physical Chemistry Chemical Physics*, 14(9):3075–3082, 2012.

[246] L. R. Covington and J. C. Moore. Photoconductivity and transient response of al:zno:al planar structures fabricated via a thermal oxidation process. *Thin Solid Films*, 540(4):106–111, 2013.

[247] E. R. Viana, J. C. Gonzalez, G. M. Ribeiro, and A. G. de Oliveira. Photoluminescence and high-temperature persistent photoconductivity experiments in sno2 nanobelts. *The Journal of Physical Chemistry C*, 117(15):7844–7849, 2013.

[248] K. Huang and Q. Zhang. Giant persistent photoconductivity of the wo3 nanowires in vacuum condition. *Nanoscale Research Letters*, 6(52):1–5, 2011.

[249] R. S. Chen, C. Y. Lu, K. H. Chen, and L. C. Chen. Molecule-modulated photoconductivity and gain-amplified selective gas sensing in polar gan nanowires. *Applied Physics Letters*, 95(23):233119–3, 2009.

[250] Michelle Geelen. Ion beam doping and defect engineering of zno nanowires for photodetection and sensing applications. *Master's Thesis, Universiteit Hasselt*, 2015.

[251] Z. Liu, J. Xu, D. Chen, and G. Shen. Flexible electronics based on inorganic nanowires. *Chemical Society Reviews*, 44(1):161–192, 2015.

[252] D. Chen, Z. Liu, B. Liang, X. Wang, and G. Shen. Transparent metal oxide nanowire transistors. *Nanoscale*, 4(10):3001–3012, 2012.

[253] Y.-J. Lee, D. S. Ruby, D. W. Peters, B. B. McKenzie, and J. W. P. Hsu. Zno nanostructures as efficient antireflection layers in solar cells. *Nano Letters*, 8(5): 1501–1505, 2008.

[254] Y.-C. Chao, C.-Y. Chen, C.-A. Lin, Y.-A. Dai, and J.H. He. Antireflection effect of zno nanorod arrays. *Journal of Materials Chemistry*, 2010(37):8134–8138, 20.

[255] D. Y. Kim and J. Y. Son. Horizontal zno nanowires for gas sensor application: Al-doping effect on sensitivity. *Electrochemical and Solid-State Letters*, 12(12): J109–J111, 2009.

[256] S. Y. Lee. Sensing properties of ga-doped zno nanowire gas sensor. *Transactions on Electrical and Electronic Materials*, 16(2):78–81, 2015.

[257] Y. Feng, W. Hou, X. Zhang, P. Lv, Y. Li, and W. Feng. Highly sensitive reversible light-driven switches using electrospun porous aluminum-doped zinc oxide nanofibers. *The Journal of Physical Chemistry C*, 115(10):3956–3961, 2011.

[258] D. Lin, H. Wu, and W. Pan. Photoswitches and memories assembled by electrospinning aluminum-doped zinc oxide single nanowires. *Advanced Materials*, 19(22): 3968–3972, 2007.

[259] H. P. He, H. P. Tang, Z. Z. Ye, L. P. Zhu, B. H. Zhao, L. Wang, and X. H. Li. Temperature-dependent photoluminescence of quasialigned al-doped zno nanorods. *Applied Physics Letters*, 90(2):023104–3, 2007.

[260] L. Goris, R. Noriega, M. Donovan, J. Jokisaari, G. Kusinski, and A. Salleo. Intrinsic and doped zinc oxide nanowires for transparent electrode fabrication via low-temperature solution synthesis. *Journal of Electronic Materials*, 38(4):586–595, 2009.

[261] M. H. Mamat, Z. Khusaimi, M. M. Zahidi, and M. R. Mahmood. Performance of an ultraviolet photoconductive sensor using well-aligned aluminium-doped zinc-oxide nanorod arrays annealed in an air and oxygen environment. *Japanese Journal of Applied Physics*, 50(6S):06GF05–4, 2011.

[262] S. Dhara and P. K. Giri. Improved fast photoresponse from al doped zno nanowires network decorated with au nanoparticles. *Chemical Physics Letters*, 541:39–43, 2012.

[263] L. J. Brillson and Y. Lu. Zno schottky barriers and ohmic contacts. *Journal of Applied Physics*, 109(12):121301–33, 2011.

[264] S.-H. Kim, S.-W. Jeong, D.-K. Hwang, S.-J. Park, and T.-Y. Seong. Zn/au ohmic contacts on n-type zno epitaxial layers for light-emitting devices. *Electrochemical and Solid-State Letters*, 8(8):G198–G200, 2005.

[265] H.-K. Kim, S.-H. Han, T.-Y. Seong, and W.-K. Choi. Low-resistance ti/au ohmic contacts to al-doped zno layers. *Applied Physics Letters*, 77(11):1647–1649, 2000.

[266] S. Geburt, D. Stichtenoth, S. Müller, W. Dewald, C. Ronning, J. Wang, Y. Jiao, Y. Y. Rao, S. K. Hark, and Q. Li. Rare earth doped zinc oxide nanowires. *Journal of Nanoscience and Nanotechnology*, 8(1):244–251, 2008.

[267] D. Weissenberger, M. Dürrschnabel, D. Gerthsen, F. Pérez-Willard, A. Reiser, G. M. Prinz, M. Feneberg, K. Thonke, and R. Sauer. Conductivity of single zno nanorods after ga implantation in a focused-ion-beam system. *Applied Physics Letters*, 91(13):132110–3, 2007.

[268] D. Stichtenoth. Dimensional effects in semiconductor nanowires. *PhD Thesis, University of Göttingen, 2008*, (http://webdoc.sub.gwdg.de/diss/2008/stichtenoth/).

[269] S. O. Kucheyev, J. S. Williams, C. Jagadish, J. Zou, Cheryl Evans, A. J. Nelson, and A. V. Hamza. Ion-beam-produced structural defects in zno. *Physical Review B*, 67(9):094115–11, 2003.

[270] S.O. Kucheyev, J. S. Williams, and S. J. Pearton. Ion implantation into gan. *Materials Science & Engineering R: Reports*, 33:51–107, 2001.

[271] K. Lorenz and E. Wendler. Implantation damage formation in gan and zno. *Ion Implantation*, Chapter 11, Edited by Mark Goorsky, Publisher InTech, 2012.

[272] K. Trachenko. Understanding resistance to amorphization by radiation damage. *Journal of Physics: Condensed Matter*, 16(49):R1491–R1515, 2004.

[273] S. Geburt, M. Lorke, A. L. da Rosa, T. Frauenheim, R. Röder, T. Voss, U. Kaiser, W. Heimbrodt, and C. Ronning. Intense intrashell luminescence of eu-doped single zno nanowires at room temperature by implantation created eu–oi complexes. *Nano Letters*, 14(8):4523–4528, 2014.

[274] S. Müller. Structural and optical impact of transition metal implantation into zinc oxide single crystals and nanowires. *PhD Thesis, University of Göttingen, 2009*, (https://ediss.uni-goettingen.de/handle/11858/00-1735-0000-0006-B487-7).

[275] C. Borschel, S. Spindler, D. Lerose, A. Bochmann, S. H. Christiansen, S. Nietzsche, M. Oertel, and C. Ronning. Permanent bending and alignment of zno nanowires. *Nanotechnology*, 22(18):185307–9, 2011.

[276] K. Vanheusden, C. H. Seager, W. L. Warren, D. R. Tallant, and J. A. Voigt. Correlation between photoluminescence and oxygen vacancies in zno phosphors. *Applied Physics Letters*, 68(3):403–405, 1996.

[277] K. Vanheusden, W. L. Warren, C. H. Seager, D. R. Tallant, J. A. Voigt, and B. E. Gnade. Mechanisms behind green photoluminescence in zno phosphor powders. *Journal of Applied Physics*, 79(10):7983–7990, 1996.

[278] D. C. Reynolds, D. C. Look, B. Jogai, and H. Morkoç. Similarities in the band-edge and deep-centre photoluminescence mechanisms of zno and gan. *Solid State Communications*, 101(9):643–646, 1997.

[279] D. C. Reynolds, D. C. Look, B. Jogai, J. E. Van Nostrand, R. Jones, and J. Jenny. Source of the yellow luminescence band in gan grown by gas-source molecular beam epitaxy and the green luminescence band in single crystal zno. *Solid State Communications*, 106(10):701–704, 1998.

[280] A. Pöppl und G. Völkel. Esr and photo-esr investigations of zinc vacancies and interstitial oxygen ions in undoped zno ceramics. *Physica Status Solidi (a)*, 125: 571–581, 1991.

[281] H. von Wenckstern, G. Benndorf, S. Heitsch, J. Sann, M. Brandt, H. Schmidt, J. Lenzner, M. Lorenz, A. Kuznetsov, B. Meyer, and M. Grundmann. Properties of phosphorus doped zno. *Applied Physics A: Materials Science & Processing*, 88 (1):125–128, 2007.

[282] B. K. Meyer, H. Alves, D. M. Hofmann, W. Kriegseis, D. Forster, F. Bertram, J. Christen, A. Hoffmann, M. Straßburg, M. Dworzak, U. Haboeck, and A. V. Rodina. Bound exciton and donor-acceptor pair recombinations in zno. *Physica Status Solidi (b)*, 241(2):231–260, 2004.

[283] B. K. Meyer, J. Sann, D. M. Hofmann, C. Neumann, and A. Zeuner. Shallow donors and acceptors in zno. *Semiconductor Science and Technology*, 20(4):S62–S66, 2005.

[284] H. Shibata, H. Tampo, M. Sakai, A. Yamada, K. Matsubara, K. Sakurai, S. Ishizuka, K. Kim, P. Fons, K. Iwata, S. Niki, K. Tamura, K. Nakahara, H. Takasu, K. Maeda,

and I. Niikura. Photoluminescence recombination centers in zno. *physica status solidi (c)*, 3(4):1026–1029, 2006.

[285] S. Müller, D. Stichtenoth, M. Uhrmacher, H. Hofsäss, C. Ronning, and J. Roder. Unambiguous identification of the pl-i_9 line in zinc oxide. *Applied Physics Letters*, 90(1):012107–3, 2007.

[286] B. K. Meyer, J. Sann, S. Lautenschlager, M. R. Wagner, and A. Hoffmann. Ionized and neutral donor-bound excitons in zno. *Physical Review B*, 76(18):184120–4, 2007.

[287] V. V. Travnikov, A. Freiberg, and S. F. Savikhin. Surface excitons in zno crystals. *Journal of Luminescence*, 47(3):107–112, 1990.

[288] L. Wischmeier, C. Bekeny, T. Voss, S. Börner, and W. Schade. Optical properties of single zno nanowires. *Physica Status Solidi (b)*, 243(4):919–923, 2006.

[289] K. Wu, H. He, Y. Lu, J. Huang, and Z. Ye. Dominant free exciton emission in zno nanorods. *Nanoscale*, 4(5):1701–6, 2012.

[290] C. F. Klingshirn. Semiconductor optics. *Springer, 2nd edition, 2005.*

[291] X. L. Wu, G. G. Siu, C. L. Fu, and H. C. Ong. Photoluminescence and cathodoluminescence studies of stoichiometric and oxygen-deficient zno films. *Applied Physics Letters*, 78(16):2285–2287, 2001.

[292] M. Zapf. Oberflächenmodifikation von zno-halbleiternanodrähten für sensorische anwendungen und die uv-photodetektion. *Bachelorarbeit, Universität Jena*, 12(5), 2014.

[293] A Kolmakov. The effect of morphology and surface doping on sensitization of quasi-1d metal oxide nanowire gas sensors. *Proceedings of SPIE*, 6370:63700X–63700X–8, 2006.

[294] Z. L. Wang. Characterizing the structure and properties of individual wire-like nanoentities. *Advanced Materials*, 12(17):1295–1298, 2000.

[295] Andrei Kolmakov and Martin Moskovits. Chemical sensing and catalysis by one-dimensional metal-oxide nanostructures. *Annual Review of Materials Research*, 34: 151–180, 2004.

[296] S. N. Das, J. P. Kar, J.-H. Choi, T. Il Lee, K.-J. Moon, and J.-M. Myoung. Fabrication and characterization of zno single nanowire-based hydrogen sensor. *The Journal of Physical Chemistry C*, 114(3):1689–1693, 2010.

[297] H. T. Wang, B. S. Kang, F. Ren, L.-C. Thien, P. W. Sadik, and D. P. Norton. Hydrogen-selective sensing at room temperature with pt-coated zno nanorods. *Applied Physics Letters*, 86(24):243503–3, 2005.

[298] C. S. Rout, S. H. Krishna, S. R. C. Vivekchand, A. Govindaraj, and C. N. R. Rao. Hydrogen and ethanol sensors based on zno nanorods, nanowires and nanotubes. *Chemical Physics Letters*, 418(4-6):586–590, 2006.

[299] W. Novis Smith and J. G. Santangelo. Hydrogen: Production and marketing. *W. Novis Smith*, 1980.

[300] L. P. Bicelli. Hydrogen: A clean energy source. *International Journal of Hydrogen Energy*, 11(9):555–562, 1986.

[301] P. Soundarrajan and F. Schweighardt. Hydrogen sensing and detection. *Taylor & Francis Group, LLC*, 2009.

[302] J. Huh, J. Park, G. T. Kim, and J. Y. Park. Highly sensitive hydrogen detection of catalyst-free zno nanorod networks suspended by lithography-assisted growth. *Nanotechnology*, 22(8):085502–7, 2011.

[303] L. C. Tien, P. W. Sadik, D. P. Norton, L. F. Voss, S. J. Pearton, H. T. Wang, B. S. Kang, F. Ren, J. Jun, and J. Lin. Hydrogen sensing at room temperature with pt-coated zno thin films and nanorods. *Applied Physics Letters*, 87(22):222106–3, 2005.

[304] C. Wang, L. Yin, L. Zhang, D. Xiang, and R. Gao. Metal oxide gas sensors: Sensitivity and influencing factors. *Sensors (Basel)*, 10(3):2088–2106, 2010.

[305] Safety standard for hydrogen and hydrogen systems: Guidelines for hydrogen system design, materials selection, operations, storage and transportation. *NASA*, 1997.

[306] Y. Yan, M. M. Al-Jassim, and S.-H. Wei. Oxygen-vacancy mediated adsorption and reactions of molecular oxygen on the zno(10-10) surface. *Physical Review B*, 72(16):161307–4, 2005.

[307] K. K. Korir, A. Catellani, and G. Cicero. Ethanol gas sensing mechanism in zno nanowires: An ab initio study. *The Journal of Physical Chemistry C*, 118(42): 24533–24537, 2014.

[308] B. Fubini, E. Giamello, G. Della Gatta, and G. Venturello. Adsorption of hydrogen on zinc oxide. energy of interaction and related mechanisms. *Journal of the Chemical Society, Faraday Transactions 1: Physical Chemistry in Condensed Phases*, 78(1): 153–164, 1982.

[309] H. Watanabe, M. Wada, and T. Takahashi. The activation energy for oxygen desorption from zinc oxide surfaces. *Japanese Journal of Applied Physics*, 4(12): 945–947, 1965.

[310] W. An, X. Wu, and X. C. Zeng. Adsorption of o2, h2, co, nh3, and no2 on zno nanotube: A density functional theory study. *The Journal of Physical Chemistry C*, 112(15):5747–5755, 2008.

[311] P. F. Williams. Plasma processing of semiconductors. *edited by P. F. Williams*, Springer Verlag, 2013.

[312] H.-W. Ra, R. Khan, J. T. Kim, B. R. Kang, K. H. Bai, and Y. H. Im. Effects of surface modification of the individual zno nanowire with oxygen plasma treatment. *Materials Letters*, 63(28):2516–2519, 2009.

[313] H.-W. Ra, K. S. Choi, C. W. Ok, S. Y. Jo, K. H. Bai, and Y. H. Im. Ion bombardment effects on zno nanowires during plasma treatment. *Applied Physics Letters*, 93(3):033112–3, 2008.

[314] J.-D. Kwon, J.-W. Lee, K.-S. Nam, D.-H. Kim, Y. Jeong, S.-H. Kwon, and J.-S. Park. The impact on in-situ-hydrogen-plasma treatment for zinc oxide plasma enhanced atomic layer deposition. *Current Applied Physics*, 12(S2):S134 – S138, 2012.

[315] K. K. Korir. Zno nanowires for energy harvesting and gas sensing applications: a quantum mechanical study. *PhD Thesis*, Politecnico di Torino, Torino, Italy, 2014, http://porto.polito.it/2539901/.

[316] M.-W. Ahn, K.-S. Park, J.-H. Heo, J.-G. Park, D.-W. Kim, K. J. Choi, J.-H. Lee, and S.-H. Hong. Gas sensing properties of defect-controlled zno-nanowire gas sensor. *Applied Physics Letters*, 93(26):263103–3, 2008.

[317] A. Dev, R. Niepelt, J. P. Richters, C. Ronning, and T. Voss. Stable enhancement of near-band-edge emission of zno nanowires by hydrogen incorporation. *Nanotechnology*, 21(6):065709–5, 2010.

[318] W. H. Doh, P. C. Roy, and C. M. Kim. Interaction of hydrogen with zno: Surface adsorption versus bulk diffusion. *Langmuir*, 26(21):16278–16281, 2010.

[319] D. D. Kälblein. Field-effect transistors based on zno nanowires. *PhD Thesis*, École Polytechnique Fédérale de Lausanne, Lausanne, 2011.

[320] A. M. Gheis, C. Neygandhi, A. K. Sternig, E. Carrasco, H. Marbach, D. Thomele, and O. Diwald. O2 adsorption dependent photoluminescence emission from metal oxide nanoparticles. *Physical Chemistry Chemical Physics*, 16(43):23922–23929, 2014.

[321] J. Onsgaard, S. M. Barlow, and T. E. Gallon. Clean zno surfaces and oxygen adsorption on the (0001) surface studied by electron spectroscopy. *Journal of Physics C: Solid State Physics*, 12(5):925–942, 1979.

Appendix

List of publications

Publications directly related to this thesis

Persistent photoconductivity in zno nanowires in different atmospheres
D. Cammi and C. Ronning
Advances in Condensed Matter Physics, 2014(Article ID 184120), 2014

Gate modulation of below-band-gap photoconductivity in zno nanowire field-effect-transistors
D. Cammi, R. Röder and C. Ronning
Journal of Physics D: Applied Physics, 47(39):394014-6, 2014

Other publications

Hot-Electron Injection in Au Nanorod–ZnO Nanowire Hybrid Device for Near-Infrared Photodetection
A. Pescaglini, A. Martin, **D. Cammi**, G. Juska, C. Ronning, E. Pelucchi, and D. Iacopino
Nano Letters, 14(11):6202-6209, 2014

Non-resonant Raman Spectroscopy of Individual ZnO Nanowires via Au Nanorod Surface Plasmons
A. Pescaglini, E. Secco, A. Martin, **D. Cammi**, C. Ronning, A. Cantarero, N. Garro and D. Iacopino
submitted to The Journal of Physical Chemistry (2015)

Ehrenwörtliche Erklärung

Ich erkläre hiermit ehrenwörtlich, dass ich die vorliegende Arbeit selbstständig, ohne unzulässige Hilfe Dritter und ohne Benutzung anderer als der angegebenen Hilfsmittel und Literatur angefertigt habe. Die aus anderen Quellen direkt oder indirekt übernommenen Daten und Konzepte sind unter Angabe der Quelle gekennzeichnet.

Bei der Auswahl und Auswertung folgenden Materials haben mir die nachstehend aufgeführten Personen in der jeweils beschriebenen Weise unentgeltlich geholfen:

- Die Herstellung und die Kontaktierung der ZnO Nanodrähte wurden zusammen mit Maximilian Zapf, Sascha Creutzburg und Michelle Geelen durchgeführt.
- Die elektrischen Messungen auf die plasma-behandelten ZnO Nanodrähte wurden in Zusammenarbeit mit Maximilian Zapf durchgeführt.
- Die elektrischen Messungen auf die implantierten ZnO Nanodrähte wurden in Zusammenarbeit mit Michelle Geelen durchgeführt.
- Die Ionenimplantationen wurden in Zusammenarbeit mit Michelle Geelen, Andreas Johannes und mit der Hilfe von Patrick Hoffmann durchgeführt.
- Die Plasmabehandlungen wurden in Zusammenarbeit mit Maximilian Zapf, Ronny Nawrodt and Christian Schwarz durchgeführt.
- Im Übrigen waren jeweils die Koautoren der angeführten Veröffentlichungen (siehe Anhang List of publications) an der Interpretation der Ergebnisse beteiligt.

Weitere Personen waren an der inhaltlich-materiellen Erstellung der vorliegenden Arbeit nicht beteiligt. Insbesondere habe ich hierfür nicht die entgeltliche Hilfe von Vermittlungs- bzw. Beratungsdiensten (Promotionsberater oder andere Personen) in Anspruch genommen. Niemand hat von mir unmittelbar oder mittelbar geldwerte Leistungen für die Arbeiten erhalten, die im Zusammenhang mit dem Inhalt der vorgelegten Dissertation stehen. Die Arbeit wurde bisher weder im In- noch im Ausland in gleicher oder ähnlicher Form einer anderen Prüfungsbehörde vorgelegt. Die geltende Prüfungsordnung der Physikalisch-Astronomischen Fakultät ist mir bekannt. Ich versichere ehrenwörtlich, dass ich nach bestem Wissen die reine Wahrheit gesagt und nichts verschwiegen habe.

Jena, den 04.11.2015 Davide Cammi

Curriculum Vitae

Persönliche Daten

Name:	Davide Cammi
Geburtsdatum:	24.04.1985
Geburtsort:	Fiorenzuola d'Arda (PC), Italien

Bildungsweg

1991 - 1996	Scuola Elementare San "G. Bosco" in Fiorenzuola d'Arda
1996 - 1999	Scuola Media "G. Gatti" in Fiorenzuola d'Arda
1999 - 2004	Liceo Scientifico "M. Gioia" in Piacenza
2004 - 2008	Studium der Physik an der Università di Pavia, Pavia
2008	Abschluss des Studiums an der Università di Pavia als "Dottore in Fisica" (Bachelor)
2008 - 2011	Studium der Physik an der Università di Milano-Bicocca, Milano
2011	Abschluss des Studiums an der Università di Milano-Bicocca als "Dottore Magistrale in Fisica" (Master)
2011 - 2015	Wissenschaftlicher Mitarbeiter am Institut für Festkörperphysik der Friedrich-Schiller-Universität Jena mit dem Ziel der Promotion

Jena, den 04.11.2015

Davide Cammi

Thesen zur Dissertation

- Der Einfluss der Gas-Umgebung und von Defektzuständen sowie von verschiedenen Behandlungen auf die Photoleitfähigkeit und die sensorischen Eigenschaften von kontaktierten ZnO Nanodrähten wurde in dieser Arbeit untesucht.

- Die Besetzung von Defektzuständen in der Bandlücke vom ZnO kann durch die Gate-Spannung in ZnO Nanodraht-basierten Feldeffekttransistoren kontrolliert werden. Die Photoreaktion mit sichtbarem Licht wurde unter negativer Gate-Spannung beobachtet und der Photoanregung von Elektronen ins Leitungsband zugeschrieben, die von der Gate-Spannung in Grenzflächenzuständen zwischen dem Nanodraht und dem Gate-Dielektrikum gefangen wurden.

- Im Vakuum wurde eine höhere UV-Photoreaktion als in Luft oder inerten Atmosphären gemessen und der Trennung von Elektronen und Löchern zugeschrieben, die von der Bandverbiegung an der Oberfläche induziert wird.

- Nach der Auswertung des Abfalls der Photoleitfähigkeit nach UV-Anregung durch die sogenannte Elovich-Gleichung, rekombinieren circa 90 % der Elektronen durch den Einfang an der Oberfläche, der von adsorbierenden Sauerstoffmolekülen induziert wird. Die übrigen Ladungsträger rekombinieren dagegen im Inneren des Nanodrahts. Diese langsamen Rekombinationsprozesse ergeben eine anhaltende Photoleitfähigkeit.

- Die elektrischen Eigenschaften der kontaktierte Nanodrähte wurden durch Implantation von Aluminium verändert. Nach der Optimierung des Ausheilungverfahrens wurde die Aktivierung von Aluminium als Donator in ZnO Nanodrähten durch eine erhöhte Leitfähigkeit nachgewiesen. Die Implantation führt zu einer erhöhten UV-Photoreaktion und länger anhaltenden Photoleitfähigkeit.

- Die Wasserstoff-Sensitivität von kontaktierten ZnO Nanodrähten wurde unter verschiedenen Wasserstoff Konzentrationen nachgewiesen. Der Funktionsmechanismus zur Sensitivität basiert auf der Interaktion zwischen Wasserstoffmolekülen und adsorbierten Sauerstoffspezies auf der Nanodraht-Oberfläche.

- Plasmabehandlungen in Sauerstoff- und Argon-Atmosphären sind schädlich für den Detektionsprozess, während eine Ausheilung in Sauerstoff hingegen zu einer erhöhten Wasserstoff-Sensitivität führt.

Theses of the Dissertation

- The work presented in this thesis focuses on the influence of the environment and defect levels, as well as of various treatments on the photoconductivity properties of ZnO nanowire devices.
- The occupation of defect levels in the band gap of ZnO can be controlled through the gate voltage in ZnO nanowire field-effect transistors. Photoresponse was observed under visible light at negative gate voltage and attributed to the photoexcitation of electrons from interfacial levels, which are located between the nanowire and the gate oxide.
- The higher UV photoresponse observed in vacuum than in air or inert atmospheres was attributed to the separation of electrons and holes, which is induced by the upward surface band bending of the nanowires.
- The evaluation of the photoconductivity decay after UV excitation with the so-called Elovich equation revealed that around 90 % of the photogenerated electrons recombine through trapping at the surface, which is assisted by the adsorption of oxygen molecules.
- The electrical properties of ZnO nanowire devices were modified by aluminum implantation. The activation of aluminum atoms as shallow donors in ZnO was demostrated by the enhanced electrical conductivity after optimization of the annealing procedure.
- The hydrogen sensitivity of ZnO nanowire devices was investigated under various hydrogen concentration. The sensing mechanism is based on the interaction between hydrogen molecules and adsorbed oxygen species on the nanowire surface.
- Plasma treatments in oxygen and argon atmospheres are deleterious for the detection process, while thermal annealing in oxygen leads instead to enhanced hydrogen sensitivity.

Acknowledgements

I wish to thank all the people who assisted and supported me along this PhD work: I am grateful to Professor Carsten Ronning, for giving me the opportunity to work in his group and for the supervision of my work, as well as for the enjoyable and pleasent atmosphere at the institute. I thank all my colleagues, those from Jena and all others around Europe, with which I had the pleasure to work within the network ”Nanowiring”. Furthermore, this research has been made possible thanks to the fundings from European Union Seventh Framework Program.

Finally, I thank my family and Masha, for their continuous support and affection.